



**Università degli Studi di Roma**

**“Tor Vergata”**

Facoltà di Scienze Matematiche Fisiche e Naturali

Dipartimento di Fisica

**Charmonium production at LHCb:  
measurement of the  $\psi'$  to  $J/\psi$  production  
ratio with the first data**

Dottorato in Fisica, XXII ciclo

**Giovanni Sabatino**

Tutore

*Prof. Giovanni Carboni*

Coordinatore

*Prof. Piergiorgio Picozza*

*Roma, anno accademico 2009/2010*



# Acknowledgments

---

The work described in this thesis was possible thanks to the precious help and useful suggestions that I received from many people. Among them, I have to thank particularly Prof. Giovanni Carboni who had a special role as my tutor and as my teacher, enriching my work with acute observations and criticisms. I would like also to thank all the members of the “Tor Vergata” LHCb group, namely Dr. Emanuele Santovetti, Dr. Alessia Satta and Prof. Roberto Messi for their support and useful suggestions.

The general idea of this work is the result of many stimulating and fruitful discussions I had with Dr. Pierluigi Campana and with Dr. Umberto Marconi, whose support has been fundamental.



# Abstract

---

LHCb is an experiment dedicated to precise measurements of CP violating and rare decays of  $b$ -hadrons. It will exploit the proton-proton collisions at an energy of 14 TeV in the centre-of-mass system, produced by the LHC collider (CERN-Geneva), and will operate at a luminosity of  $2 \times 10^{32} \text{ cm}^{-2}\text{s}^{-1}$ . The expected number of pairs  $b\bar{b}$  produced by the LHC collisions is  $N_{b\bar{b}} \approx 10^{12}/\text{year}$ . LHCb is designed with a robust and efficient trigger whose purpose is to reduce the event rate in input ( $\approx 10$  MHz) to a manageable event rate, enriched in content of heavy flavour quarks, to be written to storage ( $\approx 2$  kHz). The rate reduction is achieved in two trigger levels, L0 (Level 0) and HLT (High Level Trigger), that will be widely discussed in this thesis. A good particle identification as well as efficient tracks and vertexes reconstruction, are fundamental requirements for the reconstruction of the  $b$ -hadron decays and proper time measurement.

LHCb aims to improve the current precision on the CKM parameters and to search for any possible inconsistency with the Standard Model predictions in order to find out eventual “New Physics” effects. The LHCb detector is fully installed, commissioned and ready for data taking: the LHC start-up is expected by the end of 2009.

In the first periods of data taking, the understanding of the apparatus, as well as the preparatory measures, are necessary steps for the future analyses on the  $b$ -hadrons. In particular the charmonium states will be largely produced either as prompt or from  $b \rightarrow c$  transitions. Their well known properties make these resonances ideal for alignment and calibration studies. On the other hand the observation of charmonium states and the measurement, per example, of the prompt cross section ratio between  $\psi(2S)$  and  $J/\psi$  can give some interesting informations about the production mechanisms.

The hadroproduction of  $J/\psi$  and  $\psi(2S)$  is not yet completely understood. Early models could not describe the cross section of directly produced  $J/\psi$  mesons. Such models underestimated the measurements by a factor of approximately 50 and did not adequately describe the cross section shape as a function of  $p_T$ . With the advent of Non-Relativistic QCD (NRQCD) it has been possible to give a better theoretical description of charmonium production through the introduction of the Color Octet model. Nevertheless there are still a lot of issues and open problems: the spin alignment of  $\psi$  mesons predicted by NRQCD theories is totally in

disagreement with the CDF findings (polarization puzzle); moreover recent NLO and NNLO calculations in the Color Singlet model have shown that the amount of the Color Octet needed so far to explain data could be overestimated. Further measurements with  $J/\psi$  and other charmonia states are needed to discriminate between the models and clarify the situation.

In this thesis the measurement of the prompt cross section ratio between  $\psi(2S)$  and  $J/\psi$ , with the first data of LHCb, is described. Simulation studies have been performed to assess the acceptances, the efficiencies and the systematic errors introduced by the apparatus. Particular emphasis is given to the polarization of the  $\psi$ 's and to the systematic induced. This measure is a starting point for the subsequent absolute cross section measurements.

In chapters I-II-III of this thesis essentially we give a detailed description of the LHCb experiment including the trigger and the online monitoring system. In chapter IV we discuss the theory of charmonium production and the expectations at LHCb. In the chapters V-VI, we present a study on Monte Carlo data in which the measurement of the prompt cross section ratio between  $\psi(2S)$  and  $J/\psi$ , in the dimuon channel, is described. Finally, in the chapter VII we will discuss some further prospects on charmonium measurements.

# Contents

---

<b>1</b>	<b>The LHCb experiment at the LHC</b>	<b>1</b>
1.1	Physics motivations . . . . .	1
1.2	The Large Hadron Collider (LHC) . . . . .	2
1.3	The LHCb detector . . . . .	4
1.3.1	The Vertex Locator (VELO) . . . . .	5
1.3.2	The RICH . . . . .	6
1.3.3	The Magnet . . . . .	7
1.3.4	The Trigger Tracker and the Tracking Stations . . . . .	8
1.3.5	The Calorimeter System . . . . .	10
1.3.6	The Muon System . . . . .	12
<b>2</b>	<b>The Muon System</b>	<b>13</b>
2.1	Introduction . . . . .	13
2.2	Overview . . . . .	14
2.3	Detector technology . . . . .	16
2.3.1	Multiwire Proportional Chambers . . . . .	16
2.3.2	Triple-GEM detectors . . . . .	18
2.4	Readout electronics . . . . .	18
2.5	The muon identification . . . . .	20
<b>3</b>	<b>Trigger, Online System and Computing</b>	<b>25</b>
3.1	Trigger . . . . .	25
3.1.1	The Level-0 (L0) . . . . .	25
3.1.2	High Level Trigger . . . . .	30
3.1.3	HLT1 . . . . .	31
3.1.4	HLT2 . . . . .	32
3.1.5	Trigger performance . . . . .	32
3.2	Online System . . . . .	33
3.3	Computing . . . . .	35
3.3.1	Data flow . . . . .	35
3.3.2	The LHCb software . . . . .	36

<b>4</b>	<b>Charmonium hadroproduction</b>	<b>41</b>
4.1	Theory of prompt charmonium production . . . . .	43
4.1.1	The Non-Relativistic QCD approach . . . . .	46
4.2	Monte Carlo generation of $J/\psi$ in LHCb . . . . .	48
4.3	Perspectives at LHC . . . . .	52
4.4	The polarization of $J/\psi$ and $\psi(2S)$ . . . . .	56
<b>5</b>	<b>Selection of <math>J/\psi \rightarrow \mu^+\mu^-</math> and <math>\psi(2S) \rightarrow \mu^+\mu^-</math> events in LHCb</b>	<b>61</b>
5.1	Extraction of signal . . . . .	65
5.1.1	Disentangling prompt charmonia . . . . .	67
<b>6</b>	<b>The measurement of the <math>\psi'</math> to <math>J/\psi</math> production ratio</b>	<b>73</b>
6.1	Efficiency study . . . . .	75
6.1.1	Geometrical acceptance . . . . .	76
6.1.2	Reconstruction and selection efficiency . . . . .	78
6.1.3	Trigger efficiency . . . . .	83
6.1.4	Global efficiency ratio . . . . .	85
6.2	Systematic errors . . . . .	86
6.2.1	Systematic error from polarization . . . . .	87
6.3	Correction factor to the $\psi'$ to $J/\psi$ ratio . . . . .	92
<b>7</b>	<b>Future prospects</b>	<b>95</b>
7.1	$\psi' \rightarrow J/\psi(\mu^+\mu^-)\pi^+\pi^-$ selection . . . . .	96
<b>8</b>	<b>Conclusions</b>	<b>103</b>
	<b>Bibliography</b>	<b>107</b>

# Chapter 1

## The LHCb experiment at the LHC

---

### 1.1 Physics motivations

LHCb is an experiment at LHC dedicated to the heavy flavour physics. Its goal is to study the CP violation in the B meson decays and to look for indirect evidence of “New Physics” in CP violating and rare decays of beauty and charm hadrons. Many models of “New Physics” produce contributions that can change some Standard Model expectations like CP phases or rare decay branching fractions, or may generate decay modes which are forbidden in the framework of the Standard Model: LHCb will investigate such phenomena looking for any new and unexpected effect.

One of the most important objective of LHCb, in the CP violation domain, is the measurement of the  $\varphi_s$  mixing phase in the  $B_s$  system.  $\varphi_s$ , that can be extracted from CP time-dependent asymmetry in the decay  $B_s^0 \rightarrow J/\psi\phi$ , is sensitive to “New Physics”:  $\varphi(B_s^0 \rightarrow J/\psi\phi) = \varphi_s + \varphi^{NP}$ .

Another important goal is the measurement of the CKM angle  $\gamma$  through several decays such as  $B_s^0 \rightarrow D_s K$ ,  $B^- \rightarrow D^0 K^-$ ,  $B_{d,s}^0 \rightarrow h^+ h^-$ . Such a variety of decays makes possible to compare  $\gamma$  measured from different channels in order to get hints of “New Physics”.

Thanks to the very high statistics available, LHCb will also be able to measure rare B decays such as  $B_s \rightarrow \mu^+ \mu^-$  or  $B_s \rightarrow K^{0*} \mu^+ \mu^-$ . For the former decay the Standard Model prediction of the branching fraction has been computed to be  $\text{BR}(B_s \rightarrow \mu^+ \mu^-) = (3.35 \pm 0.32) \times 10^{-9}$  [1], whilst MSSM foresees a sizable enhancement of the branching ratio up to  $\text{BR}(B_s \rightarrow \mu^+ \mu^-) \sim 10^{-8}$ . LHCb could measure such a branching fraction with  $5\sigma$  significance over the background with only  $0.1 \text{ fb}^{-1}$  integrated luminosity.

Beside this major physics programme, LHCb will also give a contribution in the measurements of charmed hadron decays, as well as in the understanding of quarkonia production.

## 1.2 The Large Hadron Collider (LHC)

LHCb exploits the 14 TeV centre-of-mass energy proton-proton colliding beams of the LHC, a collider built and located in a circular tunnel, 27 km in circumference, buried around 50 and 175 m underground at the CERN laboratories. The protons are supplied from the injector chain Linac2 - Proton Synchrotron Booster (PSB) - Proton Synchrotron (PS) - Super Proton Synchrotron (SPS), where they reach the energy of 450 GeV, and finally are injected via two tunnels in the LHC where they are accelerated up to 7 TeV per beam. The figure 1.1 shows a schematic overall view of the LHC and its main experiments. The beams move around the LHC

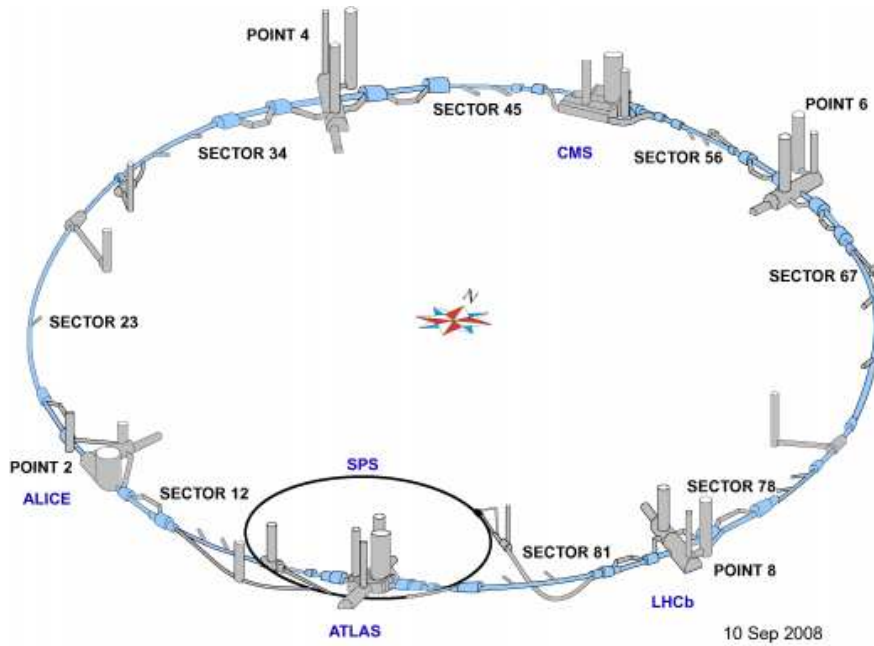


Figure 1.1: An overall view of the LHC machine and its experiments.

ring inside a continuous vacuum chamber (two separate pipes for the two proton beams, that cross at the experiment interaction points) which passes through a large number of magnets: the LHC ring accommodates 1232 main dipoles all having the same basic design, cooled to a temperature below 2 K by superfluid helium and generating magnetic fields above 8 T.

The main experiments at the LHC are located at each of the four interaction points, where the beams cross each other under a small angle. Two consecutive bunch crossings are separated in time by 25 ns, which sets the basic clock frequency for the detector electronics to 40 MHz. The maximum luminosity achievable,  $\mathcal{L} = 10^{34} \text{ cm}^{-2} \text{ s}^{-1}$ , is the luminosity at which the ATLAS [2] and CMS [3] experiments will run. These detectors are located respectively at the interaction points IP1 and IP5. They are general purpose central detectors whose main physics goals are the search of the Higgs boson and the direct detection of possible “New Physics” particles. Besides LHCb, which is dedicated to the study of  $b$ -hadrons, and that will be

widely described in this thesis, there are other three low luminosity experiments: TOTEM [4], located at the same interaction point of CMS, for the detection of protons from elastic scattering at small angles; ALICE [5], located at the interaction point IP2, for the study of lead-lead ion collisions; LHCf [6], an experiment using forward particles created inside the LHC as a source to simulate cosmic rays in laboratory conditions.

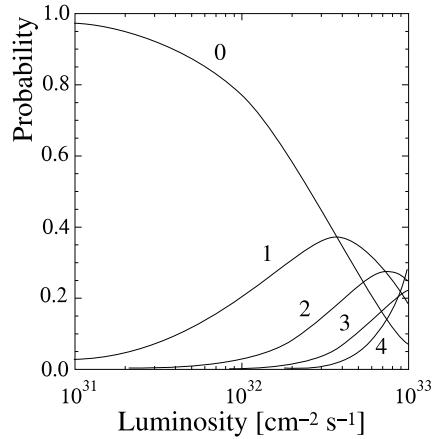


Figure 1.2: Probability of  $n$  inelastic interactions per bunch crossing as a function of the luminosity.

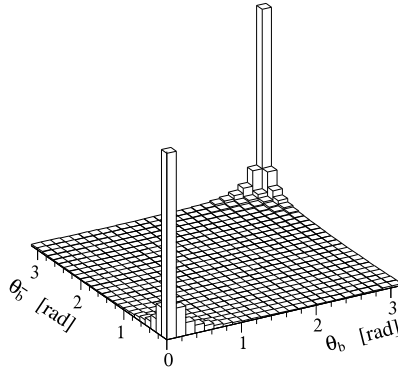


Figure 1.3: Polar angle (with respect to the beam axis) of the two outgoing  $b$  quarks.

The expected total cross section at the LHC is  $\sigma_{tot} \simeq 100$  mb while the expected  $b\bar{b}$  cross section is  $\sigma_{b\bar{b}} \sim 500 \mu\text{b}$  at 14 TeV: LHC will be the most copious source of B mesons in the world able to supply, per example at the LHCb luminosity,  $\mathcal{L} = 2 \times 10^{32} \text{ cm}^{-2} \text{ s}^{-1}$ ,  $10^{12}$   $b\bar{b}$  pairs in one nominal year ( $10^7$  s of data taking). The figure 1.2 shows the probability of  $n$  interactions per bunch crossing as a function of the luminosity. As we can see at  $\mathcal{L} = 2 \times 10^{32} \text{ cm}^{-2} \text{ s}^{-1}$ , the probability

to have multiple interactions is reduced so that the event reconstruction can be facilitated especially in a space region where the background events dominate. In fact at the LHC, since the dominant  $b\bar{b}$  production mechanism is the fusion of two or more gluons, the angular distribution of the two outgoing  $b$  quarks is very peaked at low polar angles (figure 1.3). Hence the two  $b$ -hadrons will be strongly correlated and will be both forward produced or both backward produced. This is essentially the reason for which a  $b$ -physics dedicated experiment at LHC has necessarily to cover low polar angle regions.

### 1.3 The LHCb detector

The LHCb detector [7], [8], [12] is a single arm forward spectrometer housed in the underground pit located at the interaction point IP8. The figure 1.4 shows a

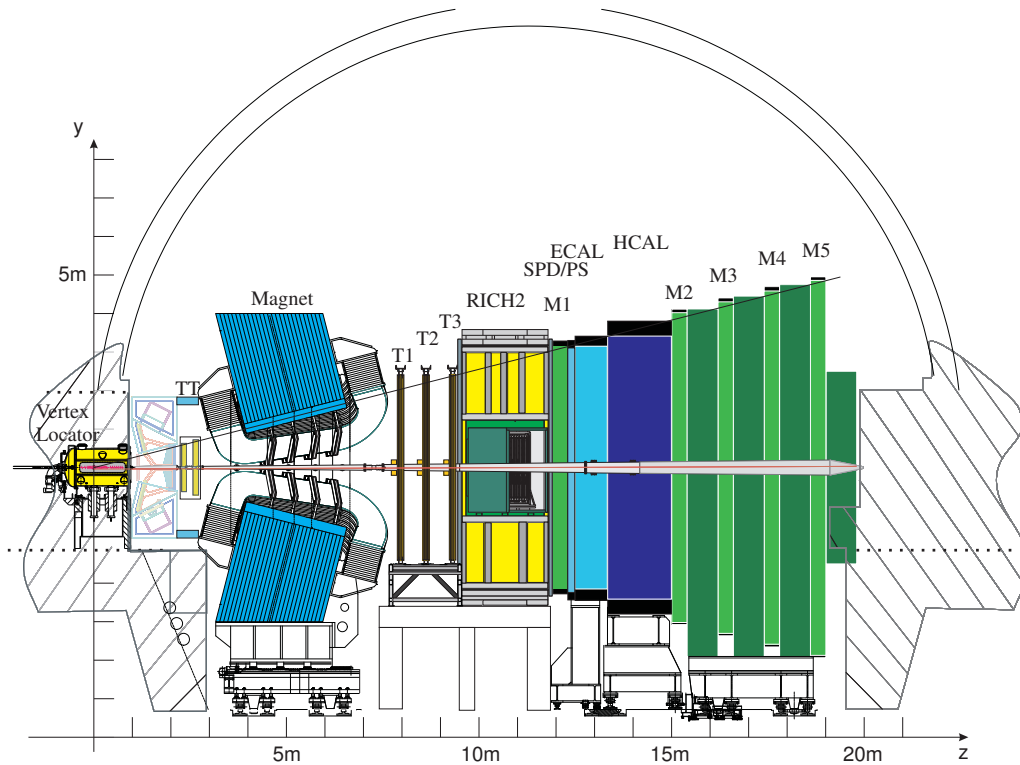


Figure 1.4: The LHCb detector (side view).

side view of the detector. LHCb is composed from the following components (in the figure 1.4 starting from left to right):

- the vertex locator (VELO)
- the upstream ring imaging Cherenkov detector (RICH1)
- the trigger tracker (TT)

- the magnet
- the tracking stations (T1,T2,T3)
- the downstream ring imaging Cherenkov detector (RICH2)
- the preshower detector (SPD/PS)
- the electromagnetic calorimeter (ECAL)
- the hadronic calorimeter (HCAL)
- the muon system.

The beam crossing point has been displaced by  $\approx 11$  m from the centre of the cavern to accommodate the total length of the detector (20 m). The LHCb geometry is imposed by the kinematic of the  $b$ -hadrons produced which, as we have seen in the last section, at the LHC energies, are particularly forward peaked. The detector angular aperture is approximately between 10 and 300 mrad in the horizontal plane (bending plane of the magnet) and between 10 and 250 mrad in the vertical plane (non-bending plane of the magnet) and this corresponds to a pseudo-rapidity range of about  $1.9 < \eta < 5$ .

A right-handed coordinate system is defined with the origin point at the interaction point,  $z$ -axis along the beampipe and the  $y$ -axis oriented upwards.

The beampipe design is particularly delicate since the LHCb experiment is focussed on the large pseudo-rapidity region, where the particle density is high. The mass of the beampipe and the presence of flanges and bellows have a direct influence on the occupancy of the subdetectors, due to secondary interactions. The 19 m long beampipe is divided into four main sections: the first three sections are made of beryllium cones joint by flexible interconnection bellows in order to compensate for thermal expansions and mechanical tolerances. Beryllium was chosen for its high transparency to the particles resulting from collisions. The total length of the first three sections is 12 m, passing through the detector up to the calorimeters. The fourth part of the beampipe, namely the most distant from the interaction point, traversing the muon system, is made of stainless steel.

### 1.3.1 The Vertex Locator (VELO)

The Vertex Locator (VELO) [9] has to provide precise measurements of the track coordinates close to the interaction region. Such informations are used to reconstruct interaction and decay vertices (primary and secondary vertices respectively) and, therefore, the lifetimes of  $b$ -hadrons and  $c$ -hadrons. The informations from the VELO measurements are also used to determine the impact parameter<sup>1</sup> of particles used to tag the hadrons' flavour. Detached vertices play a vital role in the High Level Trigger (HLT) as they are used to enrich the  $b$ -hadron content of the

---

<sup>1</sup>The impact parameter is defined as the distance of closest approach of a reconstructed track to the primary vertex.

data written to storage.

The VELO consists of a series of silicon detector modules, each providing a measurement of the  $r$  and  $\phi$  coordinates (respectively the radial and the azimuthal coordinate), arranged along the beam direction (fig. 1.5). Each silicon module

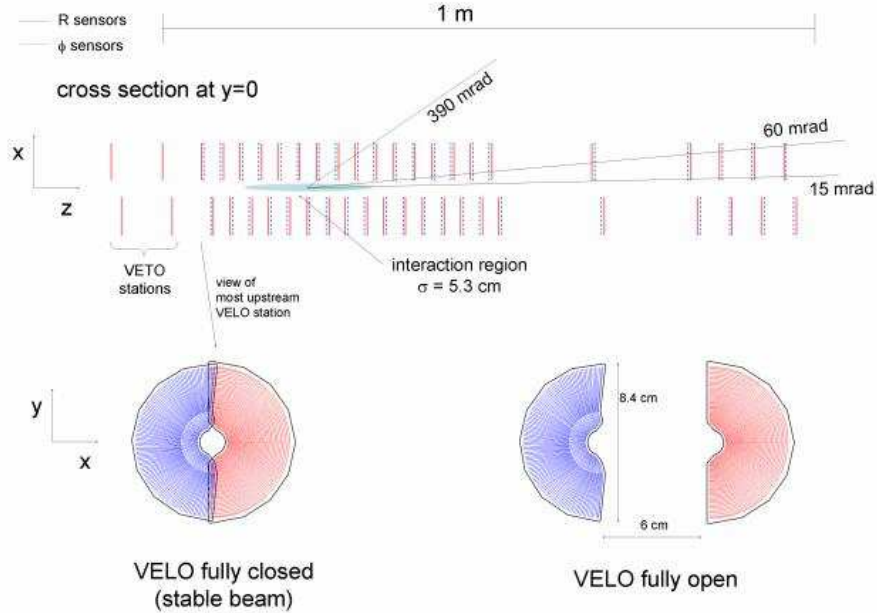


Figure 1.5: Cross section in the  $(x, z)$  plane of the VELO silicon sensors, at  $y = 0$ . Two pile-up veto stations are located upstream of the VELO sensors. The front face of the first modules is also illustrated in both the close and open positions.

has a semicircular shape with a diameter of 90.5 mm. The left and right modules can be moved away from each other to allow, if necessary, safe conditions operation. The  $\phi$ -sensors have radial strips with varying pitch from  $38 \mu\text{m}$  to  $97 \mu\text{m}$ , while  $r$ -sensors have semicircular strips with pitch from  $38 \mu\text{m}$  to  $102 \mu\text{m}$ . The position resolution of the primary vertex is determined by the number of tracks produced in a proton-proton collision. For an average event, the resolution in the  $z$ -direction is  $\simeq 40 \mu\text{m}$  and  $\simeq 10 \mu\text{m}$  in the perpendicular direction. For secondary vertices it varies from 150 to  $300 \mu\text{m}$ . Such challenging spatial resolutions allow to achieve 40 fs proper time resolution, which is a very good result considering that the B meson proper time is of the order of magnitude of few ps.

### 1.3.2 The RICH

Particle identification, and in particular good pion-kaon separation in a wide momentum range, is a fundamental requirement of the LHCb experiment: in the final states of many interesting B hadron decays there are pions and kaons (e.g.  $B_d \rightarrow J/\psi K_s$ ,  $B_s \rightarrow J/\psi \phi(KK)$ ,  $B_{d,s} \rightarrow h^+ h^-$ , etc.).

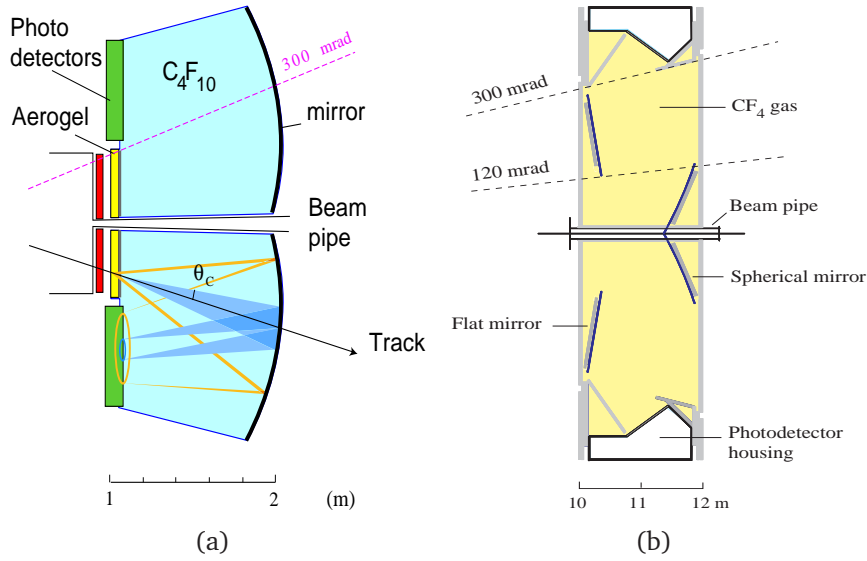


Figure 1.6: Schematic view of the RICH1 (a) and RICH2 (b) detectors.

The two RICH detectors, RICH1 and RICH2 [10], are designed to have high separation performances in the full momentum range. The upstream detector, RICH1, covers the low momentum charged particle range  $\sim 1\text{-}60$  GeV/c using aerogel and  $\text{C}_4\text{F}_{10}$  radiator, while the downstream detector, RICH2, covers the high momentum range from  $\sim 15$  GeV/c up to and beyond 100 GeV/c using a  $\text{CF}_4$  radiator (see figure 1.6). Since there is a strong correlation between the momentum and the polar angle of the track ( $\theta \propto 1/p$ ), the RICH1 has a larger acceptance than the RICH2. In both RICH detectors the focusing of the Cherenkov light is accomplished using a combination of spherical and flat mirrors to reflect the image out of the spectrometer acceptance and Hybrid Photon Detectors (HPD) are used to detect the Cherenkov light in the wavelength range from 200 to 600 nm. The HPD are sensitive to magnetic fields, thus they are surrounded by external iron shields and are placed in MuMetal cylinders to permit operation in magnetic fields up to 50 mT.

The average efficiency for kaon identification for momenta between 2 and 100 GeV/c is  $\epsilon(K \rightarrow K) \sim 95\%$ , with a corresponding average pion misidentification  $\epsilon(\pi \rightarrow K) \sim 5\%$ .

### 1.3.3 The Magnet

A dipole magnet is used in the LHCb experiment to generate the magnetic field needed to measure the charged particle momentum. Saddle-shaped coils with sloping poles are arranged in a frame-window yoke in order to match the required detector acceptance, namely,  $\pm 300$  mrad horizontally and  $\pm 250$  mrad vertically. In figure 1.7 a front view of the magnet is shown. Details on the design of the magnet can be found in [11] and in [12]. The magnetic field is vertically oriented which makes the track to bend in the horizontal  $x\text{-}z$  plane (bending plane). The bending power of the magnet is represented by its total integrated field  $\int Bdl=4$

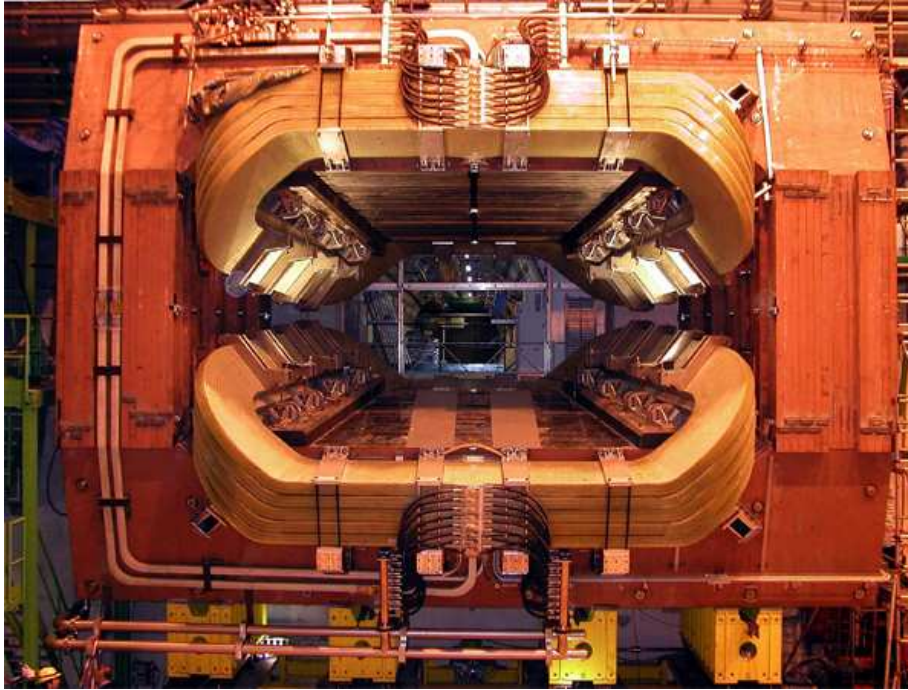


Figure 1.7: In the picture, a front view of the LHCb magnet is shown.

Tm. It dissipates a power of 4.2 MW.

The polarity of the magnetic field can be reversed in order to reduce the systematic errors in CP violation measurements arising from possible left-right asymmetries in the detector.

### 1.3.4 The Trigger Tracker and the Tracking Stations

The Trigger Tracker (TT) [8], [13] is placed just in front of the magnet and downstream of RICH1. It uses silicon microstrip sensors, with a strip pitch of about  $200\ \mu\text{m}$ . The TT is a 150 cm wide and 130 cm high planar detector covering the full detector acceptance. Its total active area is about  $8.4\ \text{m}^2$ . The TT is composed from four detection layers in an  $(x-u-v-x)$  arrangement with vertical strips in the first and the last layer and strips rotated by a stereo angle of  $-5^\circ$  and  $+5^\circ$  in the second and third layer respectively. To aid track reconstruction algorithms and to resolve ambiguities, the four detection layers are arranged in two pairs  $(x-u)$  and  $(v-x)$  separated by 27 cm distance along the LHC beam axis. The TT is used in the trigger, to improve the tracking resolution (hence the momentum resolution) as well as to give an estimation of the momentum of tracks that do not reach the Tracking Stations (T1-T3) [8] (see figure 1.8). These stations are located after the magnet and cover an area of about  $6 \times 5\ \text{m}^2$ . They are made of two different kind of detectors: the innermost part of the detector, the Inner Tracker (IT) [14] uses a silicon strip technology, whereas straw-tubes are employed in the Outer Tracker (OT) [15]. The reason for which silicon technology has been chosen for the IT

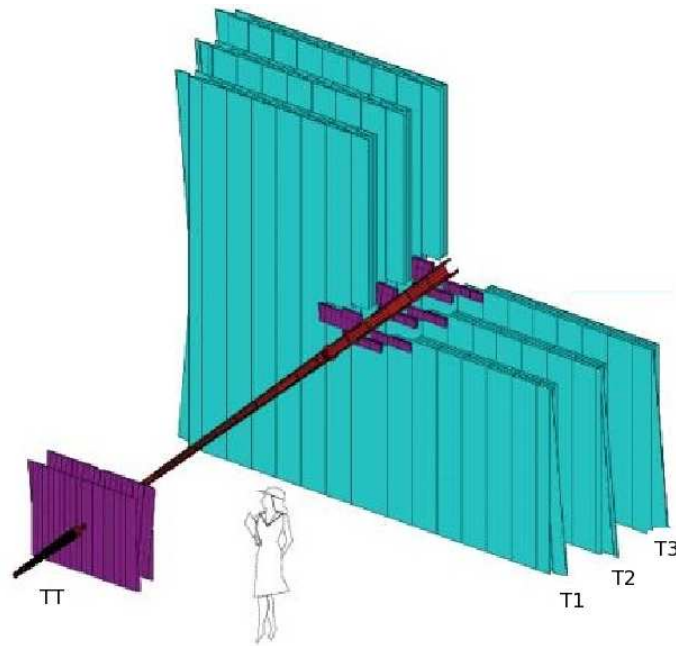


Figure 1.8: Schematic view of the LHCb Tracking System. The TT, T1-T3 and the beampipe are shown.

is the very higher particle flux close to the beampipe with respect to the external regions: the IT covers approximately 2% of the surface but detects about 20% of the tracks passing through the T stations. The straw-tubes of the OT have a 5 mm diameter and 75  $\mu\text{m}$  thick walls. The gas filling the cells is an Ar/CF<sub>4</sub>/CO<sub>2</sub> mixture, which has a drift and collection time of less than 50 ns. The spatial resolution obtained in a test beam experiment with this gas is 200  $\mu\text{m}$ .

In the track reconstruction software, hits in the VELO, TT, IT and OT are combined to form particle trajectories from the VELO to the calorimeters. In the figure 1.9 the possible kinds of tracks that can be reconstructed are represented. The magnetic field is also shown as a function of the  $z$ -coordinate. The long tracks are the tracks traversing the full tracking set-up. They have the most precise momentum determination and therefore are the most important set of tracks for the offline analyses.

The efficiency to find as a long track the trajectory of a particle having momentum larger than 10 GeV/c is about 94%; the corresponding ghost rate<sup>2</sup> is about 9%. The momentum and impact parameter resolutions of the reconstructed long tracks are shown in the figure 1.10. The momentum resolution is plotted as a function of the track momentum and it varies from  $\delta p/p = 0.35\%$  at low momentum up to  $\delta p/p = 0.55\%$  in the high momentum region. The impact parameter resolution is plotted as a function of the  $1/p_t$  of the track: a linear dependence is found. In the low part of the same figure the  $p$  and  $1/p_t$  spectra of B decay particles in the

<sup>2</sup>A ghost track is defined as a reconstructed track that does not match with a Monte Carlo particle.

detector acceptance are also illustrated.

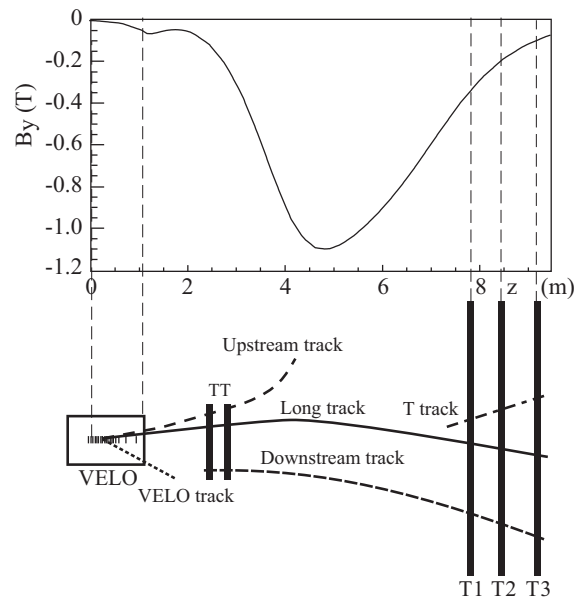


Figure 1.9: A schematic representation of the possible tracks in the tracking stations and in the VELO. The dependence of the magnetic field on the  $z$ -direction is also shown.

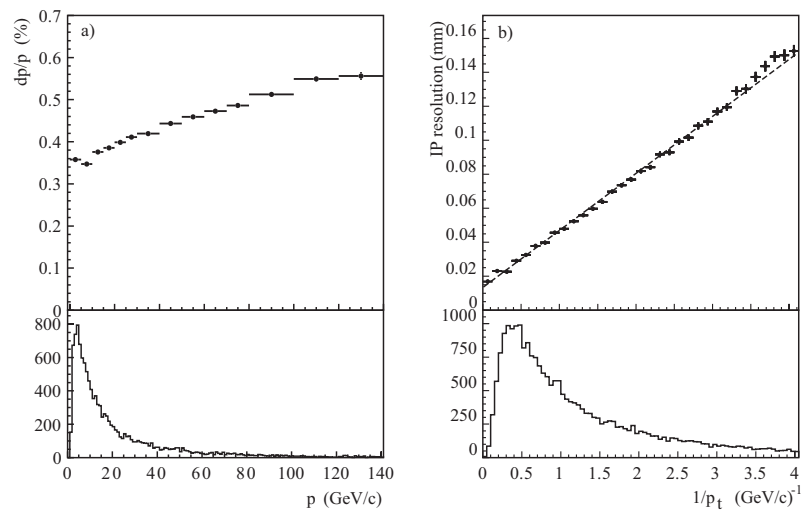


Figure 1.10: Momentum and impact parameter resolution of reconstructed long tracks.

### 1.3.5 The Calorimeter System

For the calorimeter system the classical solution of an electromagnetic calorimeter (ECAL) followed by an hadron calorimeter (HCAL) [12], [16] has been adopted. In addition a preshower SPD/PS detector is placed just upstream the ECAL. The main purpose of the LHCb calorimeter system is to identify electrons, photons and hadrons, and to provide measurements of their energy and positions which are used as input in the first level of trigger.

The SPD/PS detector, consists of a 15 mm lead converter ( $2.5 X_0$  thick), that is sandwiched between two almost identical planes of rectangular scintillator pads. The sensitive area of the detector is 7.6 m wide and 6.2 m high. It is composed by a total of 12032 detection channels designed in accordance with the experiment projectivity. The SPD detector allows to select charged particles and to reject background of  $\pi^0$  with high  $E_T$ . The PS allows longitudinal segmentation of the electromagnetic shower detection.

The ECAL uses shashlik calorimeter technology, namely a sampling scintillator/lead structure read out by plastic WLS fibres. This technology allows fast time response and acceptable radiation resistance of the detector, which were the main requirements for a LHCb calorimeter. The design energy resolution is

$$\frac{\sigma_E}{E} = \frac{10\%}{\sqrt{E}} \oplus 1\% \quad (1.1)$$

where  $E$  is expressed in GeV.

ECAL is placed at 12.5 m from the interaction point and matches projectively the tracking system. The hit density is a steep function of the distance from the beampipe and varies over the active calorimeter surface by two orders of magnitude. The calorimeter is therefore subdivided into inner, middle and outer sections with appropriate cell size, as shown in figure 1.11 (left side). Each module is made from alternating layers of 2 mm thick lead, 120  $\mu\text{m}$  thick, white reflecting TYVEK paper and 4 mm thick scintillator tiles. In depth, the 66 Pb and scintillator layers form a 42 cm stack corresponding to  $25 X_0$ . The Moliere radius of the stack is 3.5 cm.

The HCAL is a sampling device made from iron and scintillating tiles that run parallel to the beam axis. The light in this structure is collected by WLS fibres running along the detector towards the back side where photomultiplier tubes are housed. The lateral segmentation of the HCAL is shown in the figure 1.11 (right side). The length of the tiles and iron spacers in the longitudinal direction corresponds to the hadron interaction length  $\lambda_I$  in steel. The overall HCAL is built as a wall positioned at a distance from the interaction point of  $z = 13.33$  m with dimensions of 8.4 m in height, 6.8 m in width and 1.65 m in depth. The total weight of the HCAL is about 500 tons.

The resolution extracted from a fit to the data at several energies is

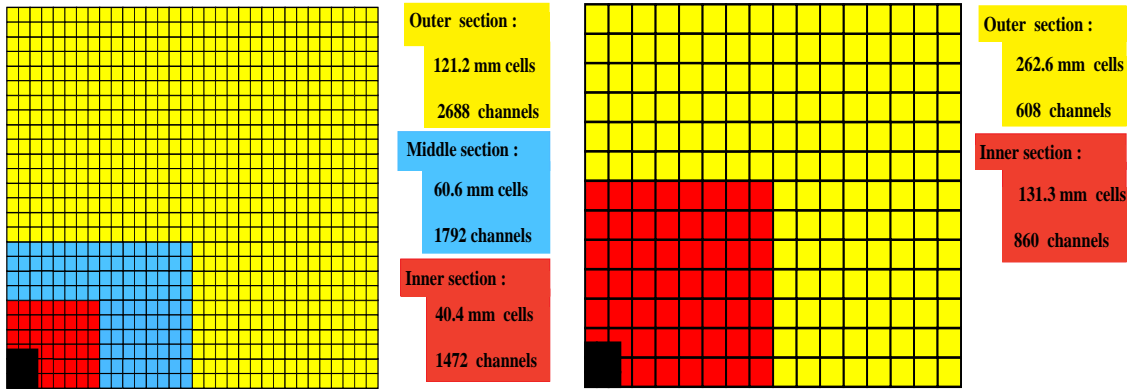


Figure 1.11: The ECAL (left) and HCAL (right) lateral segmentation is shown for one quarter of the front face detector.

$$\frac{\sigma_E}{E} = \frac{(69 \pm 5)\%}{\sqrt{E}} \oplus (9 \pm 2)\% \quad (1.2)$$

where  $E$  is expressed in GeV.

The calorimeter system is fundamental for the identification of electrons, photons and hadrons. The average efficiency to identify electrons from  $J/\psi \rightarrow e^+e^-$  decays from  $B_0 \rightarrow J/\psi K_S^0$  events, in the calorimeter acceptance, is  $\sim 95\%$  while the pion misidentification fraction for the same events is  $\sim 0.7\%$ .

### 1.3.6 The Muon System

The muon detector [12], [17] is composed from five stations, M1-M5, of rectangular shape. The first station, M1, is placed upstream the calorimeter system and the M2-M5 stations are placed downstream the calorimeter. The stations M2-M5 are interleaved by iron wall shields, whilst M1 is separated from the other muon stations by the calorimeter system which acts as a shield. The muon detector is used in the first level of trigger (L0), by detecting the highest  $p_T$  muons in the event, and in the offline muon identification. More details on the muon system are given in the chapter 2.

# Chapter 2

## The Muon System

---

### 2.1 Introduction

LHCb will study many CP-sensitive  $B$  meson decays in which muon pairs are present in the final states. In particular the two *gold-plated* decays

$$B_d^0 \rightarrow J/\psi(\mu^+\mu^-)K_s$$

$$B_s^0 \rightarrow J/\psi(\mu^+\mu^-)\phi$$

will offer the possibility to measure the CP asymmetry in the number of  $B^0$  and  $\bar{B}^0$  decaying in the final state  $f$

$$\mathcal{A}_{CP} = \frac{N_{\bar{B}^0 \rightarrow f}(t) - N_{B^0 \rightarrow f}(t)}{N_{\bar{B}^0 \rightarrow f}(t) + N_{B^0 \rightarrow f}(t)}.$$

The measurement of the CP asymmetry requires the identification of the initial flavour of the  $B$  meson reconstructed (flavour tagging) [18]. The statistical uncertainty on the measured CP asymmetries is directly related to the effective tagging efficiency  $\epsilon_{eff}$ , defined as

$$\epsilon_{eff} = \epsilon_{tag}(1 - 2\omega)^2$$

$\epsilon_{tag}$  being the tagging efficiency (fraction of events in which the tagging procedure gives an answer),  $1 - 2\omega$  being the dilution factor, and  $\omega$  being the wrong tag fraction (probability for the answer to be incorrect when a tag is present). The muon identification plays a vital role in the tagging algorithms. In addition to CP-sensitive decays, LHCb will also study some other interesting  $B$  rare decays with muons in the final state, such as the decay

$$B_s^0 \rightarrow \mu^+\mu^-$$

which, will allow to verify the predictions of Super-Symmetric models. It is clear that, for the purposes of the LHCb experiment, an efficient muon trigger

and a robust and reliable muon identification procedure are necessary requirements.

The LHCb muon system exploits the penetrating power of muons to provide the Level-0 (L0) trigger, selecting muon candidates with the highest  $p_T$  in the event, and to identify muons in the offline reconstruction.

## 2.2 Overview

The muon system is composed from five muon stations, M1-M5, of rectangular shape, placed along the beam axis. The full system comprises 1380 chambers, of which 1368 Multiwire Proportional Chambers (MWPC) and 12 triple-GEM detectors. The total area covered is about 435 m<sup>2</sup>. The inner and outer angular acceptances of the muon system are 20 (16) mrad and 306 (258) mrad in the bending (non-bending) plane respectively. This results in an acceptance of about 20% for muons from inclusive  $b$  semileptonic decays. In the figure 2.1 a side view, in the  $z$ - $y$  plane, of the muon system is shown. The stations M2-M5 are interleaved with 80 cm thick iron walls (muon filters) in order to absorb electrons and hadrons, and to cut off the low energy muons. The calorimeter system is the shielding between M1 and the rest of the muon system. The total weight of the muon shield is about 2100 tons and it has a total absorption-length of 20 nuclear interaction lengths. The minimum momentum of a muon to cross the five stations is approximately 6 GeV/c.

The geometry of the five stations is projective meaning that all their transverse dimensions scale with the distance from the interaction point. The detectors provide space point measurements of the tracks, providing binary information to the trigger processor and to the DAQ. The information is obtained by partitioning the detector into rectangular logical pads whose dimensions define the  $x, y$  resolution. The muon trigger is based on a stand-alone muon track reconstruction and  $p_T$  measurement and requires aligned hits in all the five stations (fivefold coincidence). The stations M1-M3 have an high spatial resolution in the  $x$  direction (bending plane) because they are used to determine the track direction and to measure the  $p_T$  with a resolution of about 20%. The stations M4-M5 have a limited spatial resolution, their main purpose being the identification of penetrating muons.

Each muon station is divided into four regions, R1, R2, R3, R4, with increasing distance from the beampipe. In the figure 2.2 (left side), a quadrant of a muon station is shown: each rectangle represents one chamber; each station contains 276 chambers. The linear dimensions of the regions R1, R2, R3, R4 scale in the ratio 1:2:4:8. The right part of the figure 2.2 shows, as an example, the partitioning of the M1 chambers into logical pads ( $x$ - $y$  granularity). The  $x$ - $y$  resolution worsens far from the beam axis where it is in any case limited by the increase of multiple scattering at large angles. With such a granularity the particle flux and channel occupancy are expected to be roughly the same over the four regions of a given station.

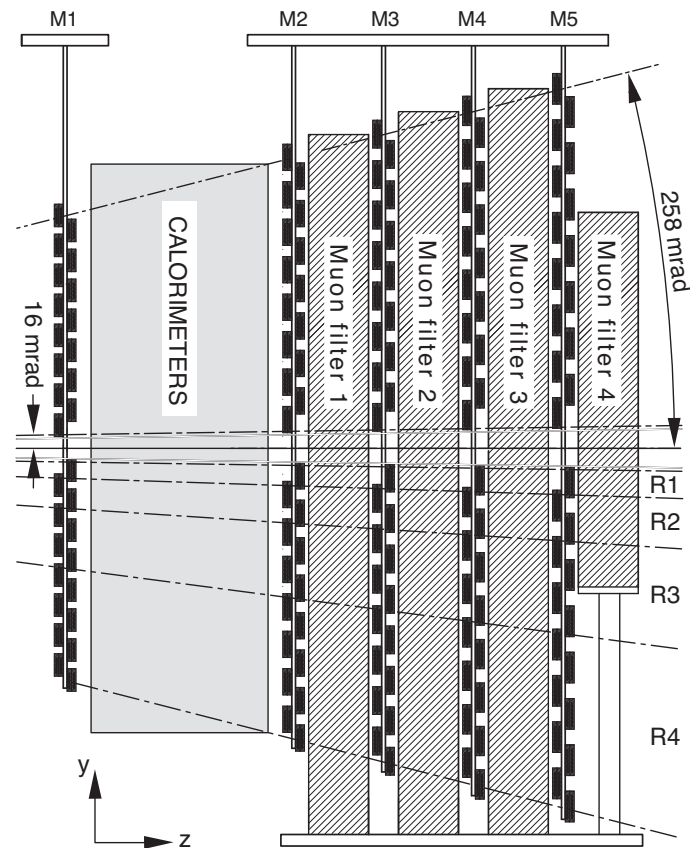


Figure 2.1: Side view of the LHCb muon system.

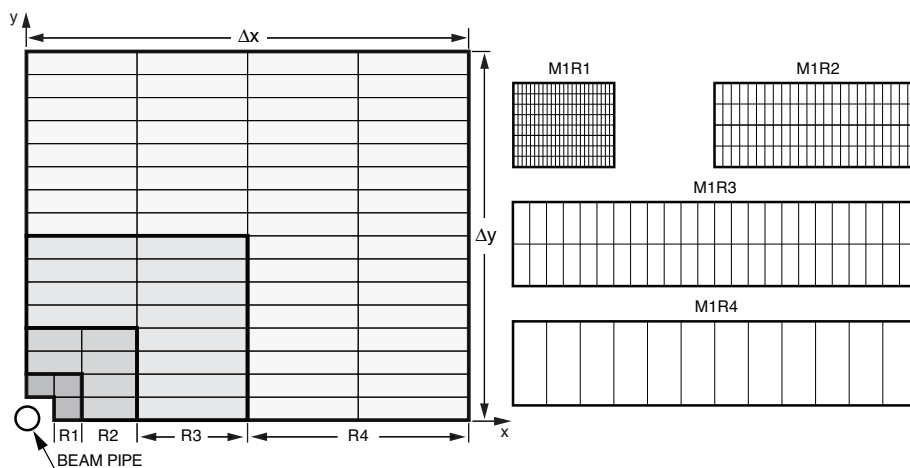


Figure 2.2: A quadrant of the LHCb muon station (left). In the right part, the subdivision into logical pads of the M1 chambers is shown.

A detailed simulation study of the muon system was performed using GEANT4 [19]. In the simulation, starting from the energy deposits of charged particles in the sensitive volumes, the detector signals were created and digitized taking into account detector effects such as efficiency, cross-talk, dead-time, pile-up and spill-over: at the nominal luminosity value,  $\mathcal{L} = 2 \cdot 10^{32} \text{ cm}^{-2} \text{ s}^{-1}$ , the highest rates expected in the inner regions of M1 and M2 are respectively 80 kHz/cm<sup>2</sup> and 13 kHz/cm<sup>2</sup>. In the detector design, appropriate safety factors were applied to the hit multiplicity to account for uncertainties in the simulation.

## 2.3 Detector technology

The intense flux of particles in the muon system and the LHC bunch crossing rate of 40 MHz, imposed stringent requirements on the efficiency, time resolution, rate capability and ageing characteristics of the detectors as well as on the speed and radiation resistance of the electronics.

Multiwire Proportional Chambers (MWPC) are used in the whole muon system except the inner region of the station M1 where the particle rate exceeds the safety limits for ageing. In this region triple-GEM detectors are used.

### 2.3.1 Multiwire Proportional Chambers

The LHCb muon system comprises 1368 MWPC, which are employed in 19 out of 20 regions of the detector. Though the basic detection layout is the same for all chambers (wire spacing, gas gap, gas mixture), the dimensions, granularity and readout system depend on the station and region (19 different chamber types) to account for the different spatial resolutions required. The picture 2.3 shows the MWPC installed on the stations M1 and M2 with the calorimeters in open position. The necessary time resolution is ensured by a fast gas mixture and an optimized charge-collection geometry. The gas used is the non-flammable mixture Ar/CO<sub>2</sub>/CF<sub>4</sub> with the relative concentrations (40:55:5). The gas gap is 5 mm thick and a wire plane of 2 mm wire-spacing, is symmetrically placed in the gap. The wires are laid in the  $y$  direction. In order to increase the efficiency, the time resolution and to provide the necessary redundancy, each M2-M5(M1) chamber is composed of 4(2) OR-ed gas gaps. M1 chambers have 2 gas gaps only to minimize the material amount in front of the calorimeters. The main parameters of the MWPC detectors are reported in table 2.1. Cosmic ray tests [20], [21], [22] have showed a time resolution of about 5 ns and an efficiency of about 99% at the nominal operating voltage (about 2650 V) in 20 ns time window. In the figure 2.4 are shown the efficiency and the cluster size, measured with cosmic rays, for two different chamber types. In both cases the efficiency is close to 99% at the operating voltage; the cluster size is sufficiently low and in agreement with the experiment requirements.

Table 2.1: Main MWPC parameters

Parameter	Design value
No. of gaps	4 (2 in M1)
Gas gap thickness	5 mm
Anode-cathode spacing	2.5 mm
Wire	Gold-plated Tungsten 30 $\mu\text{m}$ diameter
Wire spacing	2.0 mm
Wire length	250 to 310 mm
Wire mechanical tension	0.7 N
Total no. of wires	$\approx 3 \cdot 10^6$
Operating voltage	2.5-2.8 kV
Gas mixture	Ar / CO <sub>2</sub> / CF <sub>4</sub> (40:55:5)
Primary ionisation	$\approx 70 \text{ e}^-/\text{cm}$
Gas Gain	$\approx 10^5$ @ 2.65 kV
Gain uniformity	$\pm 20\%$ typical
Charge/MIP (one gap)	$\approx 0.6 \text{ pC}$ @ 2.65 kV



Figure 2.3: A picture showing the MWPC installed on the muon system. The picture was taken between the stations M1 (left) and M2 (right) with the calorimeters in open position. The beampipe is visible at the centre of the picture.

Each MWPC of the muon system is segmented into *physical pads*: anode wire-pads or cathode pads. Such different technical solutions have been adopted to satisfy the requirements of the spatial resolution and rate capability which vary strongly over the detector regions. The spatial resolution required in the M5R4 chambers, per example, allowed to build physical pads by grouping adjacent wires in order to

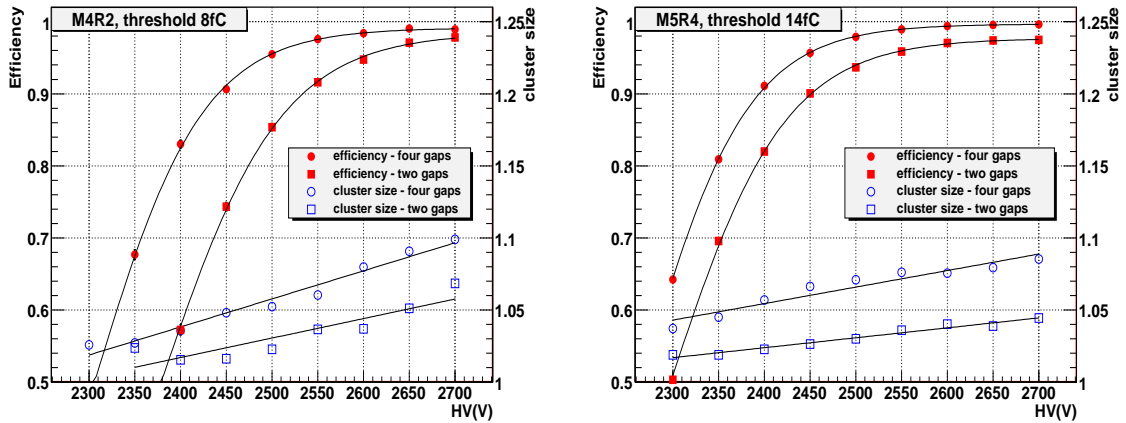


Figure 2.4: The plots show the measured efficiency and cross-talk as a function of the high voltage for two different chamber types of the muon system.

get anode wire-pads. On the other hand, where the spatial resolution would have required smaller pads, a cathode pads readout system (M4R2 per example), or a mixed cathode/anode pads readout system, has been chosen. Each physical pad is read out by one front-end (FE) electronics channel. The FE electronics is based on a custom radiation-hard chip (CARDIAC) [23] specially developed for the muon system. The input stage can be wired to handle either the signal polarity: positive for cathode pads and negative for anode wire-pads.

### 2.3.2 Triple-GEM detectors

In the innermost region R1 of the station M1 the charged particle rate can reach values up to 500 kHz/cm<sup>2</sup>. Such a particle flux requires radiation-hard suitable detectors, able to work for at least 10 years without showing significant ageing effects. This is difficult to achieve in wire chambers unless the gain is decreased, at the price of a worse signal-to-noise ratio.

After an extensive R&D program, triple-GEM chambers with active area 20×24 cm<sup>2</sup> were chosen for M1R1. A total of 12 chambers are needed to cover the entire M1R1 sensitive area. Each chamber consists of two triple-GEM detectors superimposed and forming two sensitive layers which are then logically OR-ed.

The gas mixture used, Ar/CO<sub>2</sub>/CF<sub>4</sub> (45:15:40), allowed to achieve a time resolution better than 3 ns. Measurements on prototype chambers showed an efficiency better than 96% in 20 ns window at a gain of 6 10<sup>3</sup> and a pad cluster size maximum of 1.2.

## 2.4 Readout electronics

The figure 2.5 shows schematically the readout electronics architecture of the muon system. The task of the electronics is twofold: prepare the information

needed by the L0 muon trigger and send the informations to the DAQ. Each phy-

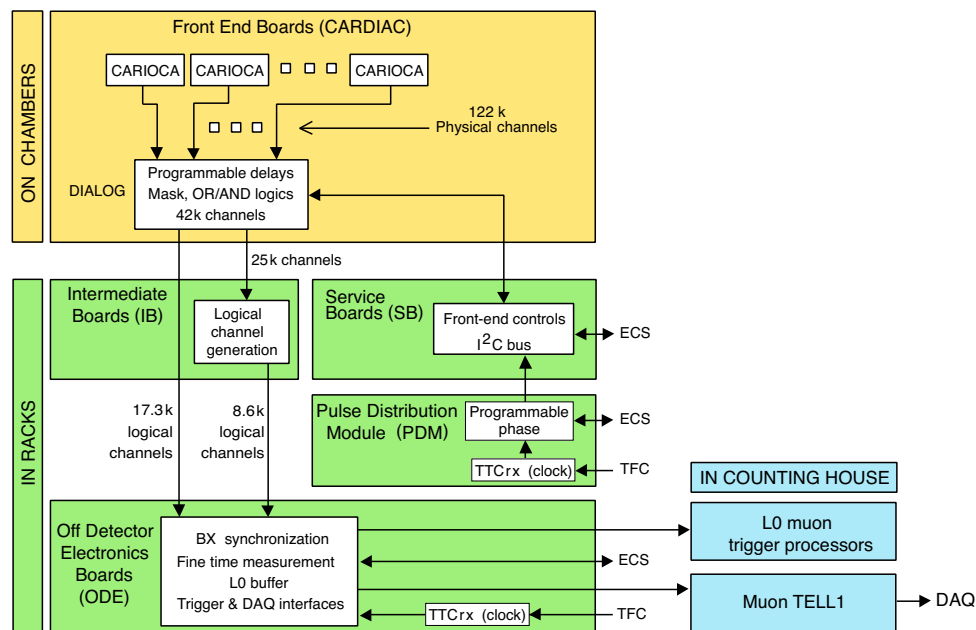


Figure 2.5: Readout electronics architecture of the muon system.

sical pad of the muon system is read out by one front-end (FE) electronics channel. The FE board (CARDIAC) is plugged directly onto the chambers and has 16 inputs and 8 outputs. The CARDIAC is equipped with two CARIOCA and one DIALOG chip. The CARIOCA is a front-end amplifier-shaper-discriminator chip with eight channels whose input polarity is selectable. The peaking time is about 10 ns while the input impedance is 50 Ohm, which is important to reduce internal pad-pad cross-talk. The CARIOCA has separate thresholds for all the channels and an equivalent noise of about 2000 electrons at 0 capacitance which increases as 42-45 e/pF. The DIALOG chip has 16 inputs to receive the outputs from two CARIOCA chips and performs the logical OR of corresponding pads in two layers of a chamber to form logical channels.

The front-end boards are managed by the Service Boards (SB) which are placed in racks beside the muon detector. 156 SBs manage the approximately 8000 CARDIACs of the muon system. The SB handles the setting of the thresholds in the CARIOCA chip, as well as the adjustable delays, the channel masking and the setting of the AND/OR logics in the DIALOG chip.

A Pulse Distribution Module (PDM) resides in every crate containing the SBs. The PDM houses one TTCrx chip which generates low-jitter pulses in a chosen phase relation with the LHC machine clock. The PDM is crucial for the time alignment of the muon system.

Whenever the generation of logical channels is not possible at the DIALOG level, a further level is needed to accomplish the task. This happens in the regions R2, R3 and R4 of the stations M2 to M5. In those regions the logical channels are formed by the Intermediate Boards (IB), which are placed in the electronics racks.

The Off-Detector Electronics board (ODE) contains the L0 pipelines and DAQ interface. It synchronizes the signals and distributes them to the L0 trigger and to the DAQ. 152 ODE boards are employed in the full detector.

To keep the noise and the dead-time of the FE channels to an acceptable level, the rate of a given pad and its electrical capacitance must be limited. This implies that in most chambers the size of the physical pads (either wire or cathode pads) must be smaller than required by spatial resolution. In this cases up to four adjacent physical pads are OR-ed by the electronics to build a logical pad. The  $\sim 122\text{k}$  physical channels of the muon system are logically combined, at the DIALOG level or at the IB level, to form  $\sim 26\text{k}$  logical channels, which identify horizontal and vertical strips on the detector. The logical channels are transmitted to the L0 trigger, where opportune AND combinations of such strips provide the  $\sim 55\text{k}$  logical pads used for the muon tracking.

Upon reception of a trigger, the TELL1 [24] board receives the data from the ODE and sends them to the DAQ. The muon-specific TELL1 board, performs standard control of event synchronization, as well as zero suppression and is also programmed to reconstruct the logical pads as the intersection of two crossing logical channels. In table 2.2 the dimensions and number of logical pads in each region of the muon stations are reported.

## 2.5 The muon identification

The muon identification procedure [25], is an algorithm executed in the offline reconstruction, aiming at identify muons in the event. The muon identification, and the L0 muon trigger which will be discussed in the next chapter, are the main tasks of the muon system.

The muon identification algorithm consists of two main steps:

**IsMuon definition:** given a reconstructed track in the LHCb tracking system, hits in the muon stations are searched around the extrapolation in some Field of Interest (FOI). A boolean decision (IsMuon=0/1) is applied to tracks which satisfy the requirement to have at least one hit in FOI in a number of stations which depends on the momentum of the track. The stations required by the IsMuon decision are shown in table 2.3.

**The Delta Log Likelihood definition:** using the tracks surviving the IsMuon

Table 2.2: Basic information for the five stations M1–M5 and the four regions R1–R4. All dimensions in cm.  $z$ : distance of the stations from the IP;  $\Delta x$  and  $\Delta y$ : dimensions of a quadrant in each station. Rows R1-R4: granularity of the different regions of the muon detector as seen by trigger and DAQ. Number of logical pads per chamber (in brackets) and size of the logical pads, along  $x$  and  $y$ . In parentheses: size of the logical pads projected onto station M1.

	M1	M2	M3	M4	M5
$z$	1210	1527	1647	1767	1887
$\Delta x$	384	480	518	556	594
$\Delta y$	320	400	432	464	495
R1	[24 × 8] 1 × 2.5	[48 × 8] 0.63 × 3.1 (0.5 × 2.5)	[48 × 8] 0.67 × 3.4 (0.5 × 2.5)	[12 × 8] 2.9 × 3.6 (2 × 2.5)	[12 × 8] 3.1 × 3.9 (2 × 2.5)
R2	[24 × 4] 2 × 5	[48 × 4] 1.25 × 6.3 (1 × 5)	[48 × 4] 1.35 × 6.8 (1 × 5)	[12 × 4] 5.8 × 7.3 (4 × 5)	[12 × 4] 6.2 × 7.7 (4 × 5)
R3	[24 × 2] 4 × 10	[48 × 2] 2.5 × 12.5 (2 × 10)	[48 × 2] 2.7 × 13.5 (2 × 10)	[12 × 2] 11.6 × 14.5 (8 × 10)	[12 × 2] 12.4 × 15.5 (8 × 10)
R4	[12 × 1] 8 × 20	[24 × 1] 5 × 25 (4 × 20)	[24 × 1] 5.4 × 27 (4 × 20)	[6 × 1] 23.1 × 29 (16 × 20)	[6 × 1] 24.8 × 30.9 (16 × 20)

requirement, a Delta Log Likelihood (DLL) function, defined as

$$DLL = \log(P_\mu/P_{non-\mu}),$$

is built.  $P_\mu$  and  $P_{non-\mu}$  are observables related to the probability for a given track to be compatible with the muon and non-muon hypothesis. To estimate the probabilities  $P_\mu$  and  $P_{non-\mu}$  the following variable is built

$$D = \sum_{i=0}^N \frac{1}{N} \left\{ \left( \frac{x_i - x_{track}}{pad_x} \right)^2 + \left( \frac{y_i - y_{track}}{pad_y} \right)^2 \right\} \quad (2.1)$$

Table 2.3: Muon stations required by the IsMuon decision as a function of momentum range.

momentum range (GeV/c)	muon stations
$3 < p < 6$	M2+M3
$6 < p < 10$	M2+M3+(M4.or.M5)
$p > 10$	M2+M3+M4+M5

where the sum runs over all the hits in the FOIs,  $x_i$ ,  $x_{track}$ ,  $y_i$ ,  $y_{track}$  are the coordinates of the hits and of the track extrapolations. The distance of the hits to the track extrapolation in a given station and region is normalized to the readout granularity of the muon detector in that station/region (table 2.2).  $D$  represents the average squared distance of hits with respect to the track extrapolation. In the figure 2.6 the average squared distance and the DLL distributions for muons and non-muons, are shown. Once computed the variable  $D$  for a given track, the probability for the muon and non-muon hypothesis, and hence the DLL, are determined.

The muon identification procedure must be robust against possible inefficiencies, dead channels and time misalignments of the muon detector. Different algorithms have been recently developed and optimized to permit the maximum performance of the muon identification even in case of a non-ideal detector [26]. Such algorithms provide alternative definitions of the IsMuon and of the average squared distance, which make the procedure more robust and suitable for the first data taking periods, when the detector behaviour could be not still optimal.

Using a Monte Carlo sample of  $B_0 \rightarrow J/\psi K_S^0$ , the muon identification efficiency was found to be  $\epsilon(\mu \rightarrow \mu) \sim 94\%$  with a corresponding misidentification  $\epsilon(\pi \rightarrow \mu) \sim 3\%$ . The efficiency is a flat function of the momentum above 10 GeV/c (see figure 2.7).

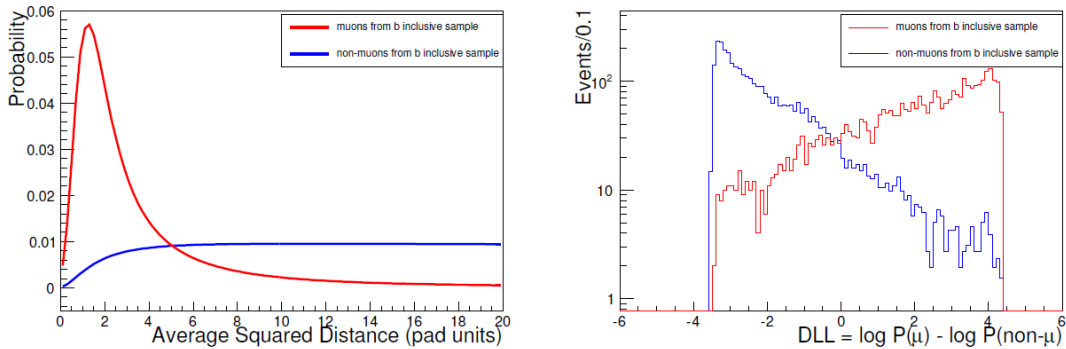


Figure 2.6: The normalized  $D$  distributions for muons and non-muons are shown in the left side plot. By using these distributions it is possible to assign at each track a DLL. The DLL distributions are shown in the right side plot.

On November 23rd 2009, LHCb registered the first proton-proton collisions at 450+450 GeV energy. So far about 300 k minimum-bias events from collisions are being used for the first calibrations and alignments. The figure 2.8 shows a comparison between real data and Monte Carlo average squared distance. A similar comparison is also shown in figure 2.9 for the muon momentum (top) and the muon identification efficiency (bottom). The agreement with Monte Carlo is excellent and the apparatus is working well. These results are very promising.

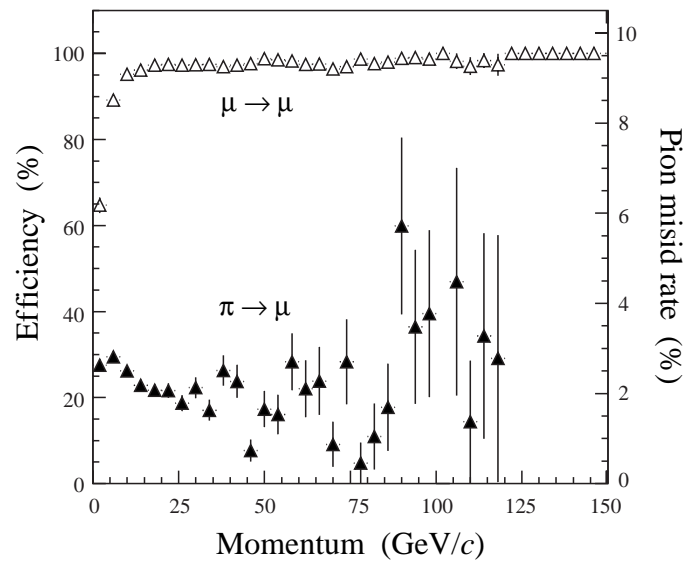


Figure 2.7: Efficiency of the muon ID plotted as a function of the track momentum. The misidentification rate is also shown.

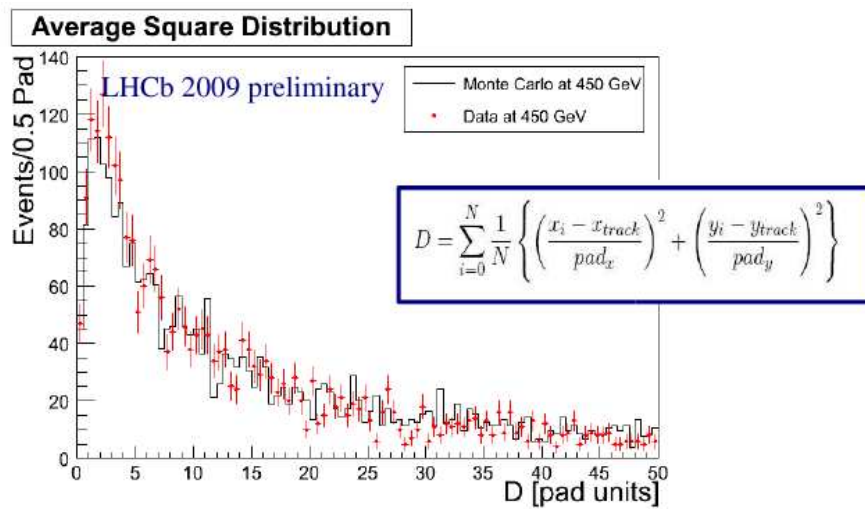


Figure 2.8: Average squared distance: data-MC comparison.

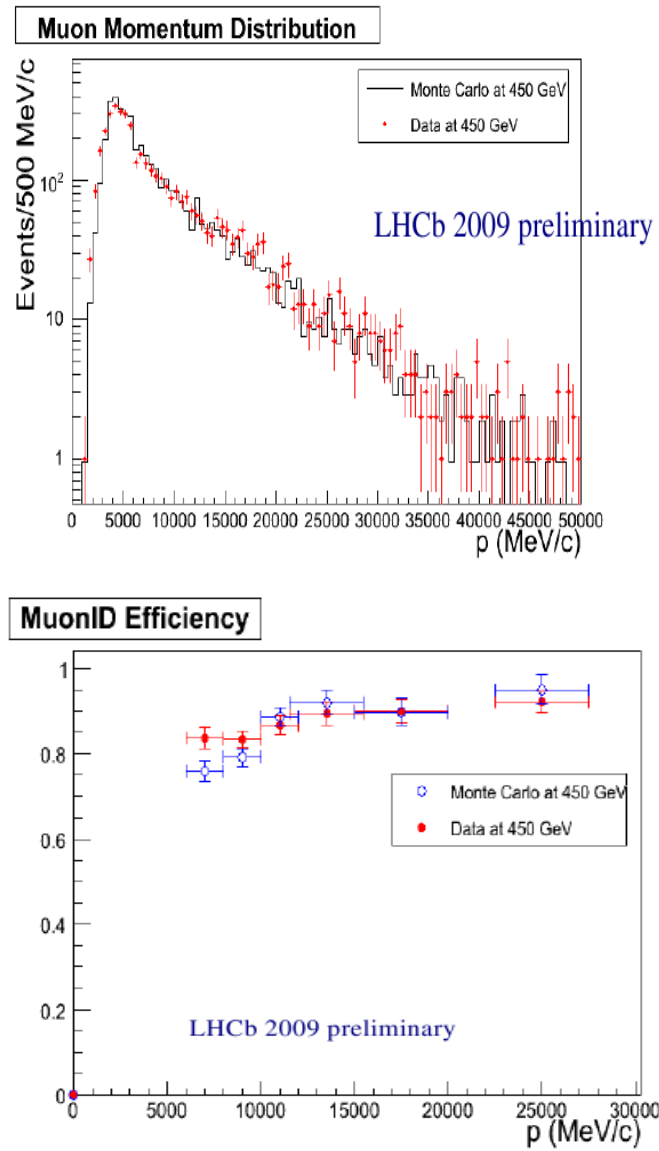


Figure 2.9: Preliminary data-MC comparison: (top) muon momentum distribution, (bottom) muon ID efficiency versus momentum.

# Chapter 3

## Trigger, Online System and Computing

---

### 3.1 Trigger

LHCb plans to operate at a luminosity of  $2 \times 10^{32} \text{ cm}^{-2} \text{ s}^{-1}$ , namely a factor 50 smaller than the maximum design luminosity of the LHC. In this way the number of interactions per bunch crossing is dominated by single interaction: in an experiment dedicated to the  $b$ -physics it is important to reduce possible ambiguities in the vertex reconstruction.

The crossing frequency with visible<sup>1</sup> interactions in the spectrometer, approximately 10 MHz, has to be reduced by the trigger to 2 kHz, at which rate the events are written to storage for further offline analysis. This reduction is achieved in two trigger levels: Level-0 (L0) and High Level Trigger (HLT) [12] (see the figure 3.1). The L0 trigger is implemented using custom made electronics operating synchronously with the 40 MHz bunch crossing frequency, while the HLT is executed asynchronously on a processor farm. The trigger is optimised to achieve the highest efficiency for the events selected in the offline analyses and to reject as strongly as possible uninteresting background events.

#### 3.1.1 The Level-0 (L0)

The purpose of the L0 is to reduce the 40 MHz LHC beam crossing rate, of which 10 MHz with visible events, to 1 MHz, at which rate the full detector can be read out. The L0 trigger reconstructs the highest transverse energy hadron, electron and photon clusters in the calorimeters, or the two highest transverse momentum muons in the muon chambers. Moreover a pile-up system in the VELO (see below) allows to identify events with multiple proton-proton interactions. The informations from the calorimeter trigger, the muon trigger and the pile-up system

---

<sup>1</sup>An interaction is defined to be visible if it produces at least two charged particles with sufficient hits in the VELO and T1-T3 to allow them to be reconstructible.

are collected by the L0 Decision Unit (DU) that derives the final L0 trigger decision for each bunch crossing. The figure 3.2 shows an overview of the L0 trigger components.

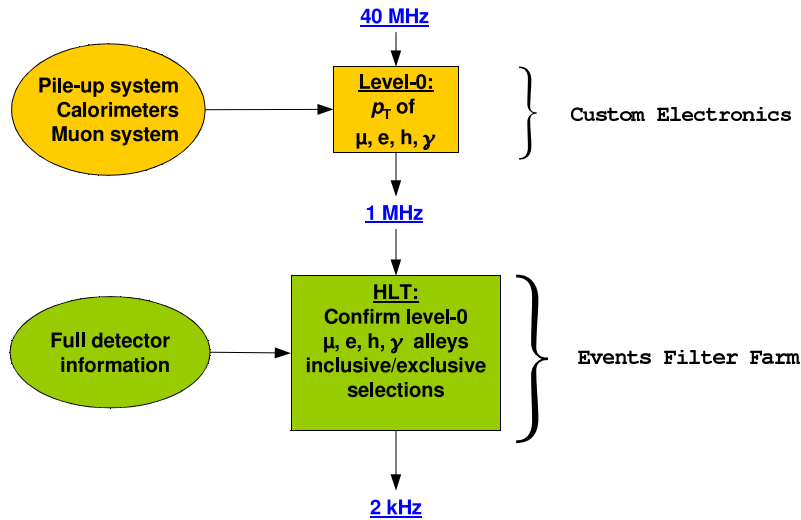


Figure 3.1: In the figure a schematic representation of the LHCb trigger is shown. The 40 MHz bunch crossing frequency, is reduced to 1 MHz event rate by the L0. This is the input rate of the HLT, which further reduces the rate at 2 kHz to be stored for the final offline analyses.

The latency of L0, i.e. the time elapsed between a proton-proton interaction and the arrival of the L0 trigger decision at the front-end electronics, is fixed to  $4 \mu\text{s}$ . This time which includes the time-of-flight of the particles, cable delays and all delays in the front-end electronics, leaves  $2 \mu\text{s}$  for the processing of the data in the L0 trigger to derive a decision.

### Pile-up System

Despite most of the events are characterized by only one proton-proton interaction in the bunch crossing, the probability of multiple interactions is not zero. The pile-up system aims at distinguishing between the crossings with single and multiple interactions. It consists of four silicon sensors placed just upstream the VELO and of the same type of those used in the VELO. The hits released in the pile-up sensors are used to reconstruct tracks from primary vertices in order to provide measurements of candidate primary vertices along the beam line. If multiple interactions are found, the crossing is vetoed.

### Calorimeter Trigger

The calorimeter trigger looks for high  $E_T$  electrons, photons,  $\pi^0$  or hadrons. Clusters of  $2 \times 2$  cells are identified as  $e, \gamma$  or hadrons based on the information

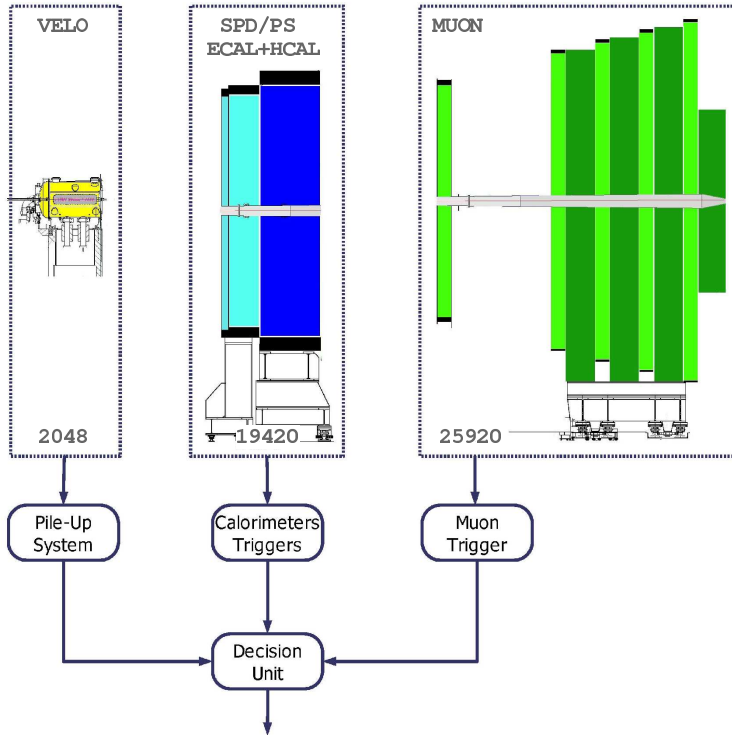


Figure 3.2: A schematic view of the components of the L0 trigger. The pile-up system, the calorimeter trigger and the muon trigger are connected to the respective sub-detectors and to the L0 Decision Unit which provides the final L0 decision.

from SPD/PS detector, ECAL and HCAL. The size of the clusters,  $2 \times 2$  cells, is large enough to contain most of the energy and small enough to avoid overlap of adjacent particles.

A first selection of high  $E_T$  candidates is performed on the front-end card which is the same for ECAL and HCAL. Each front-end card handles and sums the energies of 32 cells. Subsequently the Validation Card, placed on the platform on top of the calorimeters, merges the ECAL with the PS and SPD information prepared by the preshower front-end card. The Validation Card allows to identify the type of electromagnetic candidate: only the highest  $E_T$  candidate per type of particle is selected and sent to the next stage.

The information is then transferred, through 120 m long optical links, to the Selection Crate which is placed in the barrack next to the experimental area in a radiation free environment. Here the candidate with the highest  $E_T$  for each type is selected and the total SPD multiplicity is counted in order to provide a measure of the charged track multiplicity in the crossing.

The selected candidates are sent to the L0 DU via high speed optical links. Inputs and outputs of the Selection Crate are also sent to the data acquisition system via two high speed optical links connected to the TELL1 board.

### Muon Trigger

The figure 3.3 shows an overview of the L0 muon trigger architecture. Each quadrant of the muon detector is connected to a L0 Muon Processor via 456 optical links. Each optical link transmits serialized data at 1.6 Gbps over a distance of 100 m. The four L0 Muon Processor units needed for the whole muon system are located in the counting room (barrack) in a radiation free environment.

The track finding is based on a stand-alone procedure and is performed on the logical pads (see section 2.4). The L0 muon trigger provides a measurement of the track transverse momentum with a resolution of  $\sim 20\%$ .

The L0 Muon Processor looks for the two tracks with the largest  $p_T$ . Seeds of the track finding algorithm are hits in M3 station. For each logical pad hit in M3, an extrapolated position is set in M2, M4 and M5 along a straight line. In order to find hits, windows called Field Of Interest are opened around the extrapolated points. The size of the Field Of Interest depends on the station and region considered, the level of background and the minimum-bias retention allowed. When at least

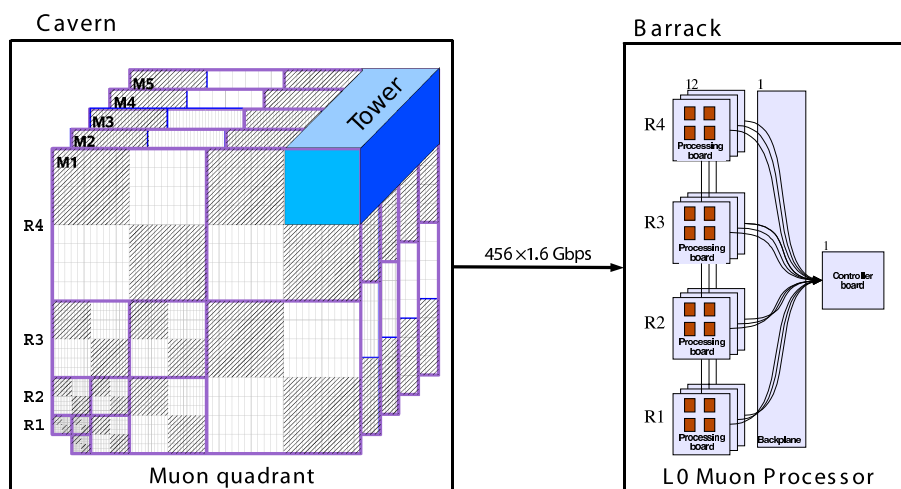


Figure 3.3: Overview of the L0 Muon Trigger architecture.

one hit is found inside the Field Of Interest for each station M2, M4 and M5, a muon track is flagged and the pad hit in M2 closest to the extrapolation from M3 is selected for a subsequent use. The track position in station M1 is determined by making a straight-line extrapolation from M3 and M2, and identifying, in the M1 Field Of Interest, the pad hit closest to the extrapolation point. Finally the hypothesis that the track comes from the interaction point, allows to measure the deviation angle in the magnet and, hence, the momentum of the track.

The geometry of the muon system is totally projective meaning that the dimensions of the logical pads scale with the distance from the interaction point.

Since the muon trigger requires a fivefold coincidence, the requirements on the efficiency of the single stations are very stringent: if the efficiency of each station decreased from 99% to 97%, the trigger efficiency would reduce from 95% to 86% and many interesting events would not be triggered. High single station efficiency is guaranteed by the 4-gaps geometry of the chambers (see section 2.3).

In order to simplify the procedure and to hide the complex layout of the muon system, the muon detector is subdivided into 192 towers (48 per quadrant) pointing towards the interaction point. All towers have the same layout and therefore the same algorithm can be executed in each tower. Each tower is connected to a processing element which is the basic component of the L0 Muon Processor. The processing element is implemented in a FPGA named Processing Unit (PU). A L0 Muon Processor consists of a crate housing 12 Processing Boards, a custom backplane to exchange logical channels between PUs and a controller board which collects muon candidates and selects the two with the highest  $p_T$ .

### Decision Unit

The L0 Decision Unit (figure 3.4) receives informations from the calorimeter, muon and pile-up sub-triggers at 40 MHz, which arrive at different fixed times. The computation of the decision starts with a sub-set of informations coming from a L0 sub-trigger (Partial Data Processing system), after which the sub-trigger informations are time-aligned. An algorithm is executed to derive the decision. The decision is sent to the Readout Supervisor which makes the ultimate decision about whether to accept an event or not. In the L0 DU, the trigger conditions are logically OR-ed to obtain the L0 decision. Electron,  $\gamma$ ,  $\pi^0$ , hadron and muon candidates as

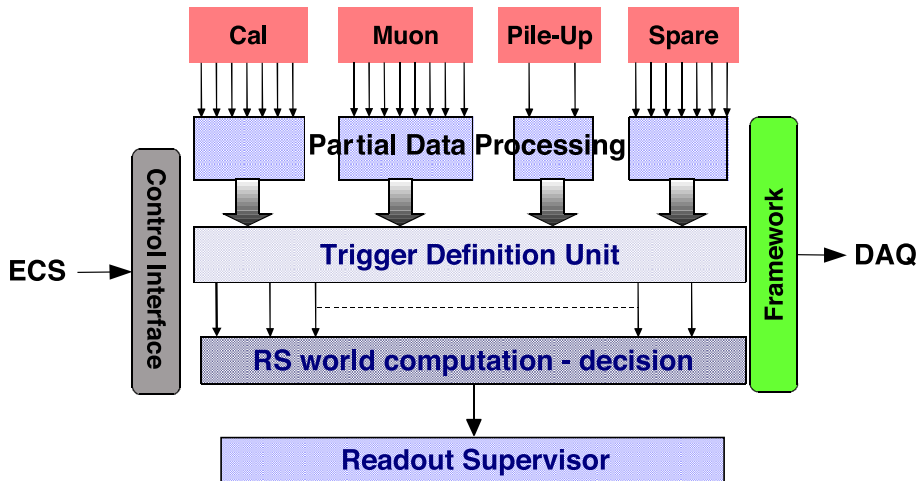


Figure 3.4: Overview of the L0 Decision Unit architecture.

well as intermediate and final decisions are sent to the DAQ via the TELL1 mother

boards. These informations can be used later by the HLT to confirm the L0 candidates using more refined algorithms. The L0 output event rate is 1 MHz.

The L0 is triggered by at least one of the following conditions:

- $E_T^{hadron} > 3.5 \text{ GeV}$
- $E_T^{e,\gamma,\pi^0} > 2.5 \text{ GeV}$
- $p_T^\mu > 1.2 \text{ GeV}$
- $p_T^{\mu 1} + p_T^{\mu 2} > 1 \text{ GeV}$ .

These are the thresholds at nominal running conditions, energy in the centre-of-mass system of 14 TeV and luminosity  $\mathcal{L} = 2 \times 10^{32}/(\text{cm}^2\text{s})$ , but they depend on the running conditions and on the relative bandwidth division between the different L0 triggers. In the very first periods of data taking, when the machine running conditions will be not the nominal ones, the output of the L0 could be so low to allow to store directly the output of the L0 without passing through the HLT or passing through a very loose HLT. Anyway, in this section we will describe the trigger as it will work at nominal conditions and will assume 1 MHz L0 output event rate, which is the maximum L0 output rate being limited by hardware.

## Technology

The transport of information from the front-end electronics to the L0 trigger boards, located in the barrack, at a distance of about 100 m, has to be fast and reliable. Optical links are used as transport media in which serialized data travel from the detector towards the L0 trigger boards. High speed serial transmission reduces the number of signal lines required and offers high level of integration, increasing data rate while keeping a manageable component count and a reasonable cost.

In the emitter side of the optical link, a serializer radiation-hard chip, called GOL, designed by the CERN microelectronics group, transforms every 25 ns a 32-bit word into a serial signal with a frequency of 1.6 GHz using 8B/10B encoding. The receiving side, located in the counting room, is the mirror of the emitting side. The high frequency signals are deserialized into 16-bit words.

The bit error ratio of the optical link, measured with Lecroy SDA11000 Serial Data Analyser, is below  $10^{-16}$  for a single fibre of 100 m long.

FPGA technologies are largely used in the L0 trigger both in the electronics boards close to the detector and in the counting room. They provide good visibility of internal node behavior during the debug phase.

### 3.1.2 High Level Trigger

The High Level Trigger consists of a C++ application which runs on every CPU of the Event Filter Farm (EFF). The EFF contains up to 2000 computing nodes. The

HLT has access to the full detector informations in one event, thus in principle the HLT could perform the offline selections. Nevertheless, given the 1 MHz output rate of the Level-0 and the computing power limitations, the HLT aims to reject most of uninteresting events using only part of the full detector data.

The HLT has been thought to be as much as possible flexible. Its purely software character makes it dynamic and adjustable according to the real needs of the experiment. For that reason the HLT will evolve in time with the knowledge of the experiment and the physics priorities. The figure 3.5 shows a typical trigger flow diagram from the L0 up to the output of the HLT.

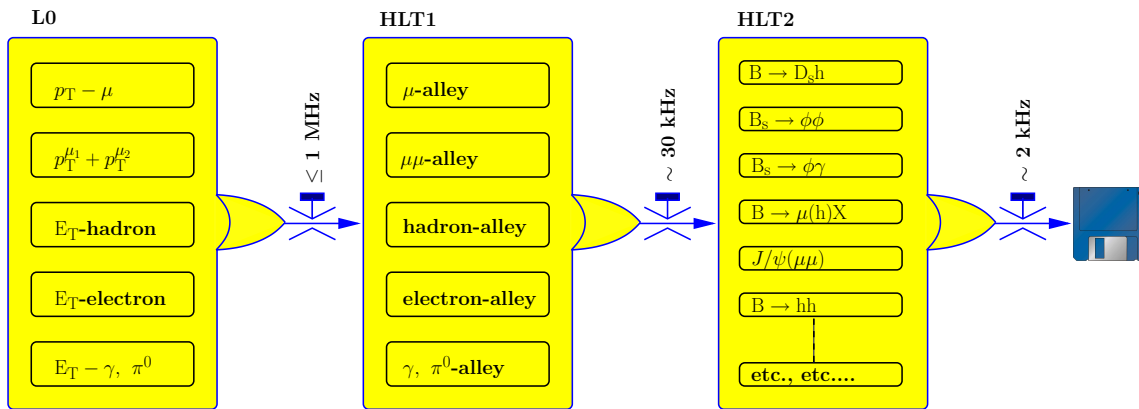


Figure 3.5: Flow diagram of the different trigger sequences (see text).

All calorimeter L0 clusters and muon tracks above threshold are passed to the HLT and will be referred to as L0 objects henceforward. The HLT is divided in two stages, HLT1 and HLT2. The HLT1 aims to confirm the L0 objects by searching for tracks in the VELO and the T-stations corresponding to the L0 electrons, hadrons or muons. In the case of L0  $\gamma$  and  $\pi^0$ , the HLT1 aims to confirm the absence of charged particle tracks corresponding to these L0 objects. This stage is called L0 confirmation. The HLT1 output, of about 30 kHz, allows full pattern recognition by the HLT2, which aims to execute a series of inclusive and exclusive trigger algorithms in order to reconstruct partially or totally several kinds of interesting decays.

### 3.1.3 HLT1

HLT1 starts with the so-called *alleys*. Each alley addresses a type of the L0 trigger, so there will be hadron-alley, electron-alley, etc. Since  $\sim 15\%$  of the L0 events will be triggered by more than one L0 channel, such events will be addressed simultaneously by more than one alley. The HLT1 has to confirm (or to reject) the L0 objects and to do that each alley makes use of a sequence of the following four algorithms:

- L0→T: the L0 objects are assumed to originate from the interaction region, which defines the whole trajectory of the candidate in the detector. T-seeds in the T-stations are reconstructed and are required to match the L0 objects both in space and momentum.
- L0→VELO: VELO-seeds are reconstructed using radial and azimuthal informations of the tracks. These VELO-seeds are required to match the L0 objects with a sufficiently low  $\chi^2$ . Moreover the tracks in the VELO are used to reconstruct the primary vertexes in the event [27].
- VELO→T: the VELO-seeds define a trajectory in the T-stations around which a T-seed is reconstructed and required to match with.
- T→VELO: this algorithm finds the VELO-seeds which match a T-seed, analogue to the L0→VELO algorithm.

As an example let us describe the performance of the muon-alley running at a luminosity  $\mathcal{L} = 2 \times 10^{32}/(\text{cm}^2\text{s})$ : the input rate of the muon-alley will be  $\sim 230$  kHz and contain 1.2 L0 muon objects per event. The L0→T algorithm reduces the rate to 120 kHz and the T→VELO reduces it to 80 kHz. Requiring the remaining candidates to have an impact parameter to any primary vertex larger than 0.1 mm reduces the rate at 10 kHz. The other HLT1 alleys employ similar strategies.

### 3.1.4 HLT2

The combined output rate of the HLT1, of about 30 kHz, is sufficiently low to allow events reconstruction. The HLT2 stage selects tracks with very loose cuts on their momentum and impact parameter to form composite particles, such as  $K^* \rightarrow K^+ \pi^-$ ,  $\phi \rightarrow K^+ K^-$ ,  $D^0 \rightarrow hh$ ,  $J/\psi \rightarrow \mu^+ \mu^-$ , etc., which are then used for all selections. The inclusive and exclusive HLT2 selections exploit cuts on the invariant mass as well as on the impact parameter and aim to reduce the event rate at 2 kHz, at which rate the events are stored for further offline analyses.

The HLT-tracks differ from the offline tracks in not having been fitted with a Kalman filter to obtain a full covariance matrix, since this would require too CPU resources.

Generally speaking, the exclusive trigger selections are more sensitive to the tracking performance than the inclusive trigger selections. The inclusive selections reconstruct partial  $b$ -hadron decays to  $\phi X$ ,  $J/\psi X$ , etc., and result to be less dependent on the online reconstruction. The final trigger is the logical OR of the inclusive and exclusive selections.

### 3.1.5 Trigger performance

The performances of the LHCb trigger have been studied using several Monte Carlo samples of events reconstructed and offline selected. Later in this chapter, the LHCb simulation software and the offline computing will be discussed in detail.

Table 3.1: Efficiency  $\epsilon_{L0} \times \epsilon_{HLT1}$  for some “MC09” events.

Channel(MC09)	$\epsilon_{L0} \times \epsilon_{HLT1}$
$Z_0 \rightarrow \mu^+ \mu^-$	1.00
$B_s \rightarrow \mu^+ \mu^-$	0.97
$B_s \rightarrow J/\psi(\mu^+ \mu^-) \phi$	0.97
$B_d \rightarrow J/\psi(\mu^+ \mu^-) K_s$	0.92
prompt $J/\psi \rightarrow \mu^+ \mu^-$	0.93
$B_d \rightarrow \mu^+ \mu^- K^*$	0.96
$\Lambda_B \rightarrow J/\psi(\mu^+ \mu^-) \Lambda$	0.95
$B_d \rightarrow K^+ \pi^-$	0.88
$B_s \rightarrow \phi \phi$	0.85
$B_s \rightarrow \phi \gamma$	0.77
$B_s \rightarrow D_s K$	0.91

The studies here presented refer to the last generation of LHCb simulated events, the so-called “MC09” (Monte Carlo 2009) production. In this generation, conditions as much as possible similar to the first data taking scenario have been set: the centre-of-mass energy has been set at 5+5 TeV and the pile-up was fixed at  $\nu = 1$ . In the table 3.1 the efficiencies of the Level-0 and HLT1,  $\epsilon_{L0} \times \epsilon_{HLT1}$ , for some of the most important channels are shown. The efficiencies have been determined by running the trigger on events reconstructed and offline selected.

The efficiencies are increasing functions of the minimum-bias retention, which varies in the range from 0.001 to 0.018 for most of channels, therefore the choice of the optimal efficiency depends on the minimum-bias retention allowed.

The HLT2 inclusive and exclusive selections should provide a high minimum-bias reduction factor keeping the efficiency of the channel at about the same level as  $L0 \times HLT1$ . The inclusive muon selections for HLT2, per example, allow to select at the trigger level events such as,  $Z_0 \rightarrow \mu^+ \mu^-$ ,  $B_s \rightarrow \mu^+ \mu^-$ ,  $J/\psi \rightarrow \mu^+ \mu^-$ ,  $\psi(2S) \rightarrow \mu^+ \mu^-$ , etc. All these channels have shown efficiencies of HLT2 from 92% to 98%, with respect to  $L0 \times HLT1$ , and minimum-bias reduction factor up to 120-140.

## 3.2 Online System

The online system [28] ensures the transfer of data from the front-end electronics to permanent storage under known and controlled conditions. This includes not only the movement of the data but also the control of the detectors and of the environmental parameters such as the temperature and pressure. The online system also must ensure that all detector channels are properly synchronized with the LHC clock.

The whole system comprises three main components: the Data Acquisition (DAQ) system, the Timing and Fast Control (TFC) system and the Experiment Control System (ECS). The figure 3.6 shows an overall view of the LHCb online system.

The Data Acquisition system is the transport of the data belonging to a given bunch crossing, and identified by the trigger, from the detector front-end electronics to permanent storage. The DAQ system is based on simple protocols with a small number of components and simple functionalities. Moreover the components are connected through point-to-point links only to increase reliability and robustness of the system. Data from the detector electronics are collected through the LHCb readout TELL1 boards. The data are sent in the Event Filter Farm where the trigger algorithms select interesting events; upon a positive decision the data are subsequently sent to the permanent storage. The quality of the acquired data is checked in a separate monitoring farm which will receive events accepted by the HLT and will house user-defined algorithms to determine, per example, the efficiencies of detector channels or the mass resolution of the detector.

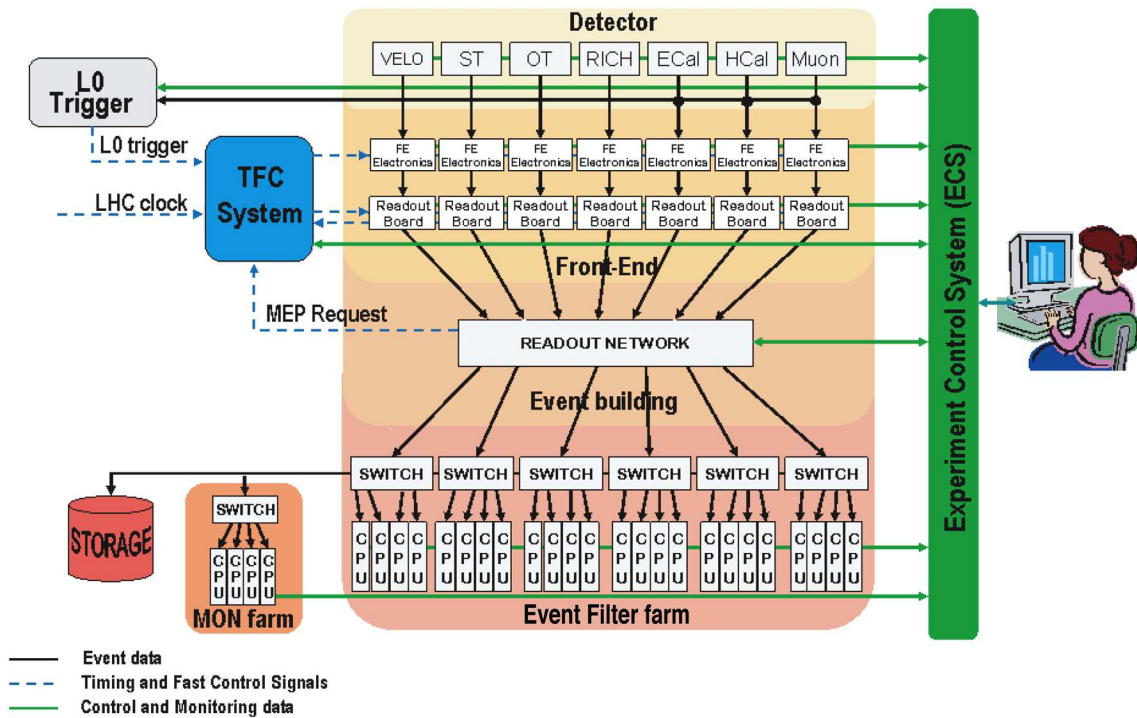


Figure 3.6: General architecture of the LHCb online system with its three major components: Timing and Fast Control, Data Acquisition and Experiment Control System.

The Timing and Fast Control system drives all stages of the data readout of the LHCb detector between the front-end electronics and the online processing farm by distributing the beam-synchronous clock, the L0 trigger, synchronous resets and fast control commands. The system is a combination of electronic components common to all LHC experiments and LHCb custom electronics.

The Experiment Control System ensures the control and monitoring of the en-

the LHCb detector. The ECS controls the high and low voltages of the detectors, the electronics temperatures as well as the gas flows and pressures. It also controls and monitors the Trigger, TFC and DAQ systems.

The ECS software is based on a PVSS II, a commercial SCADA (Supervisory Control And Data Acquisition) system. This toolkit provides the infrastructure needed for building the ECS system, such as a configuration database, graphical libraries to build operation panels and alarm systems.

Based on PVSS, a hierarchical and distributed system was designed to control the LHCb detector. The system is implemented in Device Units and Control Units. A Device Unit denotes a low-level access component which typically communicates directly with the hardware; examples of Device Units are power supplies. A Control Unit implements high-level states and transitions of subordinate Device Units. A typical example of Control Unit is a HV sub-system which controls the ensemble of crates of a sub-detector.

The ECS system has been designed keeping in mind the intuitive and user-friendly use of the final user: the shifter in control room, appropriately trained with a two-days course, will be able to control the status of the LHCb detector and to take the necessary actions to ensure the experiment data taking in safety conditions.

## 3.3 Computing

The events collected by LHCb have to be stored and processed in order to prepare data set files for final analyses. In this section the computing methods and resources used will be discussed, and a description of the LHCb software will be given.

### 3.3.1 Data flow

In the figure 3.7 a schematic view of the LHCb data flow is shown.

The raw data from the detector are produced via the Event Filter Farm of the online system. The raw data are then transferred to the CERN Tier-0 centre for further offline processing and archiving. The raw data, whether real or simulated, must be reconstructed to form physical quantities, such as the calorimeter clusters needed to provide the energy of electromagnetic and hadronic showers, tracker hits to be associated to tracks in order to determine their position and momentum. In this stage the information about particle identification (electron, photon,  $\pi^0$ , charged hadron, muon) is also obtained from the appropriate sub-system. The event reconstruction results in the generation of new data file, the *reduced Data Summary Tape* (rDST). Physics pre-selection algorithms will be run on rDST to determine the four-momentum vectors corresponding to the measured particles, to locate primary and secondary vertices and reconstruct composite particles, such as B candidates. A pre-selection algorithm will be provided for each channel of

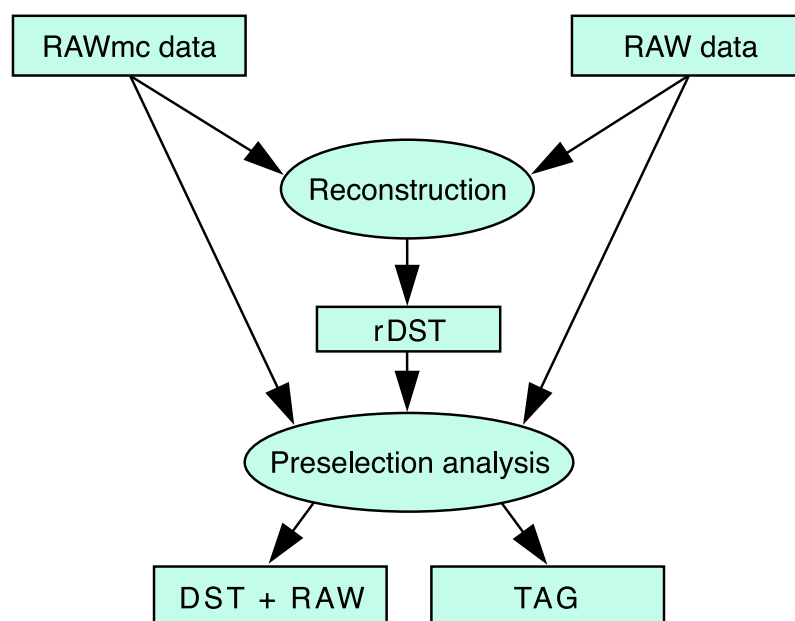


Figure 3.7: LHCb computing logical data flow model.

interest. The events which pass the pre-selection criteria (*stripping*) will be fully re-reconstructed recreating the full information associated with each event. The output of the stripping stage will be referred to as the (full) DST and contains more information than the rDST. The raw data informations for such events will also be saved to permit as much as possible full access to the event. An event tag collection will also be created for faster reference to selected events. The tag file contains a brief summary of the characteristics of each event as well as the result of the pre-selection algorithms and a reference to the actual DST record.

CERN is the central production centre and will be responsible for distributing the raw data in quasi-real time to the Tier-1 centres located in several countries. CERN is the Tier-0 centre and will also take on the role of a Tier-1. Six additional Tier-1 centres have been identified: CNAF (Italy), FZK (Germany), IN2P3 (France), NIKHEF (Netherlands), PIC (Spain) and RAL (United Kingdom). CERN and the Tier-1 centres are responsible for all the production and processing phases associated with the real data. The produced stripped DSTs will be distributed to all production centres ensuring a copy of each file in all Tier-1.

In addition to the Tier-1 centres, a number of Tier-2 is also available for computing: the Tier-2 centres will be primarily Monte Carlo production centres, with both CERN and Tier-1 centres acting as the central repositories for the simulated data.

### 3.3.2 The LHCb software

The reconstruction software can process either real data from the LHCb DAQ system, or simulated events. The simulation chain starts with the GAUSS project [29]

that mimics what will happen in LHCb to allow understanding of its experimental conditions and its performance. It integrates two independent phases:

1. A Generator Phase consisting in the generation of the p-p collisions and the decay of the particles produced.
2. A Simulation Phase consisting in the tracking of the particles in the detector and simulating the physics processes occurring in the experimental setup.

The Generator Phase uses several libraries, in particular uses PYTHIA 6 [30] to generate p-p collisions and EvtGen as decay library specialized for *b*-hadrons. The Geant4 toolkit is used for the Simulation Phase.

The project BOOLE [31] is the final stage of the LHCb detector simulation chain. BOOLE applies the detector response to hits previously generated in sensitive detectors by the GAUSS application. Additional hits are added from Spillover events and LHC background. The digitization step includes simulation of the detector response and of the readout electronics, as well as of the L0 trigger hardware. The output is digitized data that mimics the real data coming from the real detector.

The project aiming to run the HLT is MOORE [32]. MOORE will either run online data from the LHCb DAQ system, or offline starting from real data or from the output of the detector digitization application BOOLE.

The BRUNEL [33] project is the reconstruction software of the LHCb data, either real or simulated data. It reconstructs tracks in the event, it runs the particle ID algorithms and creates as output the so-called “proto-particles”: they are the end of the reconstruction stage and the starting point of the physics analysis. The “proto-particles” have all the links about how they have been reconstructed and a list of particle ID hypothesis with a probability. Moreover they contain the kinematic informations.

DAVINCI [34] is the physics analysis framework for the LHCb experiment. It forms “particles” starting from the “proto-particles” and associating them one choice of particle ID. Once the “particles” are formed (electrons, pions, kaons, muons, etc.), the analyses can be performed combining the “particles” and fitting them in order to form composite particles. DAVINCI allows to apply a series of cuts on many parameters, such as momentum, impact parameter, fitting parameters, in order to select signal events.

Let us conclude this section dedicated to the LHCb software, showing some images of the event display obtained by PANORAMIX [35], the LHCb event display software, for simulated events (figures 3.8, 3.9) and for real events from the 2009 LHC first collisions (3.10).

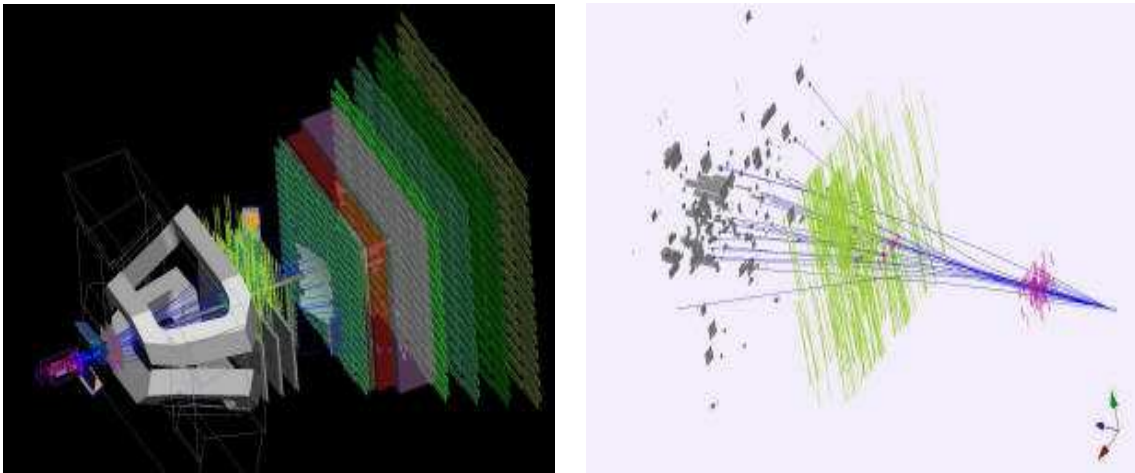


Figure 3.8: (Left) Display of the LHCb detector. (Right) Simulated tracks traversing the tracking system and calorimeter.

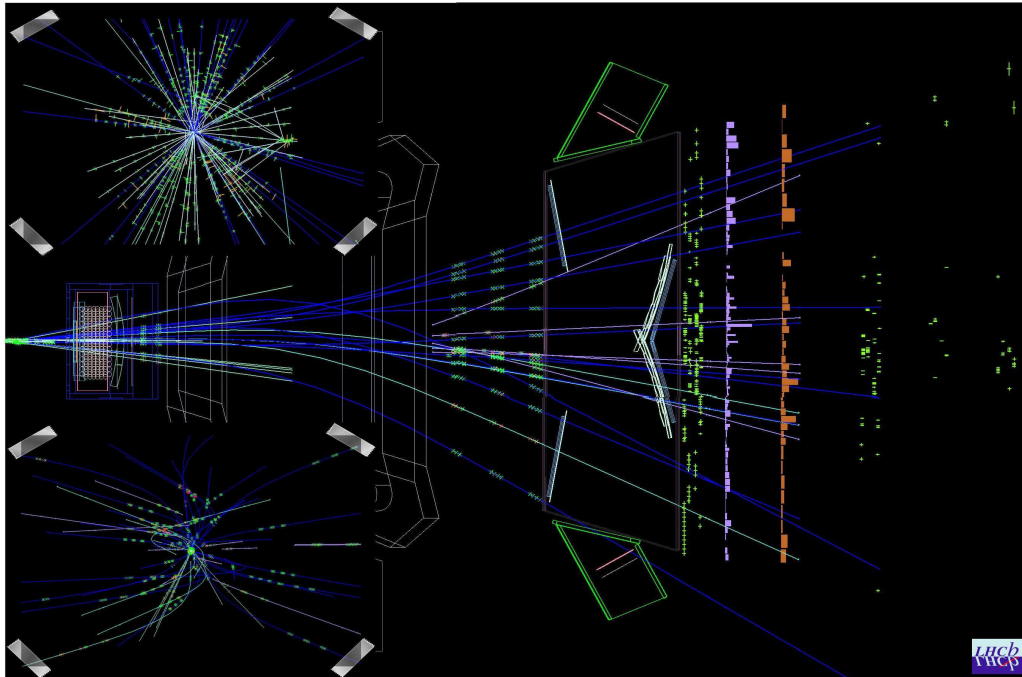


Figure 3.9: Simulated p-p collision at 14 TeV in the LHCb detector producing two  $b$ -hadrons. The two inlets on the left show the event view in the  $xy$ -projection, (top) zoom into the vertex region, (bottom) full size. The big picture is a view from the top, with the two Rich detectors and the magnet displayed. The blue lines are the reconstructed tracks together with their measurements. In the two inlets, all reconstructed tracks with a transverse momentum of more than 300 MeV/c are being displayed, while in the bigger picture only the tracks in the top part of the detector are being displayed.

## LHCb Event Display

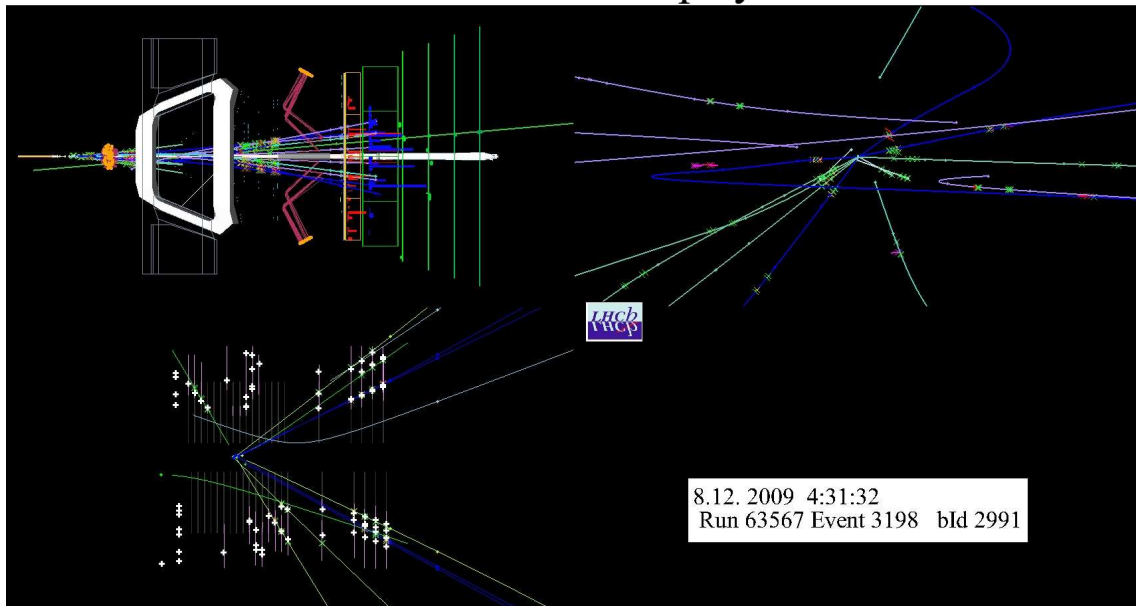


Figure 3.10: Event display of a p-p real collision at 450+450 GeV in the LHCb detector. The reconstructed collision vertex is clearly visible (bottom left). A muon track (green color) is also well visible.



## Chapter 4

# Charmonium hadroproduction

---

The study of the  $^3S_1$  charmonium states,  $J/\psi$  and  $\psi(2S)$ , and the measurement of the cross-sections at LHCb can help the understanding of the charmonium hadroproduction. Despite such particles were discovered about 35 years ago and then subsequently observed in many experiments, there are still unclear mechanisms in the hadroproduction of such mesons.

In high energy hadron collisions, a large fraction ( $\sim 10\%$  at  $p_T=2$  GeV/c and  $\sim 40\%$  at  $p_T=30$  GeV/c) of charmonium comes from  $b$ -hadron decays. This component of charmonium is characterized by having a decay vertex, in general, detached from the production vertex. The study of such decays is fundamental in the analysis of CP violation in the neutral  $B$  meson system and represents one of the main objective of LHCb. Nevertheless, in order to study the hadroproduction of charmonium, the detached component has to be separated from the prompt component, namely the component of charmonium produced in the proton-proton collisions.

The Color Singlet Model (CSM) is the natural application of perturbative QCD to quarkonium production but it has been shown to fail dramatically in describing experimental data: the CSM underestimates the differential cross-sections measured at the Tevatron of two order of magnitude.

Other models, such as the Color Octet Model, have been proposed to describe the hadroproduction of charmonium: although these models can well describe the prompt cross-sections measured at the Tevatron, they still fail in describing the polarization of charmonium. Moreover some recent theoretical calculations at NLO and NNLO in the Color Singlet Model show that the amount of Color Octet Model so far considered to fit data, could be overestimated.

The hadroproduction of charmonium is, finally, still unclear and more measurements are needed to clarify the situation. For a comprehensive theoretical and experimental report of the heavy quarkonium physics see [36].

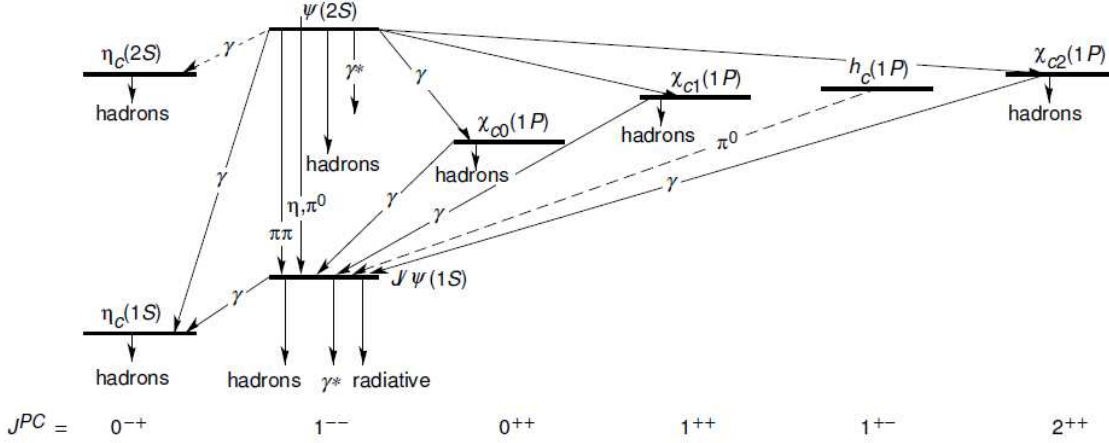


Figure 4.1: Spectrum and transitions of charmonium family.

Table 4.1: Masses, widths and quantum numbers of charmonium family states.

Meson	Mass (MeV)	Width (MeV)	$J^{PC}$
$\eta_c(1S)$	$2980.5 \pm 1.2$	$27.4 \pm 2.9$	$0^{-+}$
$\eta_c(2S)$	$3637 \pm 4$	$14 \pm 7$	$0^{-+}$
$J/\psi(1S)$	$3096.916 \pm 0.011$	$0.0932 \pm 0.0021$	$1^{--}$
$\psi(2S)$	$3686.093 \pm 0.034$	$0.286 \pm 0.016$	$1^{--}$
$\chi_{c0}(1P)$	$3414.75 \pm 0.31$	$10.5 \pm 0.8$	$0^{++}$
$\chi_{c1}(1P)$	$3510.66 \pm 0.07$	$0.88 \pm 0.05$	$1^{++}$
$\chi_{c2}(1P)$	$3556.20 \pm 0.09$	$1.95 \pm 0.13$	$2^{++}$
$h_c(1P)$	$3525.67 \pm 0.32$	$< 1$	$1^{+-}$

The figure 4.1 shows the spectrum and the allowed transitions of the charmonium family. The masses and widths are given in table 4.1.  $J/\psi$  can be produced from the decay of heavier charmonium states, such as  $\chi_{c0}$ ,  $\chi_{c1}$ ,  $\chi_{c2}$  or  $\psi(2S)$ . Some of the main branching ratios for the charmonium states are listed below in table 4.2 [53]. Transitions to  $J/\psi$  from other charmonium states are not allowed or have negligible branching fractions.

Apart from the theoretical interests in the charmonium hadroproduction, there are many other reasons for which to study  $J/\psi$  and  $\psi(2S)$  at LHCb: their well known properties, such as mass, width and branching ratios, as well as their abundance already in the first collisions (we expect about  $18000 J/\psi \rightarrow \mu^+ \mu^-$  per  $\text{nb}^{-1}$ ), make these particles ideal for calibration and understanding of the apparatus in the first periods of data taking. Different selection criteria can be set up in order to exploit the two decay muons to measure, per example, the tracking efficiency or the Muon Identification efficiency.

Table 4.2: Branching ratios for some charmonium states decays.

Decay	Branching ratio
$\psi(2S) \rightarrow J/\psi X$	$(58.7 \pm 0.8)\%$
$\psi(2S) \rightarrow J/\psi \pi^+ \pi^-$	$(33.1 \pm 0.5)\%$
$\psi(2S) \rightarrow \mu^+ \mu^-$	$(0.76 \pm 0.08)\%$
$\chi_{c0} \rightarrow J/\psi \gamma$	$(1.14 \pm 0.08)\%$
$\chi_{c1} \rightarrow J/\psi \gamma$	$(34.1 \pm 1.5)\%$
$\chi_{c2} \rightarrow J/\psi \gamma$	$(19.4 \pm 0.8)\%$
$J/\psi \rightarrow \mu^+ \mu^-$	$(5.93 \pm 0.06)\%$
$J/\psi \rightarrow e^+ e^-$	$(5.94 \pm 0.06)\%$

Finally, since the decay  $J/\psi \rightarrow \mu^+ \mu^-$  is present in the final state of many interesting  $B$  meson decays, the comprehension of the experimental issues related to  $J/\psi \rightarrow \mu^+ \mu^-$  and the evaluation of the efficiencies, is useful also for the future studies on  $b$ -physics.

## 4.1 Theory of prompt charmonium production

The Color Singlet Model (CSM) [37], [38] is the most natural application of QCD to heavy-quarkonium production in the high-energy regime. Its greatest quality resides in its predictive power as the only input, apart from the wave function, can be determined from data on decay processes or by application of potential models. Nothing more is required.

The main assumptions of this model are listed below.

- The charmonium production is divided in two steps, first the creation of two *on-shell* charm quarks ( $c$  and  $\bar{c}$ ) and then their binding to make the meson: these two processes can be factorized.
- The cross-section of the first process is computed with Feynman-diagram methods.
- The velocity of the heavy quarks ( $c$  and  $\bar{c}$ ) in the bound state must be small. One therefore supposes that the meson be created with its two constituent quarks at rest in the meson frame (*static approximation*).
- One finally assumes that the color and the spin of the  $c\bar{c}$  pair do not change during the binding. Since the physical states are colorless, one requires the pair be produced in a *color-singlet state*. This explains the name of the model: Color Singlet Model.

In the CSM the general expression of the cross-section for the production of a charmonium state  $\psi=J/\psi, \psi(2S)$ , can be written as

$$\sigma(pp \rightarrow \psi + X) = \sum_{i,j} \int dx_1 dx_2 f_{i/p} f_{j/p} \hat{\sigma}(ij \rightarrow c\bar{c}[{}^3S_1^{[1]}] + X) |\Psi(0)|^2 \quad (4.1)$$

where  $i, j$  are two partonic species,  $f_{i/p}, f_{j/p}$  are the respective parton density functions and  $|\Psi(0)|^2$  is the squared wave function at the origin. The superscript <sup>[1]</sup> denotes the color singlet state of the  $c\bar{c}$  pair.

In high-energy hadronic collisions, the leading contribution to the production of heavy quarks, comes from the gluon fusion process: as the energy of the collider increases, the initial parton momentum fraction  $x_i$  needed to produce the quarkonium decreases to reach the region in  $x$  where the number of gluons becomes much larger than the number of quarks. The figure 4.2 shows one of the Feynman diagrams for the  ${}^3S_1$  states production associated with a gluon [39]. The

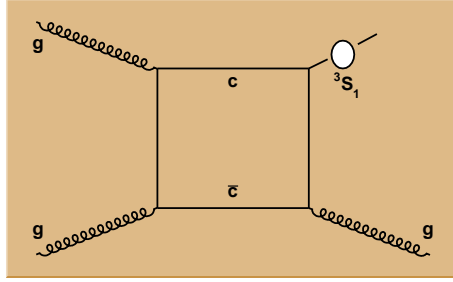


Figure 4.2: One of the Feynman diagrams describing the  ${}^3S_1$  states production by the gluon fusion. This is the basic process at the Leading Order in the Color Singlet Model.

calculation at the LO within the framework of the Color Singlet Model leads to

$$\frac{d\hat{\sigma}}{dp_T^2}(gg \rightarrow c\bar{c}[{}^3S_1^{[1]}] + g) |\Psi(0)|^2 \sim \frac{\alpha_s^3}{p_T^8} \quad (4.2)$$

The gluon-gluon cross-section is proportional to  $\alpha_s^3$ , due to the three gluon vertices in the diagram, and to  $1/p_T^8$ . The wave function at the origin, which enters directly in the expression of the cross-section, introduces a theoretical uncertainty. Its value is extracted from the leptonic decay width  $\Gamma_{\mu\mu} \propto |\Psi(0)|^2$ , thus the error on  $\Gamma_{\mu\mu}$  introduces an error on the cross-section computed.

In 1993, Braaten and Yuan [40], pointed out that gluon fragmentation processes, even though of higher order in  $\alpha_s$ , were to prevail over the LO CSM for  $S$ -wave mesons at large  $p_T$ . The figure 4.3 shows the two Feynman diagrams describing the fragmentation processes.

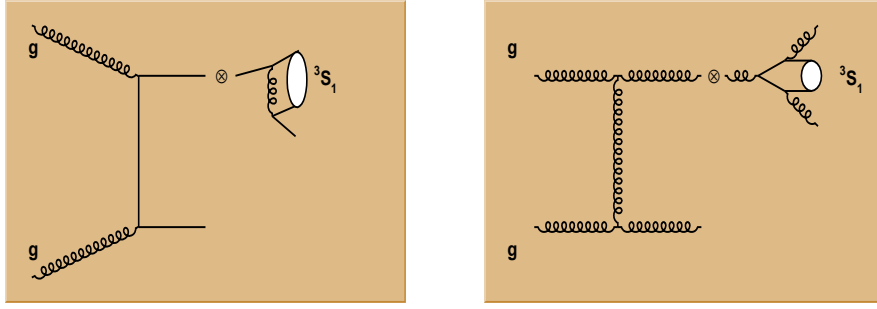


Figure 4.3: Two Feynman diagrams depicting the fragmentation processes, which occur in the Color Singlet Model.

The left side diagram introduces in the cross-section the term

$$\frac{d\hat{\sigma}}{dp_T^2}(gg \rightarrow c\bar{c}) \otimes D(c \rightarrow {}^3S_1^{[1]} + c) + \mathcal{O}\left(\frac{m_c}{p_T}\right) \sim \frac{\alpha_s^4}{p_T^4} \quad (4.3)$$

while the right side diagram introduces the term

$$\frac{d\hat{\sigma}}{dp_T^2}(gg \rightarrow gg) \otimes D(g \rightarrow {}^3S_1^{[1]} + gg) + \mathcal{O}\left(\frac{m_c}{p_T}\right) \sim \frac{\alpha_s^5}{p_T^4}. \quad (4.4)$$

By comparing the equations 4.3 and 4.4 with the equation 4.2 it is clear that the fragmentation processes dominate the Leading Order at large transverse momentum.

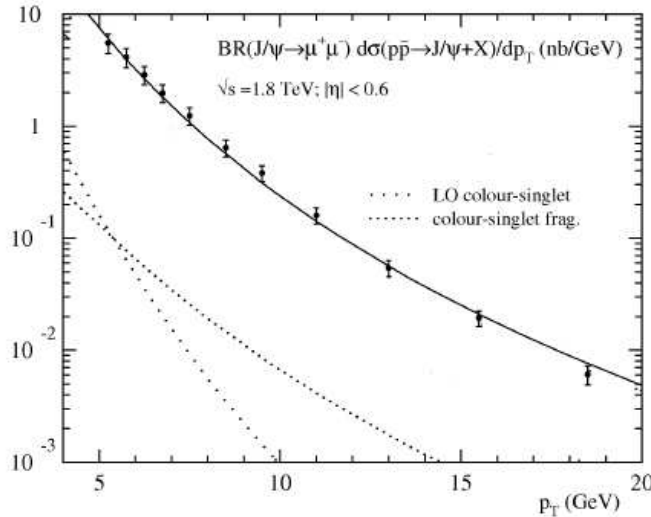


Figure 4.4:  $J/\psi$  production cross-section, times the dimuon branching fraction, as a function of  $p_T$  measured by CDF at the Tevatron. The steepest dotted curve is the prediction of CSM at Leading Order. The other dotted curve is the prediction of CSM including fragmentation processes (see text). The fitted curve suggests the needed of additional models to describe data.

The figure 4.4, [41], shows the  $J/\psi$  differential cross-section as a function of the transverse momentum, measured by CDF experiment at the Tevatron. The dotted curves represent the theoretical predictions of the Color Singlet Model: the steepest curve does not include the fragmentation contributions; the other dotted curve, which includes the fragmentations, well describes the shape but underestimates the cross-section of two orders of magnitude. The Color Singlet Model predictions are in disagreement with data and the same conclusions hold also for  $\psi(2S)$  (see figure 4.5).

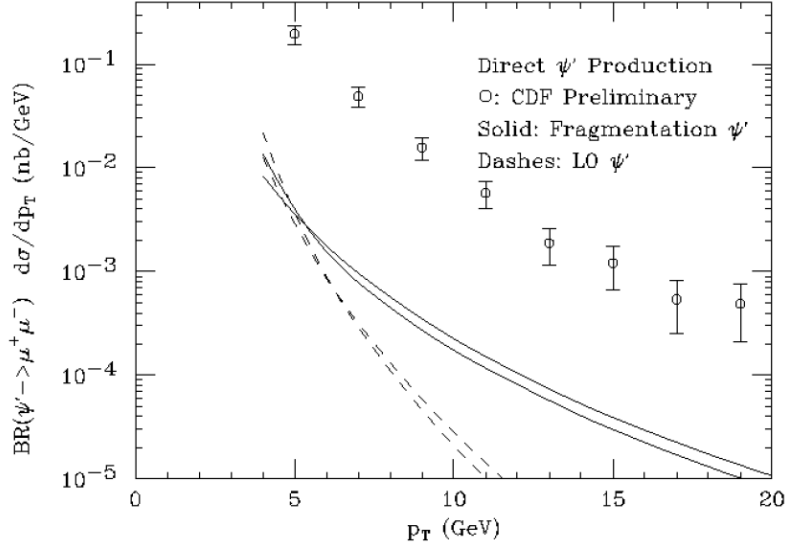


Figure 4.5:  $\psi(2S)$  production cross-section, times the dimuon branching fraction, as a function of  $p_T$  measured by CDF at the Tevatron. The dashed line curve is the prediction of CSM at Leading Order. The solid line curve is the prediction of CSM including fragmentation processes (see text). The data suggest the needed of additional models.

#### 4.1.1 The Non-Relativistic QCD approach

The Color Singlet Model has been superseded by a rigorous framework, based on the use of non-relativistic QCD (NRQCD) [42], an effective field theory that provides a solid ground for accurate theoretical analyses.

In the NRQCD approach the cross-section for the production of a charmonium state  $H$  in a proton-proton interaction is expressed as a sum of terms, each of which factors into a short-distance coefficient and a long-distance matrix element:

$$\sigma(pp \rightarrow H + X) = \sum_{i,j} \int dx_1 dx_2 f_{i/p} f_{j/p} \sum_n \hat{\sigma}(ij \rightarrow c\bar{c}[n] + X) \langle \mathcal{M}^H[n] \rangle \quad (4.5)$$

where the indexes  $i, j$  run over all the partonic species and  $n$  denotes the color, spin and angular momentum state of an intermediate  $c\bar{c}$  pair. The short-distance

cross-section  $\hat{\sigma}$  can be calculated as perturbative expansion in the strong coupling  $\alpha_s$ . The NRQCD long-distance matrix elements  $\langle \mathcal{M}^H[n] \rangle$  are related to the non-perturbative transition probabilities from the  $c\bar{c}$  state  $n$  into the charmonium  $H$ . They scale according to a definite power of the intrinsic heavy-quark velocity  $v$  within the bound state ( $v^2 \sim 0.3$  for charmonium) [43]. The equation 4.5 contains all possible intermediate states  $n$  of the  $c\bar{c}$  pair and hence color octet states are allowed. In the case of S-wave orthoquarkonia ( $^3S_1$ ) the only transitions that occur are the ones due to intermediate  $c\bar{c}$  color singlet and color octet states. So that we can distinguish between two classes of matrix elements: the color singlet ones and the color octet ones. The color octet matrix elements, which give the probability of transition between one of the states  $^1S_0^{[8]}$ ,  $^3P_0^{[8]}$ ,  $^3S_1^{[8]}$  and the physical color singlet  $^3S_1^{[1]}$  state, are not known and have to be extracted from data. In table 4.3 the NRQCD matrix elements are listed for  $J/\psi$  and  $\psi(2S)$  [44]. The amplitudes to produce  $^1S_0^{[8]}$  and  $^3P_0^{[8]}$  have the same  $p_T$  slope and their coefficient cannot be determined separately, thus only the combination  $\mathcal{M}_k^H(^1S_0^{[8]}, ^3P_0^{[8]}) = \langle \mathcal{M}^H[^1S_0^{[8]}] \rangle + k \langle \mathcal{M}^H[^3P_0^{[8]}] \rangle / m_c^2$  ( $k = 3.5$ ) can be determined.

Table 4.3: NRQCD matrix elements for charmonium production. The color singlet matrix elements are taken from potential models. The color octet matrix elements have been extracted from CDF data.

$H$	$\langle \mathcal{M}^H[^3S_1^{[1]}] \rangle$	$\langle \mathcal{M}^H[^3S_1^{[8]}] \rangle$	$\mathcal{M}_k^H(^1S_0^{[8]}, ^3P_0^{[8]})$
$J/\psi$	$1.16 \text{ GeV}^3$	$(1.19 \pm 0.14) \times 10^{-2} \text{ GeV}^3$	$(4.54 \pm 1.11) \times 10^{-2} \text{ GeV}^3$
$\psi(2S)$	$0.76 \text{ GeV}^3$	$(0.50 \pm 0.06) \times 10^{-2} \text{ GeV}^3$	$(1.89 \pm 0.46) \times 10^{-2} \text{ GeV}^3$

The figure 4.6 shows one of the possible transitions through an intermediate color octet state: this diagram introduces in the cross-section the term

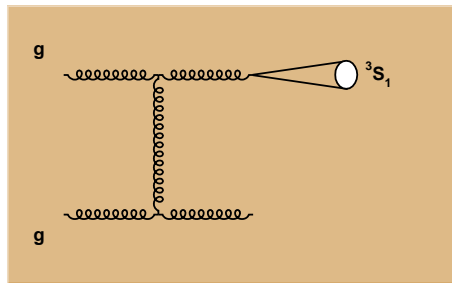


Figure 4.6: Feynman diagram describing a possible color octet transition in the hadroproduction of charmonium.

$$\frac{d\hat{\sigma}}{dp_T^2}(gg \rightarrow g c \bar{c} [{}^3S_1^{[8]}]) \langle \mathcal{M}^H [{}^3S_1^{[8]}] \rangle \sim \frac{\alpha_s^3}{p_T^4} v^4. \quad (4.6)$$

In figure 4.4, the solid line is the fitted curve including all possible color octet diagrams. From the fit results it is possible to assess the amount of color octet contribution needed to explain data (table 4.3).

## 4.2 Monte Carlo generation of $J/\psi$ in LHCb

In order to study the effects of NRQCD on the  $J/\psi$  production at LHCb, we compared samples of  $J/\psi$  from two different Monte Carlo productions, “DC06” versus “MC08”: the “DC06” production does not include color octet mechanisms, while the “MC08” test production has been generated including the color octet mechanisms. In the latter version has been possible to include in PYTHIA the new elementary processes foreseen from NRQCD theory, setting the matrix elements to realistic values: the amount of color octet model introduced in the Monte Carlo has been tuned on CDF data. In figure 4.7 the  $J/\psi$  differential cross-section measured from CDF is shown together with the simulation, in which color octet processes have been taken into account: the simulation reproduces quite well the data from CDF. In order to produce a coherent picture at the LHC energy, an extrapolation of the main phenomenological parameters, determined at lower energies, has been done.

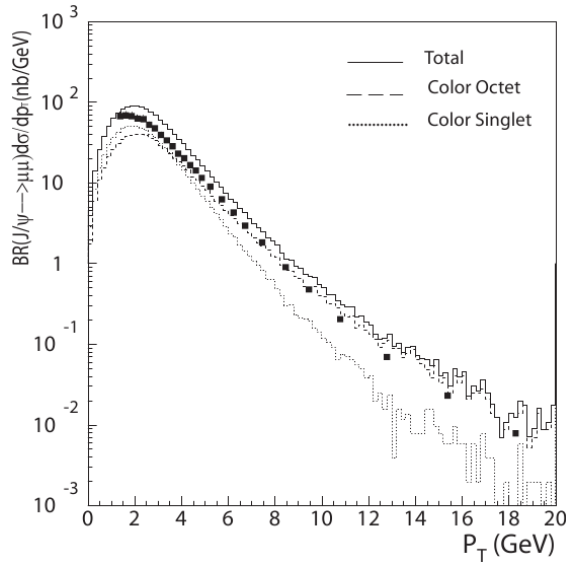


Figure 4.7: Superimposition of CDF data (black squares) with the Monte Carlo simulation. In the simulation, NRQCD matrix elements are tuned in such a way to reproduce the measurements of CDF. A good agreement is achieved.

We analyzed about 25000 inclusive  $J/\psi \rightarrow \mu^+\mu^-$  events for both productions, “DC06” and “MC08”, running the same selection algorithm in both cases. For the time being we will not discuss the details and the motivations of the selection criteria, which will be anyway addressed in the next chapter, rather we would like to highlight the difference we found in the two reconstructed samples.

$J/\psi$  have been reconstructed selecting pairs of oppositely charged tracks identified as muons and fitting them to a common vertex.

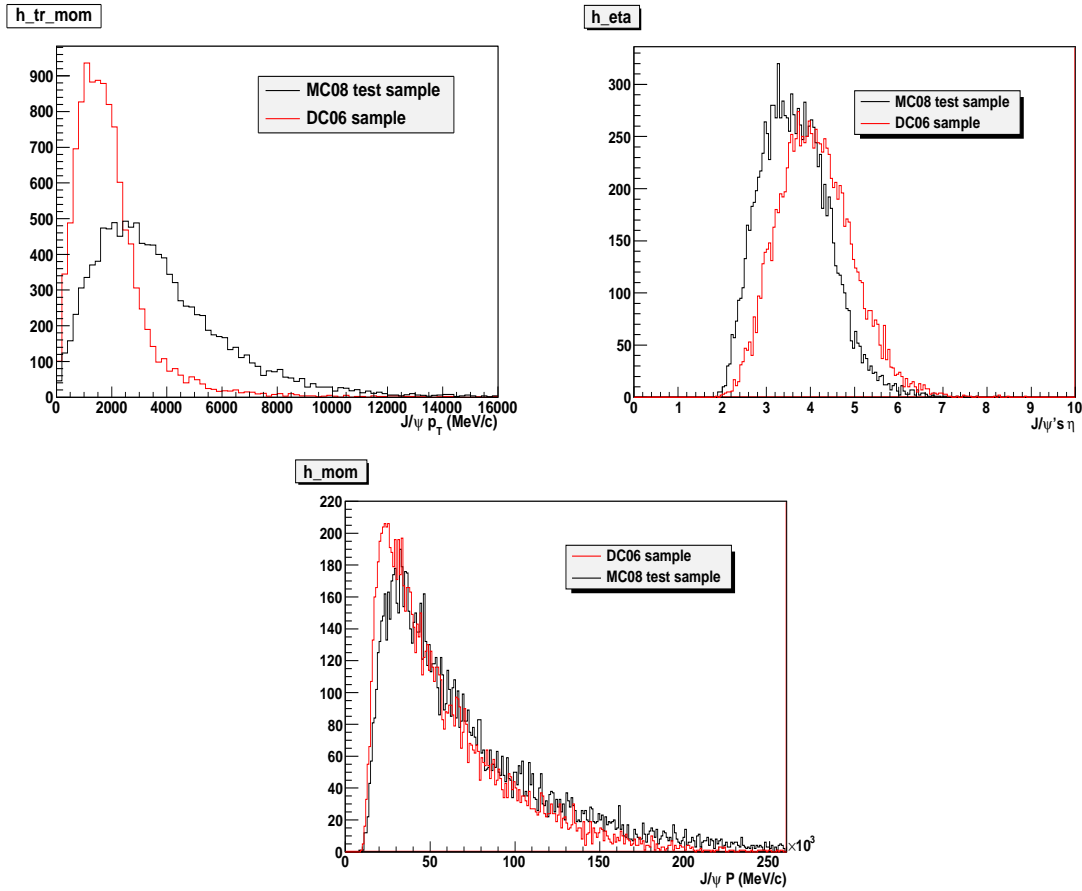


Figure 4.8: Comparison between “DC06” and “MC08” productions: (left, above)  $J/\psi(\mu^+\mu^-)$  transverse momentum distributions; (right, above)  $J/\psi(\mu^+\mu^-)$  pseudo-rapidity distributions; (below)  $J/\psi(\mu^+\mu^-)$  momentum distributions. The Monte Carlo production which includes the color octet model, is the “MC08” production.

For both selections a set of reference plots has been produced. The figure 4.8 shows the momentum transverse component (in the  $x$ - $y$  plane), the pseudo-rapidity and the momentum distributions of  $J/\psi$ . The pseudo-rapidity is defined as  $\eta = -\ln(\tan(\theta/2))$ ,  $\theta$  being the polar angle, namely the angle of the particle with respect to the beam axis. The transverse momentum is significantly increased for

the “MC08” sample and, as a consequence, the pseudo-rapidity is on average decreased: the color octet model production is characterized by less  $J/\psi$  close to the beampipe.

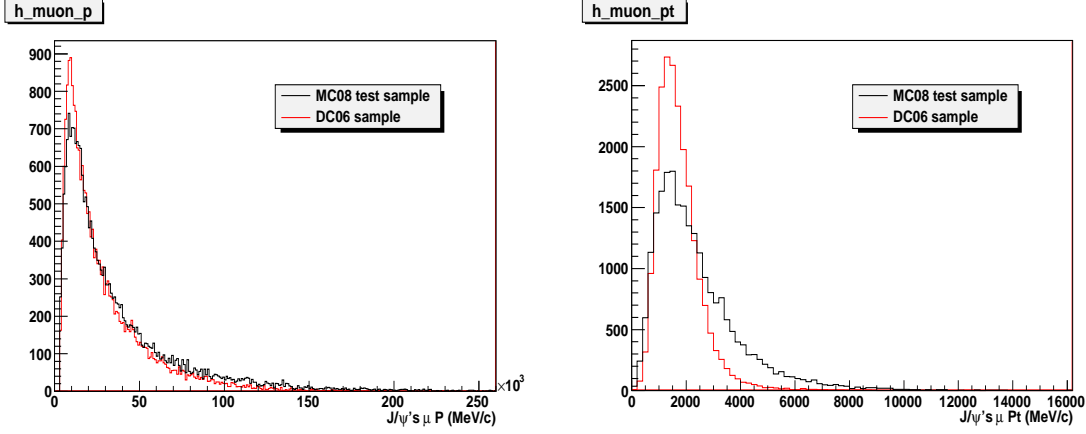


Figure 4.9: Comparison between “DC06” and “MC08” productions: (left)  $J/\psi$ ’s muon momentum distributions; (right)  $J/\psi$ ’s muon transverse momentum distributions. The average transverse momentum for the production that includes the color octet model, namely the “MC08” production, is significantly larger.

Table 4.4: Reconstructed  $J/\psi \rightarrow \mu^+\mu^-$  events for the two Monte Carlo productions “DC06” and “MC08”.

	<b>DC06</b>	<b>MC08</b>
Events processed	24911	24918
Events reconstructed	10695	11253
Candidate $J/\psi$	10902	11621
True $J/\psi$	10750	11291
True $J/\psi$ in $\pm 45 \text{ MeV}/c^2$	10041	10689
True $J/\psi$ in $\pm 45 \text{ MeV}/c^2$ & LO	7593	9521
Reconstruction ratio	$(42.9 \pm 0.3)\%$	$(45.2 \pm 0.3)\%$
Truth match ratio	$(98.6 \pm 0.1)\%$	$(97.2 \pm 0.2)\%$
LO efficiency	$(75.6 \pm 0.4)\%$	$(89.1 \pm 0.3)\%$

Finally, in figure 4.9, the momentum and transverse momentum distributions of muons from  $J/\psi$  are shown. While important differences in the momentum distributions are not found, the transverse momentum of muons is considerably harder for the color octet model production. Since the muons from  $J/\psi$  are the actual particles reconstructed in the detector, the fact that they have a higher transverse momentum distribution implies that, for the “MC08” production, the reconstruction global performances are better than the “DC06” performances. This finds confirmation in the table 4.4, where the number of events reconstructed for the

two samples are compared. The “True  $J/\psi$ ” are the  $J/\psi$  reconstructed and matching with a Monte Carlo true  $J/\psi$ . The requirement “... & L0” means that the events are required to pass the L0 trigger. The “Reconstruction ratio” is the ratio of the “Events reconstructed” to “Events processed”.

The differences between “DC06” and “MC08” are really significant: the most evident difference is in the L0 trigger efficiency which changes from 75.6% to 89.1%, due to the increase of the muon transverse momentum.

A similar comparison between Color Octet and Color Singlet  $\psi(2S)$  has not been possible because in the old version of Monte Carlo, “DC06” (the Color Singlet production), prompt  $\psi(2S)$  were not generated at all.

Table 4.5: Monte Carlo events used to perform our analyses.

Monte Carlo production	Sample type	Sample size used
DC06	inclusive $J/\psi \rightarrow \mu^+\mu^-$	$\sim 25$ k
DC06	minimum-bias (L0 triggered)	$\sim 2.2$ M
MC08 test production	inclusive $J/\psi \rightarrow \mu^+\mu^-$	$\sim 25$ k
MC09	inclusive $J/\psi \rightarrow \mu^+\mu^-$	up to $\sim 536$ k
MC09	inclusive $\psi(2S) \rightarrow \mu^+\mu^-$	$\sim 14$ k

In table 4.5 the different samples used in this thesis are given. The “DC06” Monte Carlo production has been used to make the comparison with the “MC08” test production (color singlet versus color octet  $J/\psi \rightarrow \mu^+\mu^-$ , as we have discussed in this section). “DC06” L0-stripped minimum-bias has been used to set the selection cuts (see chapter 5). The “MC08” was a transition production towards the “MC09”, the latest Monte Carlo production in LHCb. Inclusive  $J/\psi \rightarrow \mu^+\mu^-$  and  $\psi(2S) \rightarrow \mu^+\mu^-$  of such production have been used to perform most of the studies we will present in this thesis (pseudo proper time, efficiency, systematic errors).

Just in the latest version (“MC09”) of the LHCb Monte Carlo simulation has been possible to produce simultaneously prompt  $J/\psi$  and  $\psi(2S)$ . Nevertheless in the current simulation software, while for  $J/\psi$  all the NRQCD processes have been taken into account with the matrix elements tuned on CDF data, for  $\psi(2S)$  the only process  $g + g \rightarrow c\bar{c}[{}^3S_1^{[1]}] + g$  (color singlet) has been considered. This implies that the simulated  $\psi(2S)$  prompt cross-section results smaller than the expected value of a factor of about 3-4. Of course this can also affect the shape of some important kinematic distributions, such as  $p_T$ ,  $p$ , etc. The LHCb simulation software is still evolving and a description more complete and refined of the production processes will be needed in the near future.

### 4.3 Perspectives at LHC

In this section we want to discuss the charmonium production expectations at LHC and the cross-section settings in the LHCb Monte Carlo.

The results presented here have been, mostly, obtained including the most recent theoretical calculations and fits to CDF data. Despite the accuracy of the predictions we want to underline that the results are, sometimes, based on rather arbitrary theoretical assumptions.

Several studies have been carried out with PYTHIA 6.324, in which Color Octet Model processes have been included [52]: cross-sections have been calculated according to the different rapidity regions of the LHC experiments:

- $-2.5 < y < 2.5$  for the Atlas/CMS rapidity region;
- $1.8 < y < 4.9$  for the LHCb region.

The figure 4.10 shows the predicted  $J/\psi$  cross-section at LHC, times the branching ratio to  $\mu\mu$ , as a function of  $p_{T_0}$ .  $p_{T_0}$  is a phenomenological parameter tunable in PYTHIA. The total cross-section times the  $B_{\mu\mu} = (5.93 \pm 0.06)\%$  is ranging from  $5.5 \mu\text{b}$  to  $15 \mu\text{b}$ . The best agreement to CDF data seems to suggest a  $p_{T_0}$  value of  $2.85 \text{ GeV}/c$ .

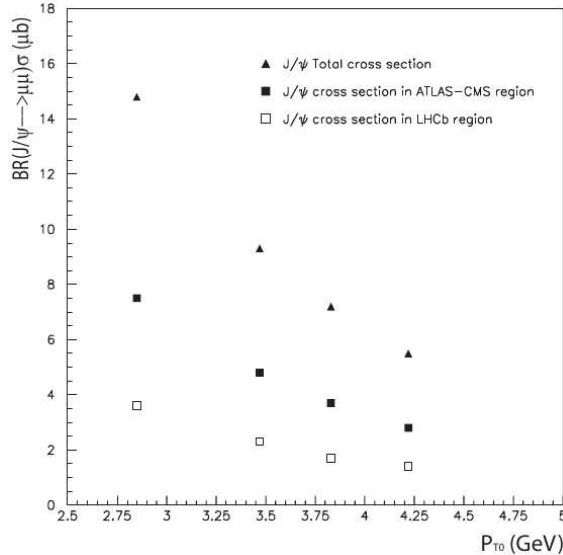


Figure 4.10: Total  $J/\psi$  cross-section times the branching ratio to  $\mu\mu$  as a function of  $p_{T_0}$ . The different symbols refer to the cross-sections calculated in different LHC acceptance regions, and to the total  $J/\psi$  cross-section integrated over the full solid angle.

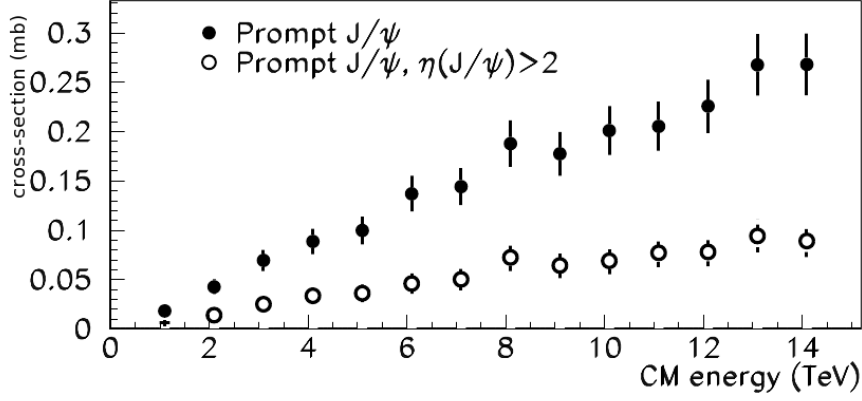


Figure 4.11: The plot shows the expected dependence of the  $J/\psi$  cross-section on the centre-of-mass energy.

If we assume the value of  $p_{T_0}$  suggested from CDF data, we get for LHC a  $J/\psi$  total cross-section of about  $250 \mu\text{b}$ . The figure 4.11 shows the expected dependence of the  $J/\psi$  production cross-section on the energy. At LHC will be possible to measure the cross-sections at different energies from 2 TeV up to 14 TeV. In the table 4.6 the  $J/\psi$  cross-sections resulting from the latest (“MC09”) LHCb Monte Carlo simulation, are shown.

Table 4.6: The  $J/\psi$  production cross-sections in the LHCb “MC09” Monte Carlo simulation.

	7+7 TeV	6+6 TeV
Inclusive $J/\psi$	$(0.262 \pm 0.002) \text{ mb}$	$(0.193 \pm 0.002) \text{ mb}$
Prompt $J/\psi$	$(0.233 \pm 0.002) \text{ mb}$	$(0.173 \pm 0.002) \text{ mb}$
$J/\psi$ from B	$(0.029 \pm 0.002) \text{ mb}$	$(0.020 \pm 0.002) \text{ mb}$

CDF has measured both the  $J/\psi$  and  $\psi(2S)$  cross-sections [45], [46]. They find in the rapidity range  $|y| < 0.6$

$$\sigma(p\bar{p} \rightarrow J/\psi X) = 4.08 \pm 0.02_{-0.33}^{+0.36} \mu\text{b} \quad (4.7)$$

$$\sigma(p\bar{p} \rightarrow H_b, H_b \rightarrow J/\psi X, p_T > 1.25 \text{ GeV}) = 0.330 \pm 0.005_{-0.033}^{+0.036} \mu\text{b} \quad (4.8)$$

respectively for inclusive  $J/\psi$  and for  $J/\psi$  from  $b$ -hadron, and

$$\sigma_i(p\bar{p} \rightarrow \psi(2S)X, p_T > 2 \text{ GeV})B'_{\mu\mu} = 3.14 \pm 0.04^{+0.23}_{-0.22} \text{ nb} \quad (4.9)$$

$$\sigma_p(p\bar{p} \rightarrow \psi(2S)X, p_T > 2 \text{ GeV})B'_{\mu\mu} = 2.60 \pm 0.05^{+0.19}_{-0.18} \text{ nb} \quad (4.10)$$

respectively for inclusive  $\psi(2S)$  and for prompt  $\psi(2S)$ . From such results, and taking into account the different  $p_T$  ranges in which the measurements have been done, it is possible to estimate a prompt cross-section ratio  $R_\psi = \sigma_{\psi'}/\sigma_\psi \simeq 13\%$ . CDF has provided also a measurement of the ratio  $\frac{\sigma_{\psi'}B'_{\mu\mu}}{\sigma_\psi B_{\mu\mu}}$  in each  $p_T$  bin (see figure 4.12). Both the prompt ratio and the ratio from  $b$  decays show an increase with  $p_T$ .

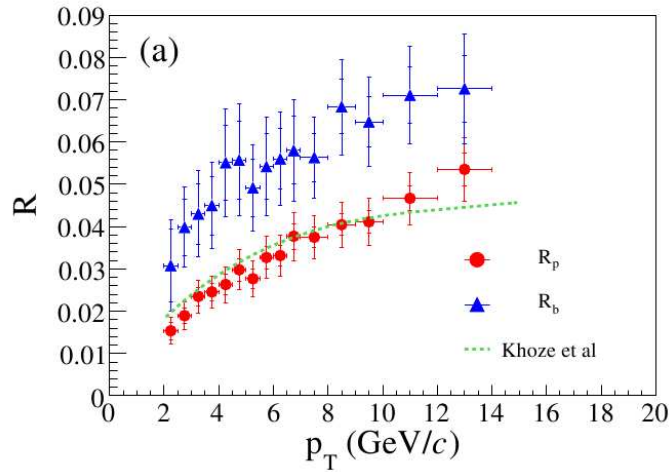


Figure 4.12: Ratio  $\frac{\sigma_{\psi'}B'_{\mu\mu}}{\sigma_\psi B_{\mu\mu}}$  measured from CDF. The subscript  $p$  ( $b$ ) refers to the prompt cross-sections (from  $b$ -hadron decays cross-sections).

In figure 4.13 we show the cross-section predictions for direct  $J/\psi$  and  $\psi(2S)$  productions as well as for the production of  $J/\psi$  from radiative  $\chi$  decays at the LHC. The theoretical curves include the statistical errors in the extraction of the NRQCD matrix elements. A measure of the  $\psi(2S)$  to  $J/\psi$  production ratio at LHCb has enormous significance as it allows, already with the first data, to verify the theoretical predictions of NRQCD.

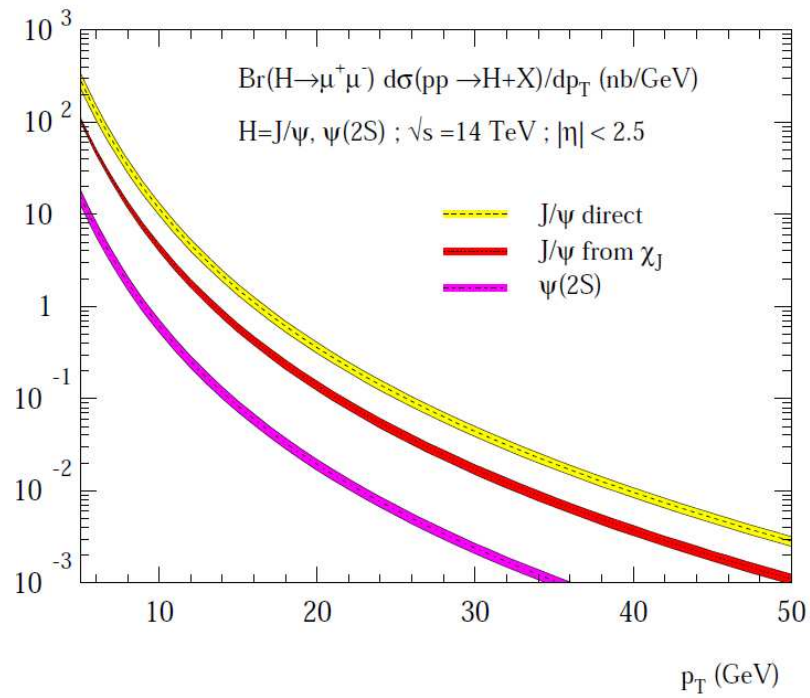


Figure 4.13:  $J/\psi$  and  $\psi(2S)$  differential cross-sections times the branching ratio to  $\mu\mu$  expected at LHC ( $\sqrt{s} = 14$  TeV, pseudo-rapidity cut  $|\eta| < 2.5$ ). Direct  $J/\psi$  and  $J/\psi$  from  $\chi_J$ , are shown separately.

## 4.4 The polarization of $J/\psi$ and $\psi(2S)$

As the bound states  $\psi$  are massive spin-1 particles, they have three polarizations. The polarization state of the charmonium can be deduced from the angular dependence of its decay into  $\mu^+\mu^-$ . The varying direction of the decay muon  $\mu^+$ , in the  $\psi$  rest frame, is measured with respect to a system of axes. Three different definitions of the *polarization axis*  $z$  identify three different reference frames (see figure 4.14):

- **helicity frame (HX):** charmonium momentum direction in the proton-proton ( $h_1 + h_2$ ) centre-of-mass frame
- **Gottfried-Jackson frame (GJ):** direction of one proton beam (per example  $h_1$ ) in charmonium rest frame
- **Collins-Soper frame (CS):** bisector between  $h_1$  and  $-h_2$  directions in charmonium rest frame.

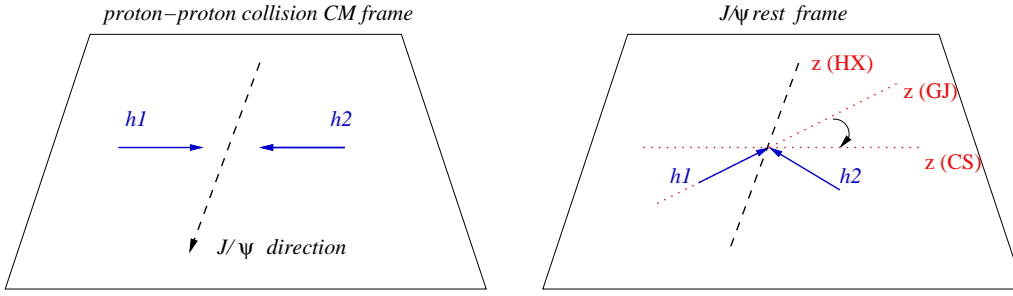


Figure 4.14: The picture shows the different frames definitions used to measure the  $\psi$  polarization.

The angular distribution of the  $\mu^+$  in the  $\psi$  rest frame with respect to the frame chosen (HX-CS-GJ) is given from

$$\frac{dN}{d(\cos\theta^*)d\varphi} \propto 1 + \lambda_\theta \cos^2\theta^* + \lambda_{\theta\varphi} \sin 2\theta^* \cos\varphi + \lambda_\varphi \sin^2\theta^* \cos 2\varphi \quad (4.11)$$

$\theta^*$  being the polar angle and  $\varphi$  being the azimuthal angle.  $\lambda_\theta = \alpha$ ,  $\lambda_{\theta\varphi}$  and  $\lambda_\varphi$  are the main polarization parameters. The interesting quantity is  $\lambda_\theta = \alpha$  which can vary in the range  $-1 \leq \alpha \leq +1$ :  $\alpha = 0$  means that the mesons are unpolarized,  $\alpha = +1$  corresponds to a full transverse polarization and  $\alpha = -1$  to a longitudinal polarization.

The polarization of  $J/\psi$  has been measured by several experiments. The present experimental picture is not so clear, as different experiments adopted different polarization frames to observe the decay angular distribution.

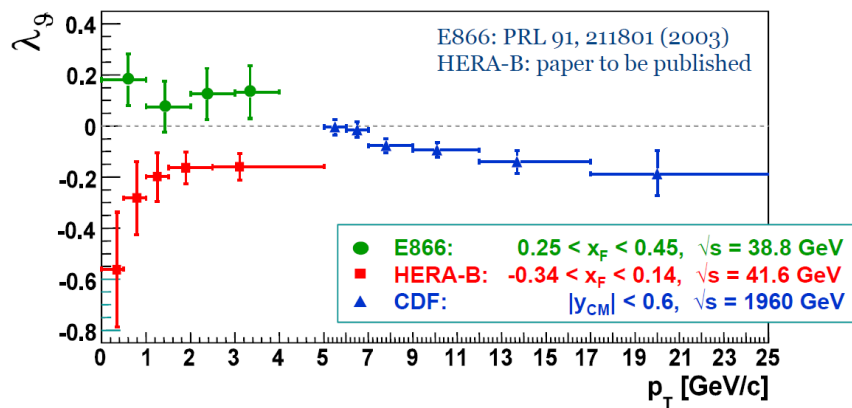


Figure 4.15: The plot shows the  $J/\psi$  polarization results obtained from the three experiments E866, HERA-B and CDF. The parameter measured  $\lambda_\theta$  corresponds to  $\alpha$ .

The choice of the reference frame crucially affects the results. While CDF has used for its analyses the HX frame, the experiment E866 used the CS frame and HERA-B used all the HX-GJ-CS frames. The figure 4.15 shows the results obtained from these experiments. The data look to be in mutual contradiction and the shape at low transverse momentum is rather unclear and ambiguous. Nevertheless the seemingly contradictory results can be consistently described assuming the same reference frame for all the measurements [47]. In particular the figure 4.16 shows how the polarization values measured by E866, HERA-B and CDF appear as a function of the momentum, if they are evaluated in the CS frame.

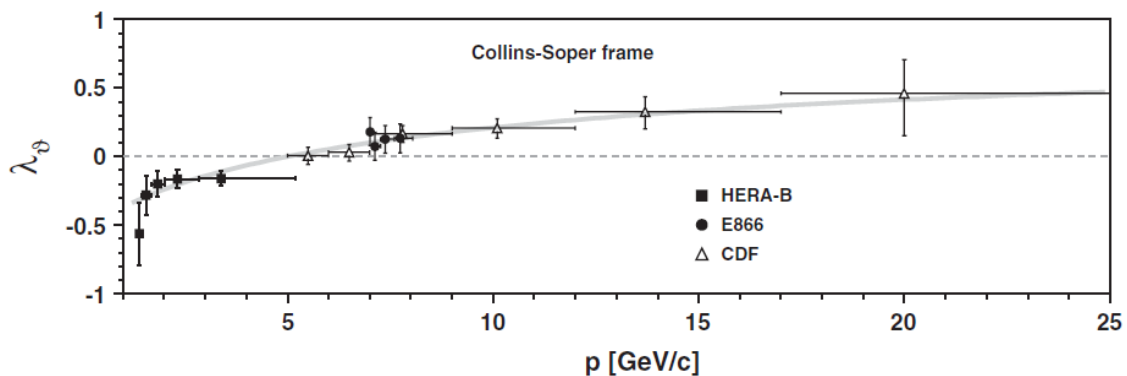


Figure 4.16: The plot shows the  $J/\psi$  polarization parameter  $\lambda_\theta = \alpha$  obtained by E866, HERA-B and CDF compared in the same reference frame (CS).

The most recent measurements of the  $\psi$  polarization, performed at HERA-B [51] with 920 GeV fixed-target proton-nucleus, have been done on all angular parameters and in all the reference frames (HX-GJ-CS) (see figure 4.17). The measure of the parameter  $\lambda_\theta$  above 1 GeV  $p_T$  in the helicity frame - asterisk markers - shows a negligible polarization while the same parameter in the Collins-

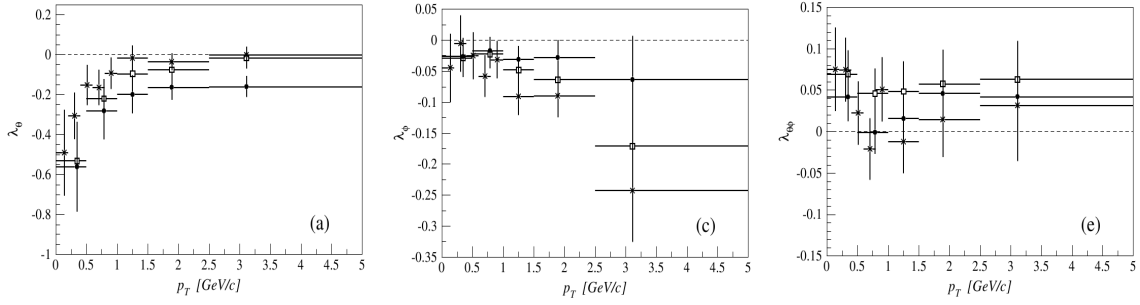


Figure 4.17: The plots show the parameters  $\lambda_\theta$ ,  $\lambda_\varphi$  and  $\lambda_{\theta\varphi}$  measured by the HERA-B experiment. The results obtained in the Collins-Soper, Gottfried-Jackson and helicity frames are represented, respectively, by black circles, white squares and asterisks. The vertical errors bars represent quadratic sums of statistical and systematic uncertainties. The horizontal bars indicate the adopted binning.

Soper frame - black circles - shows a polarization of about  $\lambda_\theta = -0.20$ , corresponding to a preferred longitudinal polarization state. Since the polarization definition itself depends on the frame in which is measured, the information contained in an analysis in which all the reference frames are considered, can help to understand possible discrepancies among the measures.

CDF has used the *helicity* frame to measure the distribution integrated over the azimuthal angle  $\varphi$ , getting informations on the parameter  $\lambda_\theta = \alpha$ . In the *helicity frame* the spin quantization axis lies along the charmonium momentum direction in the proton-proton centre-of-mass frame (see figure 4.18).

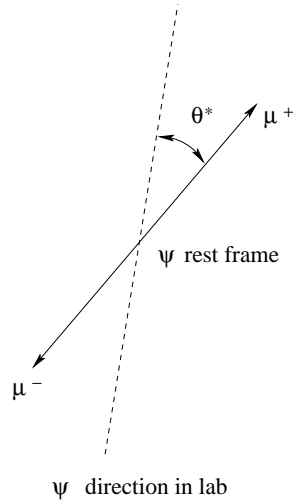


Figure 4.18: Definition of the angle  $\theta^*$  used to measure the polarization in the *helicity frame*.

The normalized angular distribution  $I(\cos \theta^*)$  is given by (for a derivation see the App. A of Ref. [48])

$$I(\cos \theta^*) = \frac{3}{2(\alpha + 3)}(1 + \alpha \cos^2 \theta^*). \quad (4.12)$$

The CDF measurement of the  $J/\psi$  and  $\psi(2S)$  spin alignment [49] is performed in the rapidity range  $|y| < 0.6$  with  $p_T \geq 5$  GeV, using data from  $p\bar{p}$  collisions at 1.96 TeV with an integrated luminosity of  $800 \text{ pb}^{-1}$ . Promptly-produced  $\psi$  mesons are isolated from those produced in heavy flavor decays by impact parameter selections on the two muon tracks. The analysis procedure employs simulations to account for acceptance and trigger efficiency effects. They used experimentally-derived trigger efficiency functions to produce the simulations.

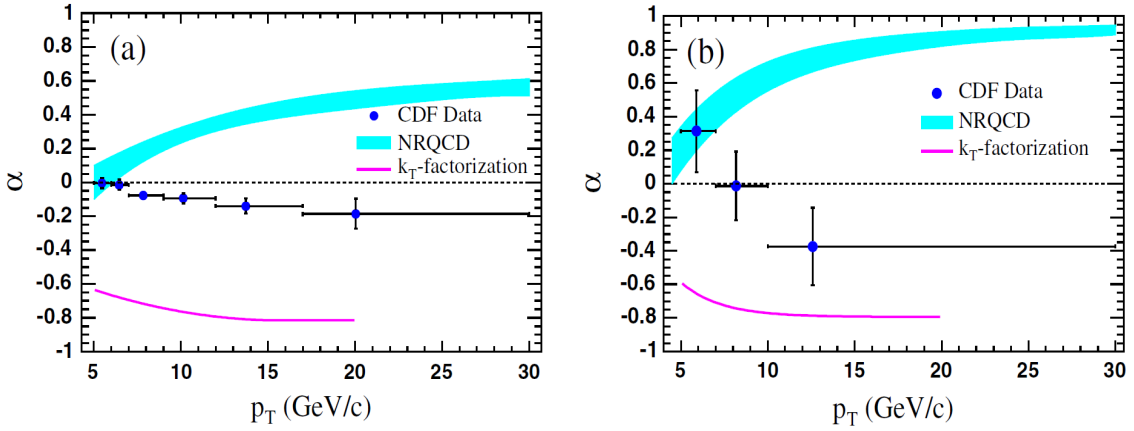


Figure 4.19: (a) Prompt  $J/\psi$  polarization as a function of  $p_T$ . (b) Prompt  $\psi(2S)$  polarization as a function of  $p_T$ . In both cases the prediction of NRQCD and  $k_T$ -factorization theories are also shown.

In figure 4.19 are shown the polarizations of prompt  $J/\psi$  and  $\psi(2S)$  mesons measured by CDF. For both vector mesons the polarizations become increasingly longitudinal as  $p_T$  increases from 5 to 30 GeV/c. The results are compared to the predictions of NRQCD and  $k_T$ -factorization model [50]: the data are in strong disagreement with the NRQCD prediction of large transverse polarization at high  $p_T$ . It is striking that the NRQCD calculations reproduce the measured  $J/\psi$  and  $\psi(2S)$  cross-sections at the Tevatron but fail to describe the polarization at high  $p_T$ . This indicates that there is some important aspect of the production mechanism that is not yet understood.

CDF has measured also the polarization of  $\psi$  vector mesons from  $b$ -hadron decays. For  $J/\psi$  they find  $\alpha_{eff} = -0.106 \pm 0.033(\text{stat}) \pm 0.007(\text{syst})$ . At this level of accuracy, a polarization contribution by  $J/\psi$  mesons from  $B_s$  and  $b$ -baryon decays cannot be separated from the effective polarization due to those from  $B_u$  and  $B_d$  decays.

They reported the first measurement of the  $\psi(2S)$  polarization from  $b$ -hadron decays:  $\alpha_{eff} = 0.36 \pm 0.25(\text{stat}) \pm 0.03(\text{syst})$ .



## Chapter 5

# Selection of $J/\psi \rightarrow \mu^+ \mu^-$ and $\psi(2S) \rightarrow \mu^+ \mu^-$ events in LHCb

---

In this chapter we will describe a selection of  $J/\psi \rightarrow \mu^+ \mu^-$ , to be run offline on reconstructed tracks. The selection criteria described here apply both to  $J/\psi$  and  $\psi(2S)$ . The sample used to optimize the selection cuts is a sample of L0-stripped minimum-bias events of the type “DC06”: L0-stripped means that in the simulation such events have successfully passed the L0 trigger.

The cross-sections used in the “DC06” production were:

$$\sigma_{tot} = 102.9 \pm 0.1 \text{ mb}$$

$$\sigma_{J/\psi}^{inc} = 0.286 \pm 0.002 \text{ mb}$$

for “total” and “inclusive  $J/\psi$ ” cross-sections respectively.

The sample size is represented by  $\sim 2.2$  M events (exactly 2216654 events); in the hypothesis in which the storage rate of 2 kHz was fully used to write L0-stripped minimum-bias events, the time needed to collect this sample would be about 1100 s at luminosity  $\mathcal{L} = 2 \times 10^{32} \text{ cm}^{-2} \text{ s}^{-1}$ . As we said in chapter 4 the  $\psi(2S)$  were not generated in this Monte Carlo sample, nevertheless, as we will see, the effect of the selection here defined will be evaluated on appropriate  $\psi(2S)$  samples also.

The selection consists of four cuts which are applied to a set of tracks identified as muons. Such set of tracks is called *Standard Loose Muons*: they are long tracks (see section 1.3.4) extrapolated to the muon system and for which the boolean variable `IsMuon` is equal to 1 (for a detailed description of the meaning of `IsMuon=1` see the section 2.5). The cuts apply on the combined DLL, on the product of the muon transverse momenta, on the  $\chi^2$  of the dimuon vertex and finally on the mass of the reconstructed  $\psi$  candidate.

### Combined DLL cut

In the track reconstruction each track is assigned a likelihood that it is a pion, kaon, proton, electron or muon using the information provided by the PID detectors, i.e. the RICH detectors, Calorimeters and Muon detectors (in the section 2.5 is discussed, per example, how the muon identification is provided by the muon system). The likelihood informations from the PID detectors can be combined in order to give the likelihood for a muon with respect to the pion hypothesis, which can be used to clean the sample of *Standard Loose Muons*:

$$DLL_{\mu\pi} = \ln(L_\mu) - \ln(L_\pi) = \ln\left(\frac{L_\mu}{L_\pi}\right) \quad (5.1)$$

where  $L_x$  is the likelihood of the  $x$  hypothesis. It is clear from equation 5.1 that a particle is more likely to be a muon than a pion for positive values of the combined  $DLL_{\mu\pi}$  and *vice versa*.

We have, initially, formed  $J/\psi(\mu^+\mu^-)$  starting just from *Standard Loose Muons* in a very wide mass region around  $J/\psi$  ( $\pm 1 \text{ GeV}/c^2$ ): 60596 dimuon pairs have been selected.

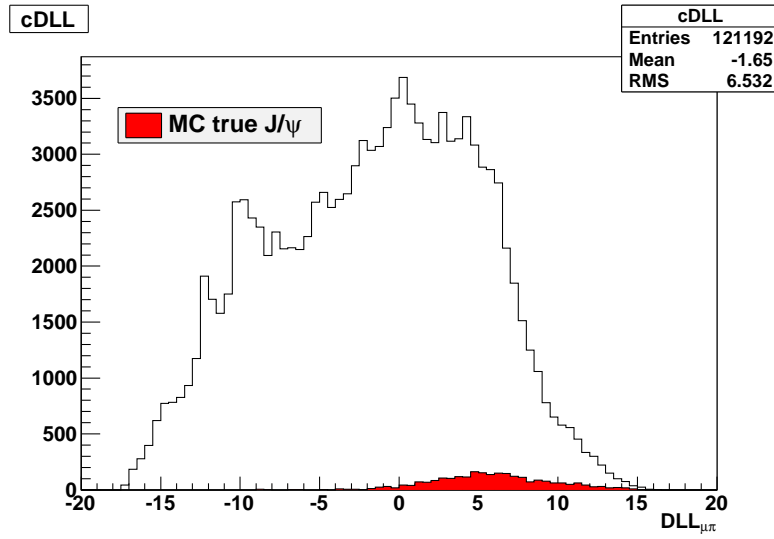


Figure 5.1: Combined  $DLL_{\mu\pi}$  for muons from dimuon pairs selected in the *Standard Loose Muons* set of tracks.

For such dimuon pairs, we construct the distribution of the combined  $DLL_{\mu\pi}$  shown in figure 5.1: each dimuon pair provides two entries in the histogram. The red histogram refers to the Monte Carlo truth matching  $J/\psi$ , hence it represents the true signal of  $J/\psi$ : it is evident that the cut  $DLL_{\mu\pi} > -3$  on both muons rejects a large part of the background without significant signal losses. The background is due, mostly, to pion flight decays and kaons which form “fake” dimuon pairs. The cut  $DLL_{\mu\pi} > -3$  has a signal efficiency of  $\sim 98\%$  and a background efficiency of  $\sim 32\%$ .

## Muon transverse momentum cut

One of the characteristics of charmonium is that the final decay products,  $\mu^+\mu^-$  in this case, typically have a larger transverse momentum than the background muons. A cut on  $p_T$  of the muons can therefore be used to reject the background. Different choices can be adopted, such as to cut on the  $p_T$  of one of the two muon candidates or to cut on  $p_T$  of both muons, etc. Each of these choices has a different effect on the efficiency. We have chosen to cut on the product of the muon transverse momenta after having noticed that the signal  $J/\psi$  identify in the plane  $(p_T^{\mu^+}, p_T^{\mu^-})$  an area limited inferiorly by a hyperbola,  $p_T^{\mu^+} \times p_T^{\mu^-} > 10^6$  (MeV/c)<sup>2</sup>, as can be seen in figure 5.2 (left). The right plot of the same figure shows clearly that the signal  $J/\psi$  are characterized from muons with product  $p_T^{\mu^+} \times p_T^{\mu^-} > 10^6$  (MeV/c)<sup>2</sup>. The cut  $p_T^{\mu^+} \times p_T^{\mu^-} > 10^6$  (MeV/c)<sup>2</sup> has a signal efficiency of  $\sim 99\%$  and a background efficiency of  $\sim 66\%$ .

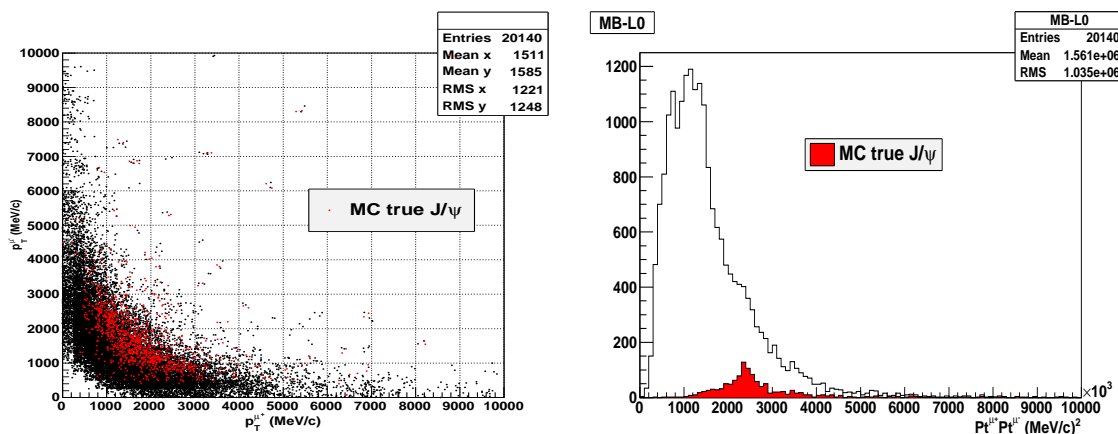


Figure 5.2:  $p_T^{\mu^+}$  versus  $p_T^{\mu^-}$  distribution (left).  $p_T^{\mu^+} \times p_T^{\mu^-}$  distribution (right). The red histograms are filled only if a Monte Carlo true  $J/\psi$  matches the selected dimuon pair.

## Vertex $\chi^2$ cut

In order to form  $J/\psi$  the two selected muons,  $\mu^+$  and  $\mu^-$ , are fitted to a common vertex. In doing that the muon momenta are re-calculated with the constraint to originate from the same vertex. The goodness of the fit is measured by the vertex  $\chi^2$ , which is typically small for tracks originating from the same vertex compared to tracks that do not.

The figure 5.3 shows the vertex  $\chi^2$  distribution for the dimuon pairs surviving the previous cuts (combined  $DLL_{\mu\pi} > -3$  and  $p_T^{\mu^+} \times p_T^{\mu^-} > 10^6$  (MeV/c)<sup>2</sup>). Most of the signal  $J/\psi$  have  $\chi^2 < 10$ , therefore this cut can be used to reject combinations of muons with a bad common vertex fit.

The cut on vertex  $\chi^2 < 10$  has a signal efficiency of  $\sim 98.5\%$  and a background efficiency of  $\sim 66\%$ .

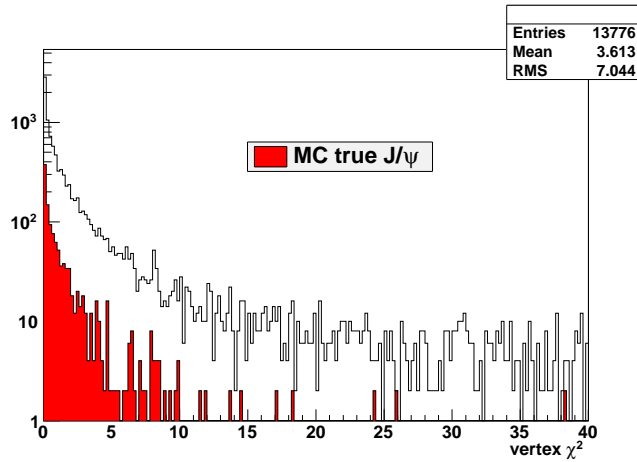


Figure 5.3: Vertex  $\chi^2$  distribution. The red histogram is filled only if a Monte Carlo true  $J/\psi$  matches the selected dimuon pair.

To estimate the background in the signal region from the shape of the mass distribution, one needs to keep sufficiently large sidebands. Therefore we will require the mass of the dimuon pair to be within  $450 \text{ MeV}/c^2$  of the PDG value of the  $J/\psi$  mass. The mass distribution will be, then, fitted with appropriate functions and the parameter values returned by the fit will be used to estimate the signal and the background in a region, typically  $\pm 3.5\sigma$  wide, around the PDG  $J/\psi$  mass value. In figure 5.4 the dimuon invariant mass distribution in the range  $|M_{\mu\mu} - M_{J/\psi}^{PDG}| < 450 \text{ MeV}/c^2$  is shown. The width of the mass peak is due to the experimental resolution.

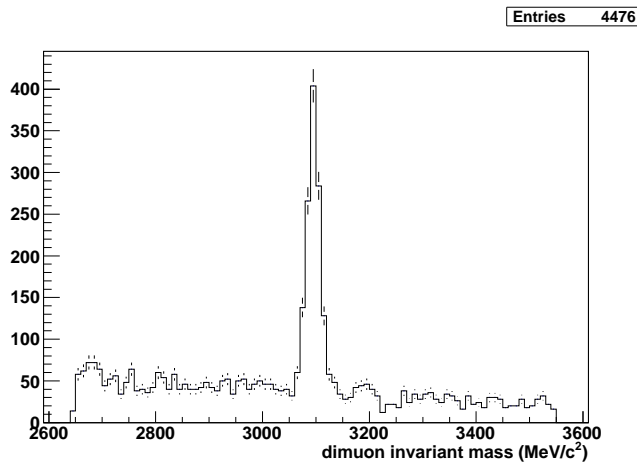


Figure 5.4: The figure shows the dimuon invariant mass distribution for the selected dimuon pairs in the mass window  $\pm 450 \text{ MeV}/c^2$  around the  $J/\psi$ . The bin size corresponds to  $10 \text{ MeV}/c^2$ .

### Mass cut

The final cut on the mass,  $|M_{\mu\mu} - M_{J/\psi}^{PDG}| < 45 \text{ MeV}/c^2$ , that as we will see corresponds to require the mass to be  $\pm 3.5\sigma$  around the PDG  $J/\psi$  mass value, has a signal efficiency of  $\sim 94\%$  and a background efficiency of  $\sim 4\%$ .

In table 5.1 the selection cuts and the respective efficiencies are given. The tight requirement for the track to be a muon,  $DLL_{\mu\pi} > -3$ , and the vertex  $\chi^2$  cut,  $\chi^2 < 10$ , guarantee a good quality of the selected tracks.

Table 5.1: Selection cuts efficiencies for  $J/\psi \rightarrow \mu^+\mu^-$  in L0-stripped minimum-bias events.

Cut	Signal efficiency (%)	Background efficiency (%)
$DLL_{\mu\pi} > -3$	$97.9 \pm 0.4$	$31.9 \pm 0.2$
$p_T^{\mu^+} \times p_T^{\mu^-} > 10^6 \text{ (MeV}/c)^2$	$99.0 \pm 0.3$	$66.4 \pm 0.3$
common vertex $\chi^2 < 10$	$98.5 \pm 0.4$	$66.0 \pm 0.4$
mass cut $\pm 45 \text{ MeV}/c^2 (\pm 3.5\sigma)$	$93.7 \pm 0.7$	$4.1 \pm 0.2$
all cuts	$89.5 \pm 0.9$	$0.57 \pm 0.03$

## 5.1 Extraction of signal

In the previous section, the cuts for a selection of  $J/\psi(\mu^+\mu^-)$  have been optimized making use of the Monte Carlo truth in order to reject the background without significant signal losses. Now we want to describe how to extract the signal and the background from experimental data once the mass distribution is reconstructed.

The number of signal  $J/\psi$  has to be extracted fitting the mass distribution with appropriate functions. The signal can be adequately described with a gaussian curve while the background with an exponential curve:

$$f(x) = p_0 \exp\left(-\frac{1}{2} \left(\frac{x - p_1}{p_2}\right)^2\right) + p_3 \exp\left(-\frac{x}{p_4}\right) \quad (5.2)$$

with  $p_0, p_1, p_2, p_3$  and  $p_4$  to be determined by the fit. The fit has been performed on the mass distribution of figure 5.4 and the result is shown in figure 5.5.

The mass resolution is  $p_2 = \sigma = (12.7 \pm 0.4) \text{ MeV}/c^2$ .

The integral of the fitted curve in the mass window  $\pm 45 \text{ MeV}/c^2$  ( $\sim \pm 3.5\sigma$ ) around the  $J/\psi$  provides:

$$S + B = 1404 \pm 37$$

where  $S + B$  is the sum signal plus background. The background extracted from the mass sidebands results to be

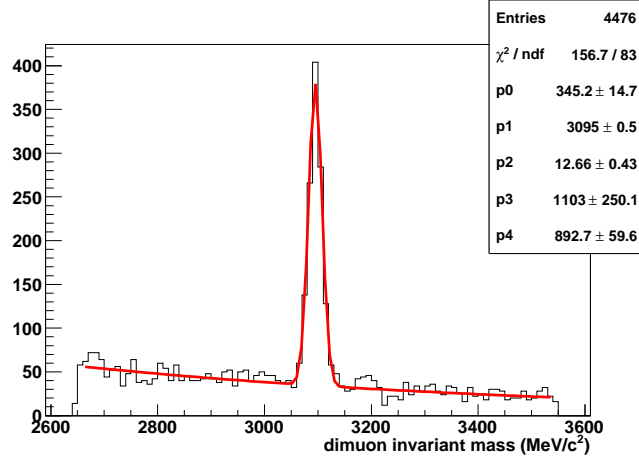


Figure 5.5: The figure shows the dimuon invariant mass distribution fitted with the function of equation 5.2. The signal is described from a gaussian and the background from an exponential. The mass resolution is given from  $p_2 = \sigma = (12.7 \pm 0.4) \text{ MeV}/c^2$ .

$$B = 313 \pm 20,$$

thus the signal estimated is

$$S = (S + B) - B = 1091 \pm 42.$$

The number of signal  $J/\psi$  given from Monte Carlo truth is  $\text{MC}_{sig} = 1106$ . The ratio signal over background in the signal region is  $S/B = 3.49 \pm 0.26$ .

The  $\psi(2S)$  was not generated in the Monte Carlo sample used here (“DC06” L0-stripped minimum-bias events), therefore is not possible to see any mass peak around the PDG  $\psi(2S)$  mass value:  $(3686.09 \pm 0.04) \text{ MeV}/c^2$ . Since the mass difference  $M_{\psi(2S)}^{PDG} - M_{J/\psi}^{PDG}$  is just  $\sim 590 \text{ MeV}/c^2$  and, as we will show, they have very similar kinematic properties, the dimuon selection here described for  $J/\psi$  can be used also for  $\psi(2S)$ , appropriately shifting the mass window around the  $\psi(2S)$  mass. In the next chapter we will study in detail the effect of such a selection on both  $J/\psi$  and  $\psi(2S)$  signals, using appropriate Monte Carlo samples.

Concerning the current sample, we can only give an estimation of the signal over background ratio expected in a region  $\pm 45 \text{ MeV}/c^2$  around the  $\psi(2S)$ . The  $\psi(2S)(\mu^+\mu^-)$  signal, can likely be about 2% of the  $J/\psi(\mu^+\mu^-)$  signal, as indicated by recent measurements [54]. In this case the signal over background ratio in the  $\psi(2S)$  signal region would be  $S/B = 0.16$ .

### 5.1.1 Disentangling prompt charmonia

The selection described in the previous sections allows to select  $\psi$  mesons in the decay channel  $\mu^+\mu^-$  starting from tracks reconstructed in the detector and identified as muons. The events in the mass peak are *prompt*  $\psi$ , *non-prompt*  $\psi$  and combinatorial background. Since we are interested in measuring the prompt component, a fundamental step of the analysis is the disentanglement of the *prompt*  $\psi$ . A distinctive feature of the *non-prompt*  $\psi$  production pattern is a measurable distance between the production vertex and the decay vertex due to the  $B$  meson flight distance.

The proper time of a particle is defined as

$$\tau = \frac{(\vec{V}_2 - \vec{V}_1) \cdot \vec{P}}{P^2 c} M \quad (5.3)$$

where  $\vec{V}_2$  is the decay vertex,  $\vec{V}_1$  is the production vertex,  $\vec{P}$  and  $M$  are respectively the momentum and the mass of the particle and  $c$  is the speed of light. When the particle is a  $J/\psi$  or a  $\psi(2S)$ , of course the physical meaning of the quantity of equation 5.3 is not exactly the proper time of the  $b$ -hadron, because the momentum and the mass refer to the  $J/\psi$  or  $\psi(2S)$ . Nevertheless this quantity is a good approximation of the  $b$ -hadron proper time and can be used to disentangle the prompt from the non-prompt component of charmonia.

Let us consider Monte Carlo inclusive  $J/\psi \rightarrow \mu^+\mu^-$  and Monte Carlo inclusive  $\psi(2S) \rightarrow \mu^+\mu^-$  (the samples used here are of the type ‘‘MC09’’ production, namely the latest LHCb simulation production). Each of these events has been reconstructed because, at the generator level, has been produced a  $J/\psi$  ( $\psi(2S)$ ) whose decay muons have fallen in a portion of solid angle defined by  $10 < \theta < 400$  mrad and  $p_z > 0$ . Should not surprise that just a fraction of such  $J/\psi$  ( $\psi(2S)$ ) are effectively reconstructed and selected: this is due, mainly, to the real detector acceptance which does not exactly coincide with the geometric requirement made above.

Since, for such samples, most of selected  $\psi$  are true signal and only a minor part is background (the ratio signal over background is typically  $\sim 100$ ), it is possible to build the  $\tau$  distribution for a sufficiently large signal statistics and to study the probability density functions shape.

In the figures 5.6 and 5.7, the  $\tau$  distribution for  $J/\psi \rightarrow \mu^+\mu^-$  and  $\psi(2S) \rightarrow \mu^+\mu^-$  respectively, selected in a  $\pm 45$  MeV/ $c^2$  mass window, are shown. The events selected have successfully passed the L0 trigger also. The signal has been separated from the background requiring the Monte Carlo match with a true  $J/\psi$  ( $\psi(2S)$ ): this allow us to study the shape of the signal separately from the shape of the background.

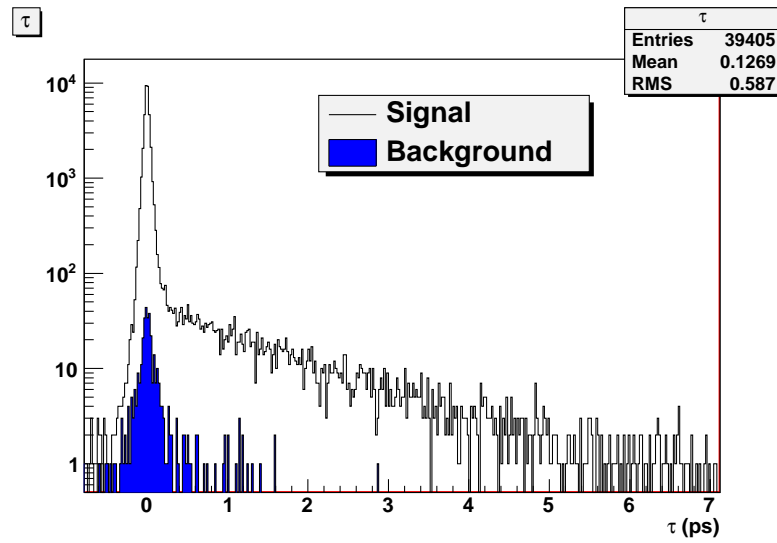


Figure 5.6:  $\tau$  distribution for selected  $J/\psi \rightarrow \mu^+\mu^-$ . The signal and background separation is obtained requiring the Monte Carlo match with a true  $J/\psi$ . The events have successfully passed the L0 trigger. The bin size corresponds to 0.02 ps.

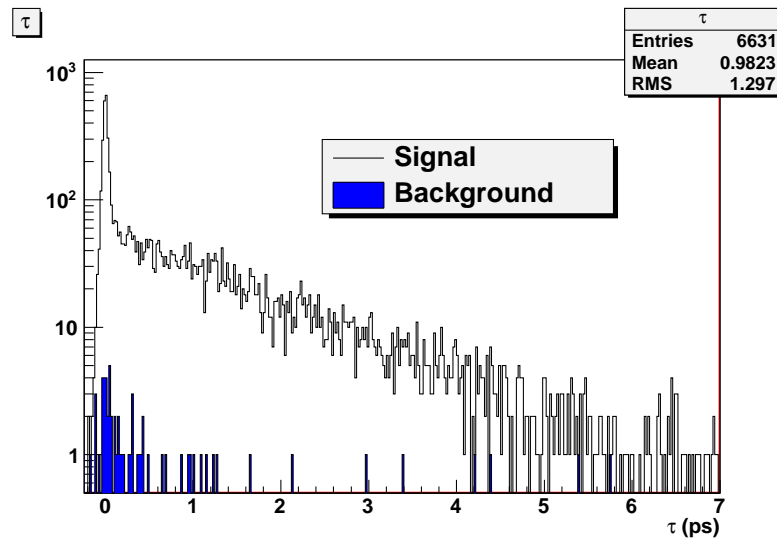


Figure 5.7:  $\tau$  distribution for selected  $\psi(2S) \rightarrow \mu^+\mu^-$ . The signal and background separation is obtained requiring the Monte Carlo match with a true  $\psi(2S)$ . The events have successfully passed the L0 trigger. The bin size corresponds to 0.02 ps.

The signal  $\tau$  distribution is characterized by a sharp peak at zero and a long tail for positive values of  $\tau$ . The peak at zero is due to the superimposition of prompt  $J/\psi$  ( $\psi(2S)$ ), which are produced and decay in the primary vertex, and  $J/\psi$  ( $\psi(2S)$ )

coming from short-lived  $b$ -hadron decays. The width of this peak is due to the experimental resolution. The long tail events are  $J/\psi$  ( $\psi(2S)$ ) from long-lived  $b$ -hadron decays.

The background  $\tau$  distribution gives its main contribution in the prompt part of the spectrum.

Obviously, in the real life it is not possible to distinguish background from signal events, therefore the  $\tau$  distribution will be the sum of both the components and the fit should adequately take into account the background. The shape we used to fit the  $\tau$  distribution (signal + background) is given from

$$f(x) = \begin{cases} p_0 \exp(-\frac{1}{2}(\frac{x-p_1}{p_2})^2) + p_3 \exp(-\frac{1}{2}(\frac{x-p_4}{p_5})^2) & \text{if } x < 0 \\ p_0 \exp(-\frac{1}{2}(\frac{x-p_1}{p_2})^2) + p_3 \exp(-\frac{1}{2}(\frac{x-p_4}{p_5})^2) + \exp(p_6 + p_7x) & \text{if } x \geq 0. \end{cases} \quad (5.4)$$

The gaussian curves are used to fit the peak at zero and the exponential curve is used to fit the long tail. For  $J/\psi$ , nevertheless, the superimposition of well three gaussian curves has been needed to describe adequately the peak at zero. The number of parameters for  $J/\psi$ , hence, is 11: 3 parameters per each of the three gaussians and 2 parameters for the exponential. The fitted distributions are shown in figures 5.8 and 5.9.

The mean *pseudo* proper times obtained from fit,

$$\tau_0 = \frac{1}{|p_{10}|} = (1.47 \pm 0.04) \text{ ps} \quad \text{for } J/\psi, \quad \tau_0 = \frac{1}{|p_7|} = (1.49 \pm 0.03) \text{ ps} \quad \text{for } \psi(2S),$$

are a good approximation of the  $b$ -hadron proper time: the current PDG value [53] for the  $B^\pm/B^0/B_s^0/b$ -baryon admixture mean life is  $(1.568 \pm 0.009)$  ps. We would like to remark that the aim of this work is not to measure the  $B$  proper time, rather we want to build a *pseudo* proper time variable which allows to separate the prompt from non-prompt component of charmonium.

In order to get the total number of events from  $b$ -decays, the exponential positive tail of  $\tau$  distribution is integrated between zero and plus infinite. The  $b$ -fractions estimated in this way are

$$F(J/\psi, \text{ from } b) = (8.3 \pm 0.2)\% \quad F(\psi(2S), \text{ from } b) = (63.2 \pm 1.0)\%.$$

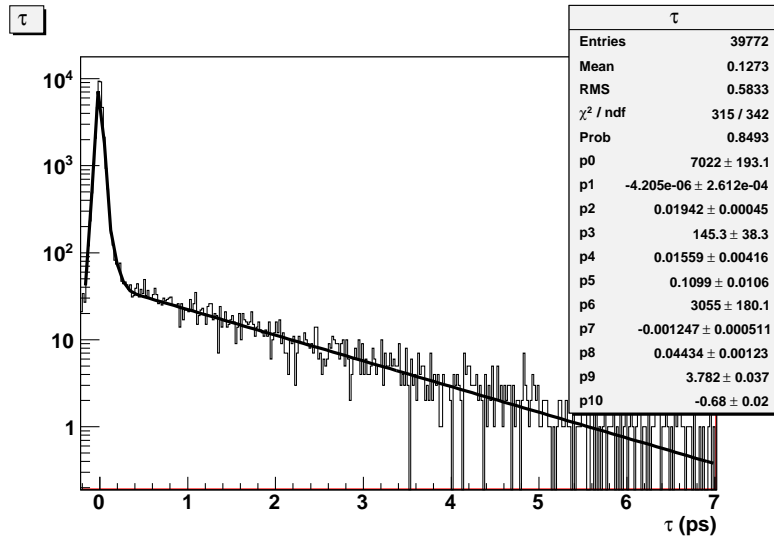


Figure 5.8:  $\tau$  total distribution (signal + background) for selected  $J/\psi \rightarrow \mu^+\mu^-$  which have successfully passed the L0 trigger. The fit is performed with three Gaussians for the peak at zero and an exponential for the tail. The bin size corresponds to 0.02 ps.

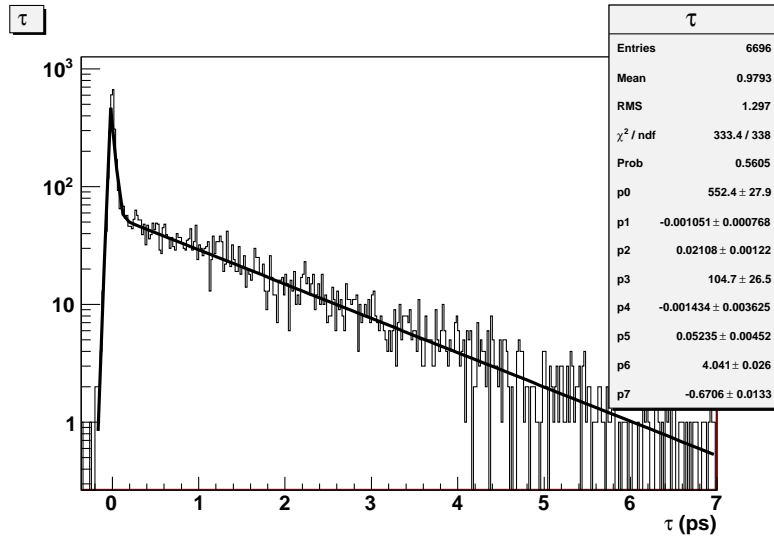


Figure 5.9:  $\tau$  total distribution (signal + background) for selected  $\psi(2S) \rightarrow \mu^+\mu^-$  which have successfully passed the L0 trigger. The fit is performed with the function of equation 5.4 and the bin size corresponds to 0.02 ps.

CDF has measured the  $b$ -hadron fractions for  $J/\psi$  and  $\psi(2S)$  [45], [46].  $F_{\text{CDF}}(J/\psi, \text{from } b)$  varies in the  $p_T$  range 1.25-20 GeV/c from  $9.4 \pm 1\%$  at low  $p_T$ , up to  $46.4 \pm 4.5\%$  at high  $p_T$ .

$F_{\text{CDF}}(\psi(2S), \text{from } b)$  varies in the  $p_T$  range 2-30 GeV/c from  $13.3 \pm 1.9\%$  at low  $p_T$ , up to  $39.1 \pm 10.6\%$  at high  $p_T$ .

The reason for which the  $\psi(2S)$   $b$ -fraction we get is considerably larger than the expected values, is due to the fact that in our Monte Carlo the prompt cross-section for  $\psi(2S)$  is smaller than the expected value, because, as already mentioned in the previous chapter, only the color singlet production process has been considered. The LHCb simulation software is still evolving and further improvements are necessary: the Monte Carlo needs to be tuned on real data; only real data can give us the correct  $b$ -hadron fractions at the LHC energies.

The  $\tau$  distribution will be inevitably “polluted” by the background survived the selection. Hence it will be needed a detailed study of the shape of the background and of other possible components in the distribution, given per example from primary vertex wrong associations. The shape of the background in the  $\tau$  distribution can be inferred from real data, per example, studying the shape of  $\tau$  distribution of sideband events, while the shape of possible components due to wrong associations among primary and decay vertexes can be deduced making the vertex association between the  $\psi$  meson decay vertex and the primary vertex of a different bunch-crossing event.



## Chapter 6

# The measurement of the $\psi'$ to $J/\psi$ production ratio

---

At LHCb a large number of  $J/\psi$  and  $\psi'$  will be collected very soon after the LHC start. Given the abundance of such resonances in the collisions (we expect about 18000  $J/\psi \rightarrow \mu^+\mu^-$  and about 360  $\psi(2S) \rightarrow \mu^+\mu^-$  produced per  $\text{nb}^{-1}$  at 7+7 TeV and 60% of such numbers at 3.5+3.5 TeV), the statistical error on the cross-sections measurements will be reduced under 10% with  $5 \text{ pb}^{-1}$  of data from LHCb.

In LHCb there is great interest around the measurement of the  $J/\psi$  cross-section, both for prompt  $J/\psi$  and for  $J/\psi$  from  $b$ -hadron decay. These measurements are important for later analysis steps in LHCb: they aim to open the road to the  $b$ -physics with  $J/\psi$  and dimuon modes. Despite such measurements can be considered as first publication measurements, they require the knowledge of the integrated luminosity, the acceptance, the trigger, reconstruction and selection efficiencies. While the geometrical acceptance given from Monte Carlo can already be considered as a reliable determination, for the efficiencies introduced by the trigger, the reconstruction and selection, the situation is a bit more delicate: we need to correct them with the real efficiencies from real data. This certainly gives an added value to the measurement but requires a detailed check of Monte Carlo.

In the measurement of the  $\psi'$  to  $J/\psi$  production ratio, performed exploiting the dimuon decay mode, the integrated luminosity cancels out. Moreover since the two resonances have very similar kinematic properties and a relatively small mass difference ( $\sim 590 \text{ MeV}/c^2$ ), one would expect that the efficiencies and the main systematic errors cancel out in the ratio. This measurement requires less inputs from Monte Carlo and does not need the luminosity. The ratio  $\psi'$  to  $J/\psi$  measured with very first data, will be useful to do cross-checks with the absolute cross-section measurements.

The different types of production of  $J/\psi$  and  $\psi'$  are listed and described below:

- *prompt*: is the fraction of  $\psi$  mesons not coming from the decay of a  $b$ -hadron. Such  $\psi$  decay immediately in the primary vertex. They can be *direct* or *indirect*.
  - *direct*: is the component of the *prompt* fraction produced directly in the  $pp$  interaction.
  - *indirect*: is the component of the *prompt* fraction produced indirectly, namely, coming from the decay of a heavier charmonium state.
- *non-prompt*: is the fraction of  $\psi$  mesons coming from the decay of a  $b$ -hadron. Such  $\psi$  decay, in general, in a vertex detached from the primary vertex.

All the components listed above contribute in forming the ones we call “inclusive  $pp \rightarrow \psi(\mu^+\mu^-) + X$  events”, where  $\psi = J/\psi, \psi(2S)$ . In the measurement of the  $\psi(2S)$  to  $J/\psi$  production ratio we are interested in the prompt component.

The following expressions for the cross-sections are used:

$$\sigma_{\psi(2S)} = \sigma_{\psi(2S)}^D \quad (6.1)$$

$$\sigma_{J/\psi} = \sigma_{J/\psi}^D + \sum_{J=0}^2 Br(\chi_{cJ} \rightarrow J/\psi\gamma)\sigma_{\chi_{cJ}}^D + Br(\psi(2S) \rightarrow J/\psi X)\sigma_{\psi(2S)} \quad (6.2)$$

$$R_{\psi} = \frac{\sigma_{\psi(2S)}}{\sigma_{J/\psi}} \quad (6.3)$$

where the superscript  $D$  refers to the direct contribution. The equations 6.1 and 6.2 represent the prompt component of  $\psi(2S)$  and  $J/\psi$ . While for  $\psi(2S)$  the prompt component corresponds to the direct component, for  $J/\psi$  does not because of the presence of not negligible decays from heavier charmonium states: *prompt*  $J/\psi$  can be *direct* or produced *indirectly* from the decay of a resonance  $\chi_{cJ}$  or  $\psi(2S)$  with the branching ratios reported in table 4.2. Other decays to  $J/\psi$  or  $\psi(2S)$  from heavier states of charmonium have negligible branching ratios or are not permitted.

The ratio  $R_{\psi}$  of equation 6.3 is the prompt cross-section ratio between  $\psi(2S)$  and  $J/\psi$  and represents the quantity we want to measure. In the following we will describe how to perform this measurement in the dimuon decay channel.

The number of prompt  $\psi(2S)$  mesons,  $N_{\psi'}$  ( $J/\psi$  mesons,  $N_{\psi}$ ), triggered, reconstructed and offline selected after a time  $t$  of data taking, is given from

$$N_{\psi'} = \sigma_{\psi(2S)} B'_{\mu\mu} \left( \int \mathcal{L} dt \right) \epsilon', \quad N_{\psi} = \sigma_{J/\psi} B_{\mu\mu} \left( \int \mathcal{L} dt \right) \epsilon \quad (6.4)$$

where  $B'_{\mu\mu}$  ( $B_{\mu\mu}$ ) is the dimuon branching ratio for  $\psi(2S)$  ( $J/\psi$ ),  $\int \mathcal{L} dt$  is the integrated luminosity and  $\epsilon'$  ( $\epsilon$ ) is the global experimental efficiency for  $\psi(2S)$  ( $J/\psi$ ). The efficiency factors  $\epsilon$  and  $\epsilon'$  take into account the geometrical acceptance of the detector, the efficiency due to the reconstruction (tracking efficiency, muon identification efficiency, vertex reconstruction efficiency), the trigger efficiency and the efficiency of the offline selection.

From the previous equations it follows that

$$R_\psi = \frac{\sigma_{\psi(2S)}}{\sigma_{J/\psi}} = \frac{N_{\psi'}}{N_\psi} \frac{B_{\mu\mu}\epsilon}{B'_{\mu\mu}\epsilon'} \quad (6.5)$$

thus the ratio of the prompt cross-sections is given from the ratio  $N_{\psi'}/N_\psi$  appropriately corrected by the branching fraction ratio and by the efficiency ratio. While the numbers  $N_{\psi'}$  and  $N_\psi$  are deduced by experimental data, as shown in chapter 5, through a fit of the invariant mass and of the *pseudo* proper time in order to extract the prompt component of the signal, the efficiency ratio has to be inferred by Monte Carlo simulations. Nevertheless, as we will describe in the following, some components of the global efficiency, such as the tracking efficiency or the muon identification efficiency, can be controlled with real data efficiency measurements.

## 6.1 Efficiency study

In this section we will address the problem of the efficiency determination from Monte Carlo. As already mentioned, the advantage of measuring the cross-section ratio,  $R_\psi$ , with respect to a measure of absolute cross-section, is that the main systematic effects related to the efficiency determination, cancel out in the ratio: the experimental efficiencies will be very similar for  $J/\psi$  and  $\psi(2S)$  so that their ratio will be close to one.

Even if the knowledge of the absolute efficiency for  $J/\psi$  and  $\psi(2S)$  is not required in the measurement of the ratio, the value  $\epsilon/\epsilon'$  that we will get from Monte Carlo, has to be anyway controlled with real data. At least some basic results from Monte Carlo have to be checked. First of all, the main distributions, such as the momentum, transverse momentum and pseudo-rapidity obtained from Monte Carlo must be compared with the ones obtained from real data. Subsequently the measurements from real data of the tracking efficiency, of the muon identification efficiency and of the L0 trigger efficiency, have to be performed.

The efficiency ratio  $\epsilon/\epsilon'$  can be written as

$$\frac{\epsilon}{\epsilon'} = \frac{\epsilon^{\mu\mu} \epsilon_{r\&zs} \epsilon_{trig}}{\epsilon'^{\mu\mu} \epsilon'_{r\&zs} \epsilon'_{trig}} \quad (6.6)$$

where  $\epsilon^{\mu\mu}$  is the geometrical acceptance, namely the probability that both decay

muons from  $J/\psi$  have polar angle  $10 < \theta < 400$  mrad and  $p_z > 0$ .  $\epsilon_{r\&s}$  is the efficiency of reconstruction and offline selection, namely the fraction of events ( $J/\psi$  mesons) in the geometrical acceptance which are effectively reconstructed and offline selected.  $\epsilon_{trig}$  is the trigger efficiency, namely the fraction of selected events which successfully pass the trigger. The quantities marked with prime symbol (') refer to  $\psi(2S)$ .

### 6.1.1 Geometrical acceptance

The geometrical acceptance,  $\epsilon^{\mu\mu}$  for  $J/\psi$  and  $\epsilon'^{\mu\mu}$  for  $\psi(2S)$ , is defined as the probability to have both decay muons in a portion of solid angle defined by  $10 < \theta < 400$  mrad and  $p_z > 0$ . Such geometrical acceptance does not correspond exactly to the real detector acceptance: the LHCb cross section in the vertical plane ( $x,y$ ), has a rectangular shape inscribed in the annulus identified, at  $z$  fixed, from the relation  $10 < \theta < 400$  mrad. The geometrical acceptance can be completely determined from Monte Carlo.

Using the LHCb simulation software (Gauss), we have generated events of inclusive  $J/\psi \rightarrow \mu^+\mu^-$  and  $\psi(2S) \rightarrow \mu^+\mu^-$ . We run Gauss in generator stand-alone modality, switching off the simulation phase in which the interaction of the produced particles with the LHCb detector is, normally, simulated. The generator stand-alone modality uses Pythia+EvtGen [30], [55] to produce proton-proton collisions and to force a certain decay ( $\rightarrow \mu^+\mu^-$  in this case) when a signal particle ( $J/\psi$  or  $\psi(2S)$  in this case) is produced. In the generation of such events any acceptance cut on the produced signal particles has been removed: the  $J/\psi \rightarrow \mu^+\mu^-$  and the  $\psi(2S) \rightarrow \mu^+\mu^-$  produced have decayed in the whole solid angle. The figure 6.1 shows the pseudo-rapidity distribution of  $J/\psi$  at generator level. The generated signal particles cover the  $\eta$  range from  $\eta \simeq -10$  to  $\eta \simeq 10$ . A similar distribution is obtained for the decay muons from  $J/\psi$  at generator level (see figure 6.2). For comparison we want to recall that the LHCb acceptance corresponds to  $1.9 < \eta < 5$ .

In order to evaluate  $\epsilon^{\mu\mu}$  we made the requests that the generated  $J/\psi$  had positive  $p_z$  and both decay muons with polar angle  $10 < \theta < 400$  mrad.  $\epsilon^{\mu\mu}$  is independent on the transverse momentum and its mean value has resulted to be

$$\langle \epsilon^{\mu\mu} \rangle_{p_t} = (20.3 \pm 0.5)\%.$$

The same has been done for the  $\psi(2S) \rightarrow \mu^+\mu^-$  we have generated. The evaluated acceptance is

$$\langle \epsilon'^{\mu\mu} \rangle_{p_t} = (19.1 \pm 0.9)\%.$$

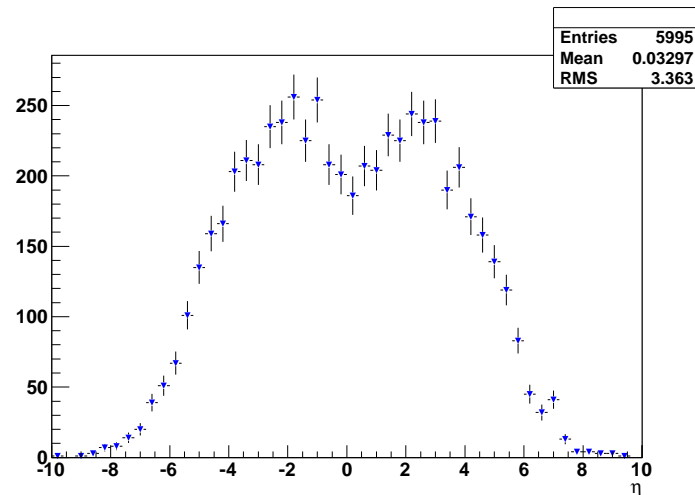


Figure 6.1: Pseudo-rapidity of  $J/\psi$  at generator level. No acceptance cuts are applied. The LHCb geometrical acceptance is  $1.9 < \eta < 5$ .

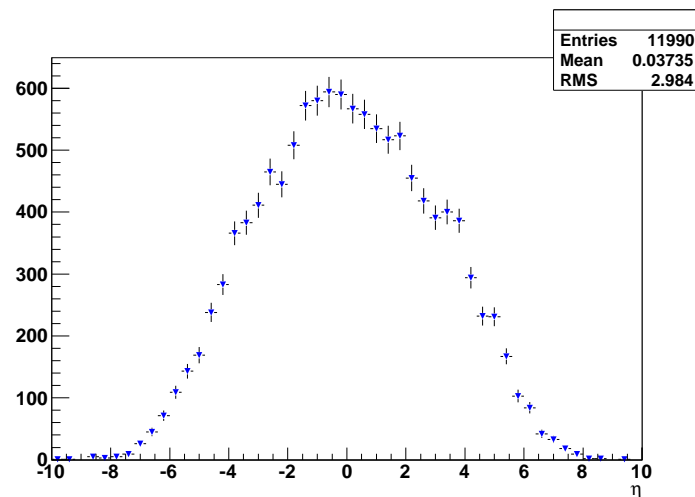


Figure 6.2: Pseudo-rapidity of muons from  $J/\psi$  at generator level. No acceptance cuts are applied. The LHCb geometrical acceptance is  $1.9 < \eta < 5$ .

The two geometrical acceptances are compatible each other within the uncertainties, whose source is the statistics used in the Monte Carlo. The ratio  $\epsilon^{\mu\mu}/\epsilon^{J\mu\mu}$ , needed to correct the  $\psi'$  to  $J/\psi$  ratio is

$$\epsilon^{\mu\mu}/\epsilon^{J\mu\mu} = 1.06 \pm 0.06.$$

The error can, of course, be reduced increasing the size of Monte Carlo samples produced.

### 6.1.2 Reconstruction and selection efficiency

The reconstruction and selection efficiency,  $\epsilon_{r\&s}$  for  $J/\psi$  and  $\epsilon'_{r\&s}$  for  $\psi(2S)$ , is defined as the number of  $\psi \rightarrow \mu^+\mu^-$  effectively reconstructed and offline selected with respect to the number of  $\psi \rightarrow \mu^+\mu^-$  in the geometrical acceptance

$$\epsilon_{r\&s} = \frac{\text{Number of } J/\psi \text{ reconstructed and selected}}{\text{Number of } J/\psi \text{ in LHCb geometrical acceptance}} . \quad (6.7)$$

$\epsilon_{r\&s}$  is the global result of a series of conditions which must be satisfied:

1. both muons in the geometrical acceptance have to be reconstructible, that is, they must really traverse the sub-detectors;
2. both muons must be tracked in the tracking system;
3. both muons must be identified as muons by the muon ID procedure;
4. a common vertex has to be reconstructed;
5. the reconstructed  $\psi$  meson has to pass the offline selection cuts.

Each of the items listed above introduces an efficiency factor and all of them contribute to form the reconstruction and offline selection efficiency  $\epsilon_{r\&s}$ .

The item 1. is related to the real detector acceptance being different from the geometrical acceptance previously defined. Such term has to be deduced from Monte Carlo. The items 2. and 3. can be deduced either from Monte Carlo or from real data, as it is possible to measure the tracking efficiency and the muon ID efficiency. Concerning the item 4., namely the efficiency of the common vertex reconstruction, hints can come from Monte Carlo. Finally, the last term of efficiency, the item 5., is deduced from Monte Carlo but hints can come from real data also, estimating the signal in the mass peak surviving the selection cuts.

In order to determine the efficiency  $\epsilon_{r\&s}$  we run the offline selection on two separate samples of inclusive  $J/\psi \rightarrow \mu^+\mu^-$  and  $\psi(2S) \rightarrow \mu^+\mu^-$  reconstructed in the detector. In figure 6.3 we show the dimuon invariant mass. In this figure, the invariant masses of the two separate samples,  $J/\psi \rightarrow \mu^+\mu^-$  and  $\psi(2S) \rightarrow \mu^+\mu^-$ , have been plotted in the same histogram, re-scaling appropriately the signals in such a way that the  $\psi(2S)(\mu^+\mu^-)$  signal was 2% of the  $J/\psi(\mu^+\mu^-)$  signal. A 2% signal ratio is a reasonable value and in agreement with the measurements performed by CDF (see figure 4.12).

The events selected in the mass window  $\pm 45 \text{ MeV}/c^2$  around  $J/\psi$  and  $\pm 45 \text{ MeV}/c^2$  around  $\psi(2S)$  have very similar kinematic properties, such as momentum, transverse momentum and pseudo-rapidity.

In figure 6.4 the transverse momentum distributions of selected  $J/\psi$  (left plot) and  $\psi(2S)$  (right plot) in the mass window  $\pm 45 \text{ MeV}/c^2$  around the respective resonance masses, are shown.

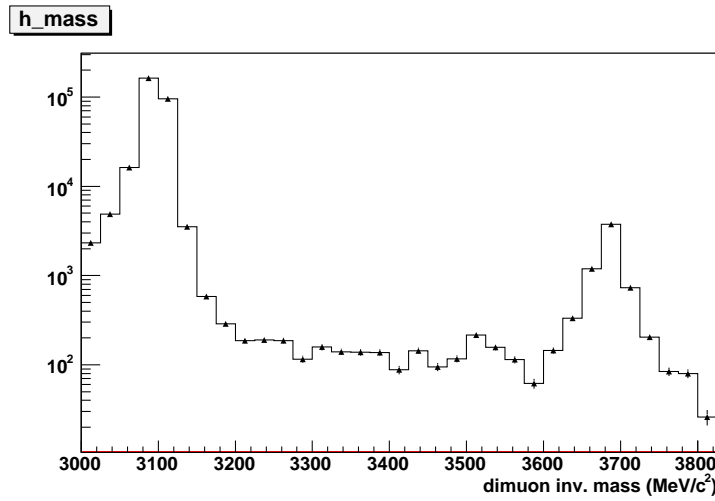


Figure 6.3: Dimuon invariant mass distribution. Two separate samples of inclusive  $J/\psi \rightarrow \mu^+\mu^-$  and  $\psi(2S) \rightarrow \mu^+\mu^-$  have been selected with the same offline selection and have been plotted on the same histogram. The signals have been scaled in such a way that the  $\psi(2S)(\mu^+\mu^-)$  signal was 2% of the  $J/\psi(\mu^+\mu^-)$  signal.

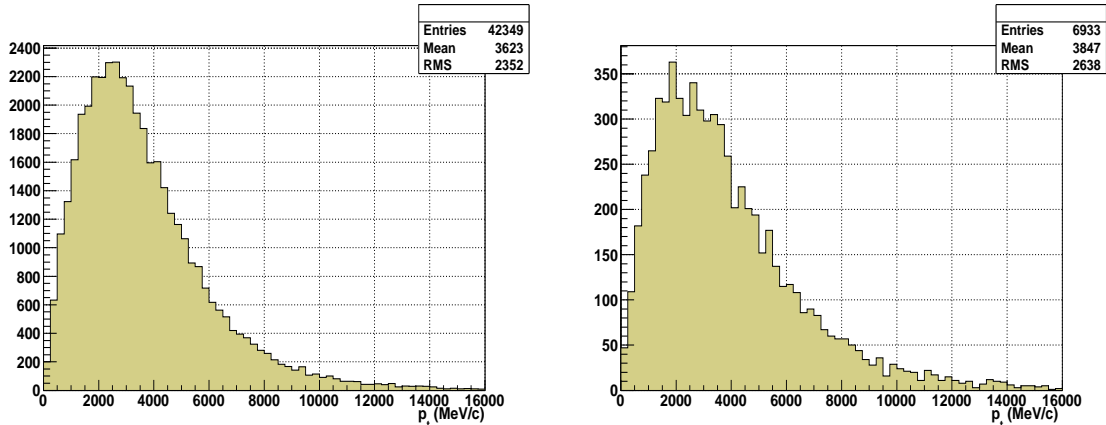


Figure 6.4: Transverse momentum distributions of selected  $J/\psi$  (left plot) and  $\psi(2S)$  (right plot), in the mass window  $\pm 45 \text{ MeV}/c^2$  around the respective resonance masses. The bin size corresponds to  $250 \text{ MeV}/c$ .

As we can see, the transverse momentum distributions have a very similar shape. Both distributions have a peak around  $2.5 \text{ GeV}/c$  and extend up to about  $16 \text{ GeV}/c$ . A minor difference can be noticed between the mean values: the mean transverse momentum for  $\psi(2S)$  is larger than the mean for  $J/\psi$  of about 6%.

In the figures 6.5 and 6.6, the momentum and the pseudo-rapidity distributions of  $J/\psi$  (left plot) and  $\psi(2S)$  (right plot) selected, are shown. While no evident differences can be noticed in the shapes for  $J/\psi$  and  $\psi(2S)$ , the average momentum of  $\psi(2S)$  results to be about 5% larger than the average momentum of  $J/\psi$ .

Despite the pseudo-rapidity range of LHCb is  $1.9 < \eta < 5$ , some few selected  $J/\psi$  and  $\psi(2S)$  have higher pseudo-rapidity, up to 7. This is normal and is due to the fact that the relationship  $1.9 < \eta < 5$  has to be satisfied by the two decay muons, which are effectively tracked in the detector. The reconstructed resonance instead can have pseudo-rapidity slightly different.

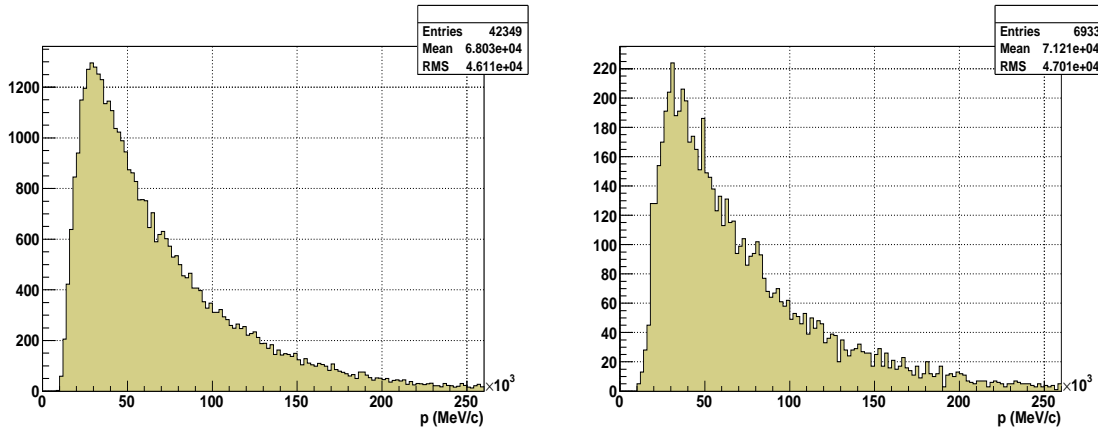


Figure 6.5: Momentum distributions of selected  $J/\psi$  (left plot) and  $\psi(2S)$  (right plot), in the mass window  $\pm 45$  MeV/ $c^2$  around the respective resonance masses. The bin size corresponds to 2000 MeV/ $c$ .

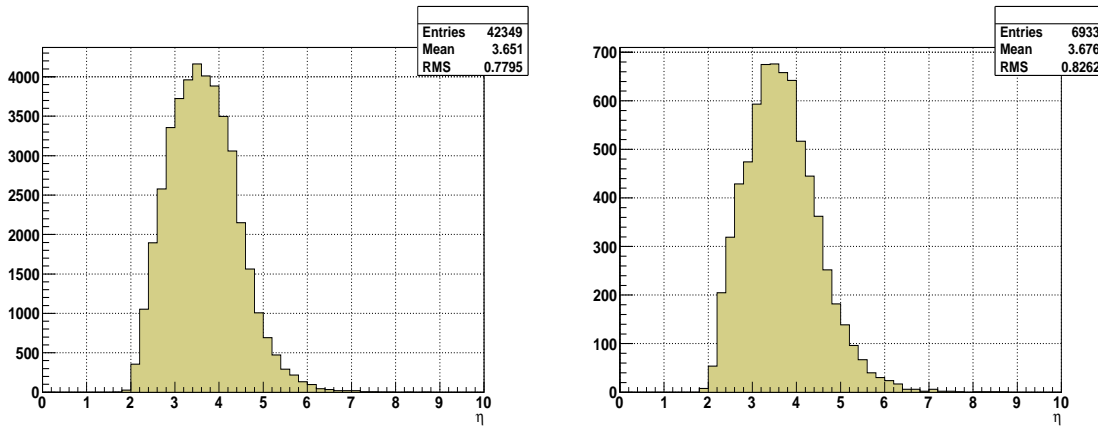


Figure 6.6: Pseudo-rapidity distributions of selected  $J/\psi$  (left plot) and  $\psi(2S)$  (right plot), in the mass window  $\pm 45$  MeV/ $c^2$  around the respective resonance masses. The bin size corresponds to 0.2.

In the figures 6.7 and 6.8, the muon momentum and the muon transverse momentum distributions of  $J/\psi$  (left plot) and  $\psi(2S)$  (right plot) selected, are shown. For  $\psi(2S)$  the muon momentum is larger of about 5% and the muon transverse momentum is larger of about 13% than  $J/\psi$ .

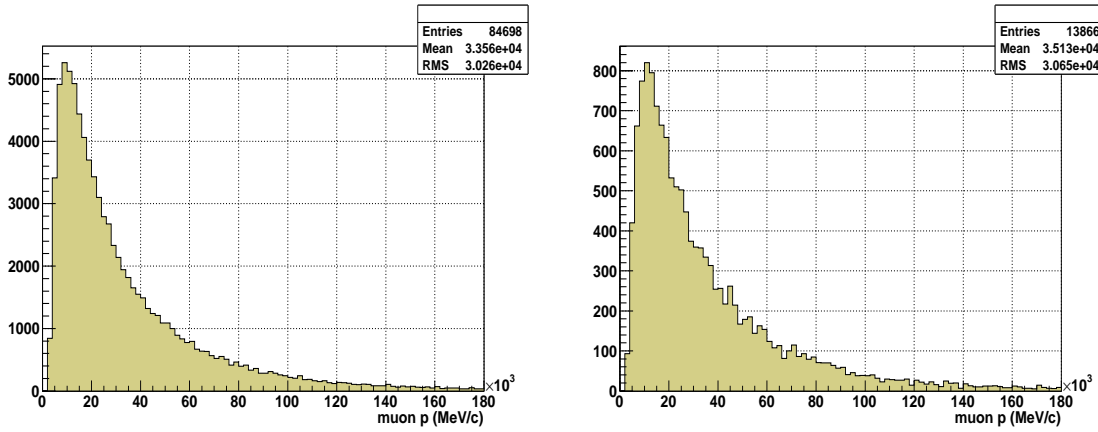


Figure 6.7: Muon momentum distributions of selected  $J/\psi$  (left plot) and  $\psi(2S)$  (right plot), in the mass window  $\pm 45 \text{ MeV}/c^2$  around the respective resonance masses. The bin size corresponds to  $2000 \text{ MeV}/c$ .

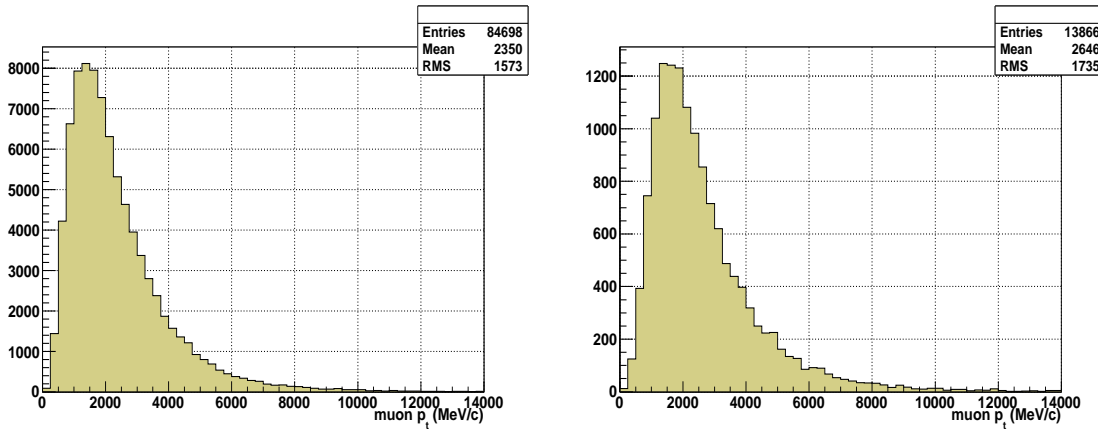


Figure 6.8: Muon transverse momentum distributions of selected  $J/\psi$  (left plot) and  $\psi(2S)$  (right plot), in the mass window  $\pm 45 \text{ MeV}/c^2$  around the respective resonance masses. The bin size corresponds to  $250 \text{ MeV}/c$ .

The main distributions for  $J/\psi$  and  $\psi(2S)$  selected with the same offline selection, highlight a lot of analogies between the two mesons and their decay muons. For this reason one would expect similar reconstruction and selection efficiencies for the two resonances. Using the Monte Carlo truth information it is possible, after the reconstruction and selection, to check whether the reconstructed and selected  $\psi$  meson matches or not with a Monte Carlo true  $\psi$  meson. Either for selected  $J/\psi$  or  $\psi(2S)$ , the Monte Carlo truth match fraction is 99%.

The reconstruction and selection efficiency, given from the ratio of equation 6.7, has been computed in  $p_t$  bins,  $\epsilon_{r\&s}(p_t)$ .

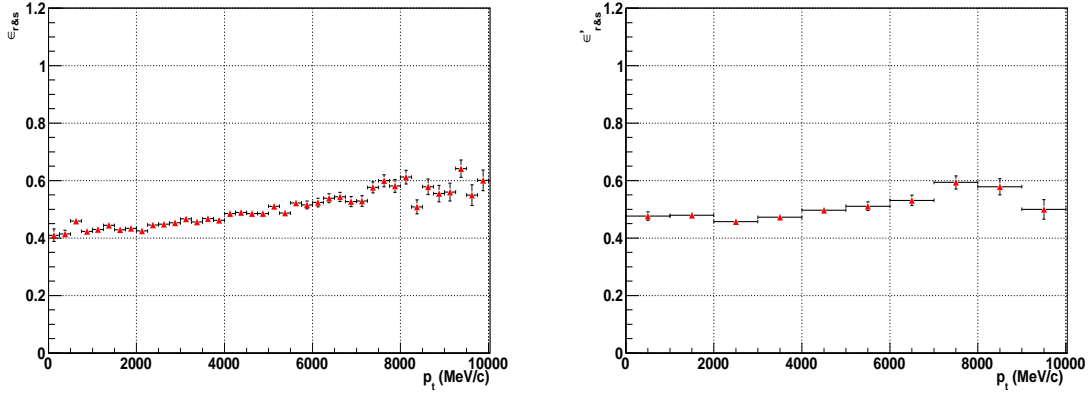


Figure 6.9: Reconstruction and selection efficiency of  $J/\psi$  (left plot) and  $\psi(2S)$  (right plot), as a function of the meson transverse momentum. For  $J/\psi$  one bin corresponds to 250 MeV/c, while for  $\psi(2S)$  one bin corresponds to 1 GeV/c.

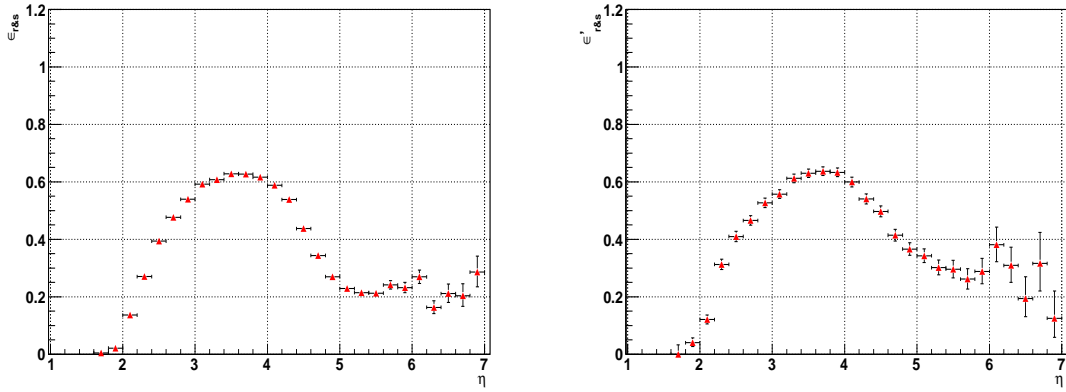


Figure 6.10: Reconstruction and selection efficiency of  $J/\psi$  (left plot) and  $\psi(2S)$  (right plot), as a function of the meson pseudo-rapidity. Each bin corresponds to 0.2.

The figure 6.9 shows the reconstruction and selection efficiency of  $J/\psi$  (left plot) and  $\psi(2S)$  (right plot), as a function of the meson transverse momentum. The efficiencies have been computed in each  $p_t$  bin, that is, 250 MeV/c for  $J/\psi$  and 1 GeV/c for  $\psi(2S)$ . The efficiency shows an increase at large  $p_t$ : the reconstruction capabilities improve at large  $p_t$  because the more the particle energy is large, the better are the detector performance.

The reconstruction and selection efficiencies have also been computed in pseudo-rapidity bins (see figure 6.10). The shape of the efficiency, in this case, depends on the geometry of the detector. In the boundary regions,  $\eta \sim 2$  and  $\eta \sim 5$ , the efficiency gets down due to the detector acceptance.

Table 6.1: Reconstruction and selection efficiencies,  $\epsilon_{r\&s}$  and  $\epsilon'_{r\&s}$ , computed in  $p_t$  bins.

$p_t$ range (GeV/c)	$\epsilon_{r\&s}$	$\epsilon'_{r\&s}$	$\epsilon_{r\&s}/\epsilon'_{r\&s}$
0-1	$0.432\pm 0.006$	$0.476\pm 0.014$	$0.91\pm 0.03$
1-2	$0.434\pm 0.004$	$0.479\pm 0.010$	$0.91\pm 0.02$
2-3	$0.443\pm 0.004$	$0.457\pm 0.009$	$0.97\pm 0.02$
3-4	$0.463\pm 0.004$	$0.472\pm 0.010$	$0.98\pm 0.02$
4-5	$0.486\pm 0.005$	$0.497\pm 0.012$	$0.98\pm 0.03$
5-6	$0.508\pm 0.006$	$0.511\pm 0.015$	$0.99\pm 0.03$
6-7	$0.533\pm 0.008$	$0.531\pm 0.018$	$1.00\pm 0.04$
7-8	$0.568\pm 0.010$	$0.594\pm 0.023$	$0.96\pm 0.04$
8-9	$0.563\pm 0.013$	$0.579\pm 0.028$	$0.97\pm 0.05$
9-10	$0.590\pm 0.017$	$0.500\pm 0.034$	$1.18\pm 0.09$

In table 6.1 the reconstruction and selection efficiencies for  $J/\psi$  and  $\psi(2S)$ , as well as their ratio, are given in each  $p_t$  bin. According to the statistics available one can consider to use the value  $\epsilon_{r\&s}/\epsilon'_{r\&s}$  to correct the  $\psi(2S)$  to  $J/\psi$  ratio in each  $p_t$  bin (and possibly in each  $\eta$  bin), or to use the average value on the full  $p_t$  spectrum

$$\langle \epsilon_{r\&s}/\epsilon'_{r\&s} \rangle_{p_t} = 0.99 \pm 0.01$$

### 6.1.3 Trigger efficiency

The trigger introduces a further factor in the  $\psi(2S)$  to  $J/\psi$  ratio:  $\epsilon_{trig}/\epsilon'_{trig}$ . The trigger efficiency can be factorized as  $\epsilon_{trig} = \epsilon_{L0} \times \epsilon_{HLT1} \times \epsilon_{HLT2}$ , since the trigger is composed of three levels as described in chapter 3.

In the first periods of data taking, the running conditions will be not the nominal ones. Several scenarios are foreseen in which the number of bunches, the luminosity and the beam energy are well below than the nominal values. Of course if the conditions are not the nominal ones, lower event rates are expected. Different running scenarios can be dealt with using of the same L0 and HLT1 settings with HLT2 tuned to provide different rejection factors on HLT1 output. The general idea is to have minimal rejection with L0 and HLT1, using lower thresholds than nominal running conditions, and to provide, through HLT2, global rate reduction factors. For the HLT2 muon trigger, therefore, several selections have been set up with different cuts in order to provide several rate reduction factors.

A possible initial scenario for the LHC 2009/2010 run, foresees 68 colliding bunches with event pile-up  $\nu = 1$ , luminosity of  $0.8 \times 10^{31} \text{ cm}^{-2} \text{ s}^{-1}$  and energy 3.5 TeV/beam (the energy will be increased up to 5 TeV/beam at the end of 2009/2010 run). In these running conditions the expected event rates are

Table 6.2: The trigger efficiencies for  $J/\psi$  and  $\psi(2S)$ . The efficiencies have been determined running the L0 trigger, the HLT1 trigger and the HLT2 muon selections on samples of offline selected inclusive  $J/\psi \rightarrow \mu^+\mu^-$  and  $\psi(2S) \rightarrow \mu^+\mu^-$  events. The case (i) is the most favorable case in which  $\sim 1$  kHz of the HLT2 output is devoted to muon triggers, while the case (ii) is the one less favorable, in which only  $\sim 0.1$  kHz are devoted to muon triggers.

Trigger level	$\epsilon'_{trig}$	$\epsilon_{trig}$	$\epsilon_{trig}/\epsilon'_{trig}$
L0	$0.999 \pm 0.001$	$0.992 \pm 0.003$	$0.993 \pm 0.003$
L0 $\times$ HLT1	$0.954 \pm 0.007$	$0.899 \pm 0.010$	$0.94 \pm 0.01$
L0 $\times$ HLT1 $\times$ HLT2 (i)	$0.944 \pm 0.007$	$0.867 \pm 0.011$	$0.92 \pm 0.01$
L0 $\times$ HLT1 $\times$ HLT2 (ii)	$0.915 \pm 0.009$	$0.851 \pm 0.011$	$0.93 \pm 0.02$

320 kHz visible rate  $\rightarrow$  300 kHz L0 output rate  $\rightarrow$  10 kHz HLT1 output rate

of which 3 kHz are HLT1 Muon triggers.

Since the maximum rate to which the events can be written to storage is 2 kHz, the HLT2 selections have to provide further reduction factors. The HLT2 muon selections can introduce rate reduction factors up to 100, reducing the 10 kHz HLT1 output rate to 0.1 kHz. The muon trigger bandwidth depends on the running conditions and on the physics priorities. Of course the HLT2 efficiency, hence the total trigger efficiency, will depend on the rate reduction factor imposed: the more the reduction factor required is large, the more the trigger efficiency is small.

In the table 6.2 the trigger efficiencies are shown for  $J/\psi \rightarrow \mu^+\mu^-$  and  $\psi(2S) \rightarrow \mu^+\mu^-$ . The results refer to the first running conditions trigger settings. Samples of selected events of the type “MC09” (5+5 TeV energy,  $\nu = 1$ ) have been used to determine the trigger efficiencies. The case (i) is the most favorable case, in which the rate reduction factor is minimum and  $\sim 1$  kHz of muon trigger events are written to storage (maximum muon bandwidth). The case (ii) is the less favorable case, in which the rate reduction factor is maximum and  $\sim 0.1$  kHz of muon trigger events are written to storage (minimum muon bandwidth). In both cases the trigger efficiency ratios are in good agreement each other:  $0.92 \pm 0.01$  and  $0.93 \pm 0.02$ .

### Muon trigger: hints to check the Monte Carlo

As already outlined previously, the Monte Carlo tuning is a fundamental step for each analysis and even a first data measurement, as the one described in this thesis, which does not require the knowledge of the absolute efficiencies, cannot ignore this phase. The process of tuning of Monte Carlo by real data, allows to increase the reliability of the simulation data and, hence, the reliability of the efficiencies computed by Monte Carlo.

Since the L0 trigger comprises several L0-channels, hadron, electron,  $\gamma$ ,  $\pi^0$  and muon, an event  $J/\psi \rightarrow \mu^+\mu^-$  can, in principle, be triggered from a non-muon trigger:  $J/\psi \rightarrow \mu^+\mu^-$  can accidentally be found in hadron trigger events. Such events can be used to do muon trigger-unbiased distributions, such as  $p_t$  distribution. The same distributions can be done for  $J/\psi \rightarrow \mu^+\mu^-$  events triggered from the muon trigger, in order to evaluate the effect of the muon trigger. This comparison can be done both between the Monte Carlo simulated distributions and between real data distributions, therefore the muon trigger effect on  $J/\psi \rightarrow \mu^+\mu^-$  can be checked with the real data.

#### 6.1.4 Global efficiency ratio

The efficiencies and the acceptances determined from Monte Carlo, can be put together to give the global efficiency ratio of equation 6.6 (see table 6.3).

Table 6.3: Partial and global efficiency ratios.

$\frac{\epsilon^{\mu\mu}}{\epsilon'^{\mu\mu}} = 1.06 \pm 0.06$	$\frac{\epsilon_{r\&s}}{\epsilon'_{r\&s}} = 0.99 \pm 0.01$	$\frac{\epsilon_{trig}}{\epsilon'_{trig}} = 0.93 \pm 0.02$	$\frac{\epsilon}{\epsilon'} = 0.98 \pm 0.06$
--	--	--	--

Despite the geometrical acceptance ratio  $\epsilon^{\mu\mu}/\epsilon'^{\mu\mu}$  is compatible with one, its best value, 1.06, seems to indicate that the acceptance for muons from  $J/\psi$  is slightly larger than for muons from  $\psi(2S)$ . This could be due to the fact that for  $\psi(2S)$  the two decay muons form a relative angle larger than the  $J/\psi$  muons angle, because of the larger mass of  $\psi(2S)$ , therefore the probability for the two muons to get out the LHCb acceptance, increases.

The trigger efficiency for  $\psi(2S)$  results to be larger than the trigger efficiency for  $J/\psi$ , the ratio being equal to 0.93. This is due, mainly, to the HLT selection cut on the muon transverse momentum, which is fixed at  $p_t^\mu > 1$  GeV/c. This cut rejects more  $J/\psi$  signal than  $\psi(2S)$  signal.

The global efficiency ratio,  $\epsilon/\epsilon' = 0.98 \pm 0.06$ , is used to correct the raw  $\psi'$  to  $J/\psi$  ratio. As expected such ratio is close to one, which means that the global experimental effect due to the reconstruction in LHCb of  $J/\psi$  is analogue to the

effect introduced for  $\psi(2S)$ .

The error 0.06 is only due to the Monte Carlo sample size used in the simulation, and can be easily reduced to negligible values increasing the samples size.

## 6.2 Systematic errors

After the LHC start, due to the abundance of charmonium in the collisions, the statistical error on the number of  $\psi$  mesons selected will be reduced soon to negligible values (under 10% with only  $5 \text{ pb}^{-1}$  of data collected). On the other hand several systematic sources have to be taken into account in order to evaluate correctly the uncertainties on the measurement.

Given the kinematic analogies between  $J/\psi$  and  $\psi'$  ( $p$  and  $p_t$  spectra) and the relatively small mass difference ( $\sim 590 \text{ MeV}/c^2$ ) between them, we may reasonably assume that in the efficiency ratio,  $\epsilon/\epsilon'$ , the main systematic effects due to the modeling in the Monte Carlo, cancel out. Nevertheless some systematic bias can appear due to uncertainties in the simulation of kinematical distributions of charmonia. Possible biases have to be evaluated by varying, and tuning with real data, the parameters of the Monte Carlo simulation.

A source of non-statistical error is the one that arise from the dimuon branching fractions ratio

$$B_{\mu\mu}/B'_{\mu\mu} = 7.80 \pm 0.83 \quad (6.8)$$

(see table 4.2). This error is unavoidable and is due, mainly, to the uncertainty on the  $\psi'$  dimuon branching fraction which is known with a relative error of 10.5%, and in minor part to the  $J/\psi$  dimuon branching fraction which is known with a relative error of 1.0%.

Another source of systematic error is the one that arise from assuming unpolarized mesons. As we will see, due to the limited angular acceptance of the LHCb detector, the efficiency  $\epsilon$  ( $\epsilon'$ ) depends on the polarization state of  $J/\psi$  ( $\psi'$ ) and, therefore, the  $\epsilon/\epsilon'$  ratio could be affected by a difference between the polarizations of the two mesons. The CDF measurements (see figure 4.19) in the helicity frame, seem to suggest that the difference in the  $J/\psi$  and  $\psi'$  polarization is small, with a trend for both mesons to a longitudinal polarization as  $p_t$  grows up.

Given the character of “first measurement” of the  $\psi'$  to  $J/\psi$  production ratio described in this thesis, in the first periods of data taking we will not know the polarization state of  $J/\psi$  and  $\psi'$  at LHC. Thus we should dispense with this information and assume unpolarized mesons. In the following we will try to estimate the systematic uncertainty introduced by such an assumption.

### 6.2.1 Systematic error from polarization

In chapter 4 we have seen the distribution function of decay muons, equation 4.12, that we report here for convenience

$$I(\cos \theta^*) = \frac{3}{2(\alpha + 3)}(1 + \alpha \cos^2 \theta^*)$$

where  $\theta^*$  is the angle between  $\mu^+$  in the  $\psi$  meson rest frame and the  $\psi$  direction in the laboratory frame.  $\alpha$  can vary in the range  $-1 \leq \alpha \leq 1$ , where  $\alpha = -1$  for totally longitudinal polarized mesons and  $\alpha = +1$  for totally transverse polarized mesons. In case of unpolarized mesons,  $\alpha = 0$  (see figure 6.11).

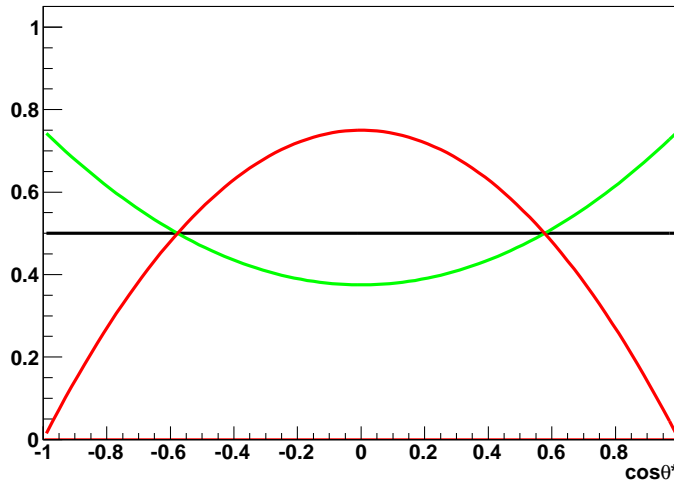


Figure 6.11:  $\cos \theta^*$  probability density functions for: (black line) unpolarized mesons,  $\alpha = 0$ ; (red line) totally longitudinal polarized mesons,  $\alpha = -1$ ; (green line) totally transverse polarized mesons,  $\alpha = +1$ . The distributions are all normalized to one.

In order to determine the  $\cos \theta^*$  variable from reconstructed particles, a Lorentz boost has to be applied in order to pass from the laboratory frame to the meson rest frame. Since in the LHCb Monte Carlo, unpolarized  $\psi$  have been generated, the  $\cos \theta^*$  distribution at the generator level, is flat. This feature is, nevertheless, lost when the  $\cos \theta^*$  distribution is reconstructed: the request of having both decay muons in the LHCb acceptance as well as the reconstruction procedure itself, modify the shape of the distribution mimicking a non-zero polarization (see figure 6.12).

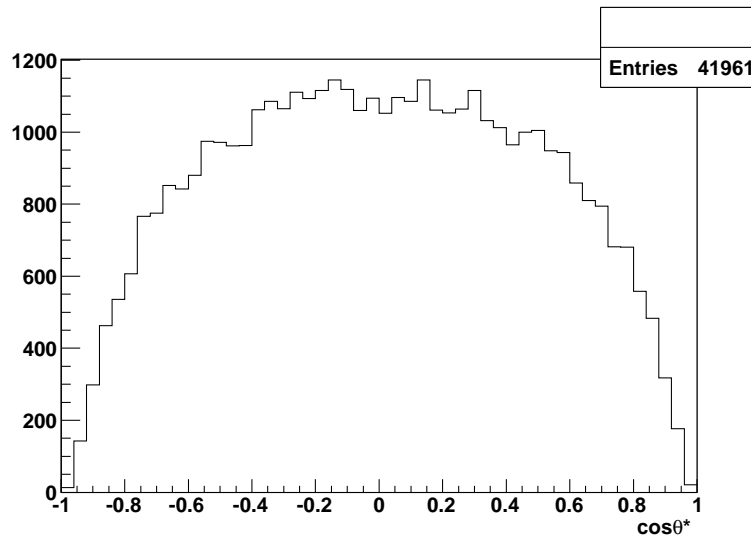


Figure 6.12:  $\cos \theta^*$  distribution for reconstructed and offline selected  $J/\psi$  (Monte Carlo matching with a true  $J/\psi$ ). In spite of the mesons are unpolarized, the distribution is not flat.

The LHCb detector reconstructs and selects events over the  $\cos \theta^*$  range with non-uniform efficiency. The efficiency is maximum in the central region of  $\cos \theta^*$  and is minimum close to the boundary regions. The reason for which LHCb is less efficient close to the boundaries is related to the kinematics of the two decay muons: when  $|\cos \theta^*| \simeq 1$  one of the two decay muons takes away most of the  $J/\psi$  energy, leaving a small energy to the other muon. The figure 6.13 shows (left plot) the  $\min(p^{\mu^+}, p^{\mu^-})$  versus the  $\cos \theta^*$  variable at the generator level. The right plot shows the same dependency but for reconstructed and selected  $J/\psi$ . It is evident the decrease of muons energy close to the boundary regions.

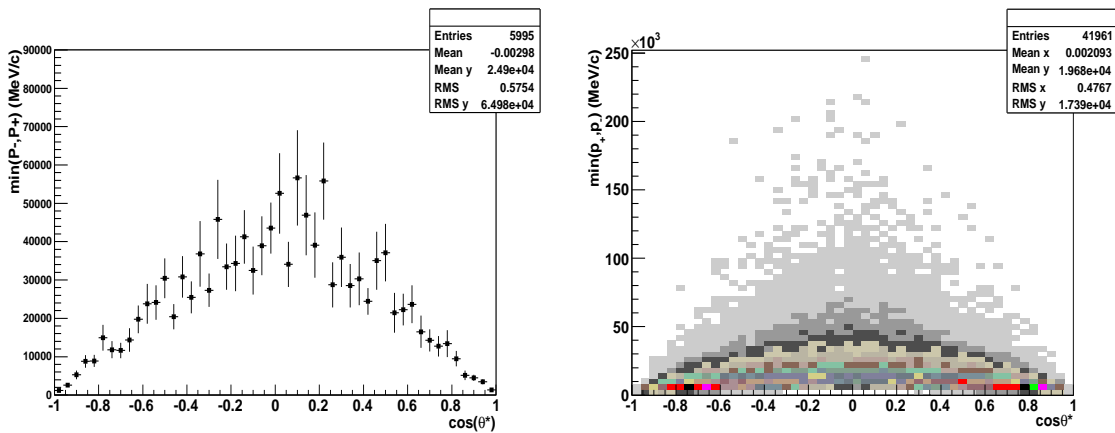


Figure 6.13: Minimum momentum of  $\mu^+$  and  $\mu^-$  versus the  $\cos \theta^*$  variable for generator level  $J/\psi$  (profile histogram, left) and for reconstructed and selected  $J/\psi$  (scatter histogram, right).

The dependence of the efficiency on  $\cos \theta^*$ ,  $\epsilon(\cos \theta^*)$ , is shown in figure 6.14. The efficiency computed here accounts for the geometrical acceptance, the reconstruction and selection, and the L0 trigger. The function used to fit data is a fourth order polynomial,  $p_0 + p_1x^4$ .

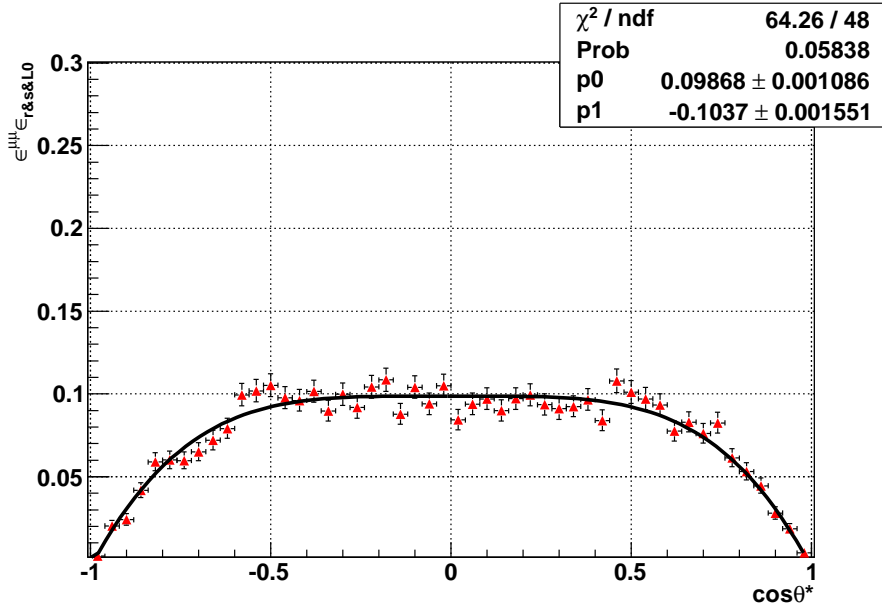


Figure 6.14: The experimental efficiency, up to L0 trigger, dependence on  $\cos \theta^*$ , for unpolarized  $\psi \rightarrow \mu^+ \mu^-$ : the function fitted to Monte Carlo data is  $p_0 + p_1x^4$ .

As the efficiency is not flat over the  $\cos \theta^*$  range, we expect that if the distribution of  $\cos \theta^*$  changes at the generator level, because the mesons are polarized, the number of reconstructed  $\psi$  mesons changes too: this can be exploited to assess how the average efficiency varies when  $\alpha$  changes from -1 to +1.

Let us consider a sample of  $\psi$  mesons ( $J/\psi$  or  $\psi(2S)$ ) generated with a flat  $\cos \theta^*$  distribution, namely unpolarized  $\psi$  mesons (see figure 6.15 left plot). The requirement to be in acceptance, the reconstruction procedure, the selection and the trigger, modify the distribution shape (figure 6.15 right plot). In this case, of unpolarized mesons, the average efficiency results to be

$$\langle \epsilon^{\alpha=0} \rangle_{\cos \theta^*} = (7.8 \pm 0.1)\%.$$

In order to simulate polarized  $\psi$  mesons, we have weighted the events, uniformly distributed of figure 6.15 (left plot), with the function of equation 4.12 in which  $\alpha$  was set at 1 and then at -1. In figure 6.16 the results of this simulation are shown.

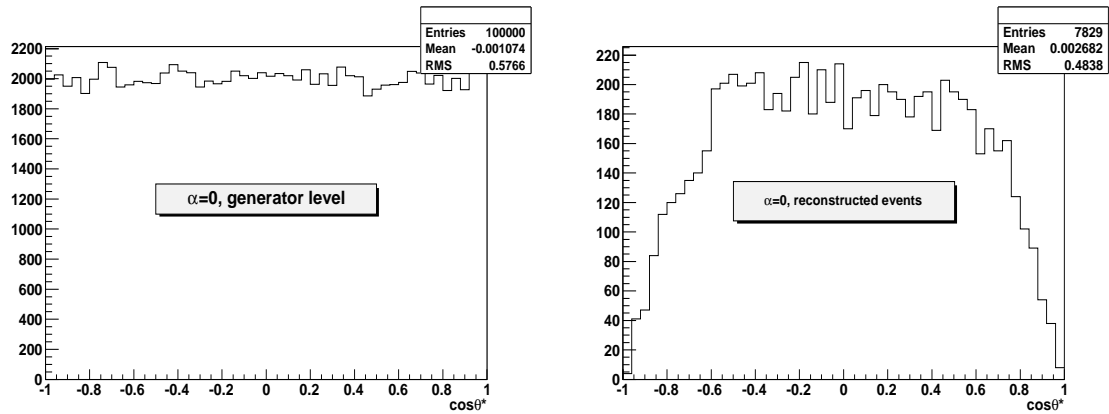


Figure 6.15: (Left plot)  $\cos\theta^*$  distribution for  $\psi$  mesons at the generator level. The flat distribution is due to  $\psi$  which are unpolarized. (Right plot)  $\cos\theta^*$  distribution for  $\psi$  mesons which have been reconstructed, selected and triggered from the LO.

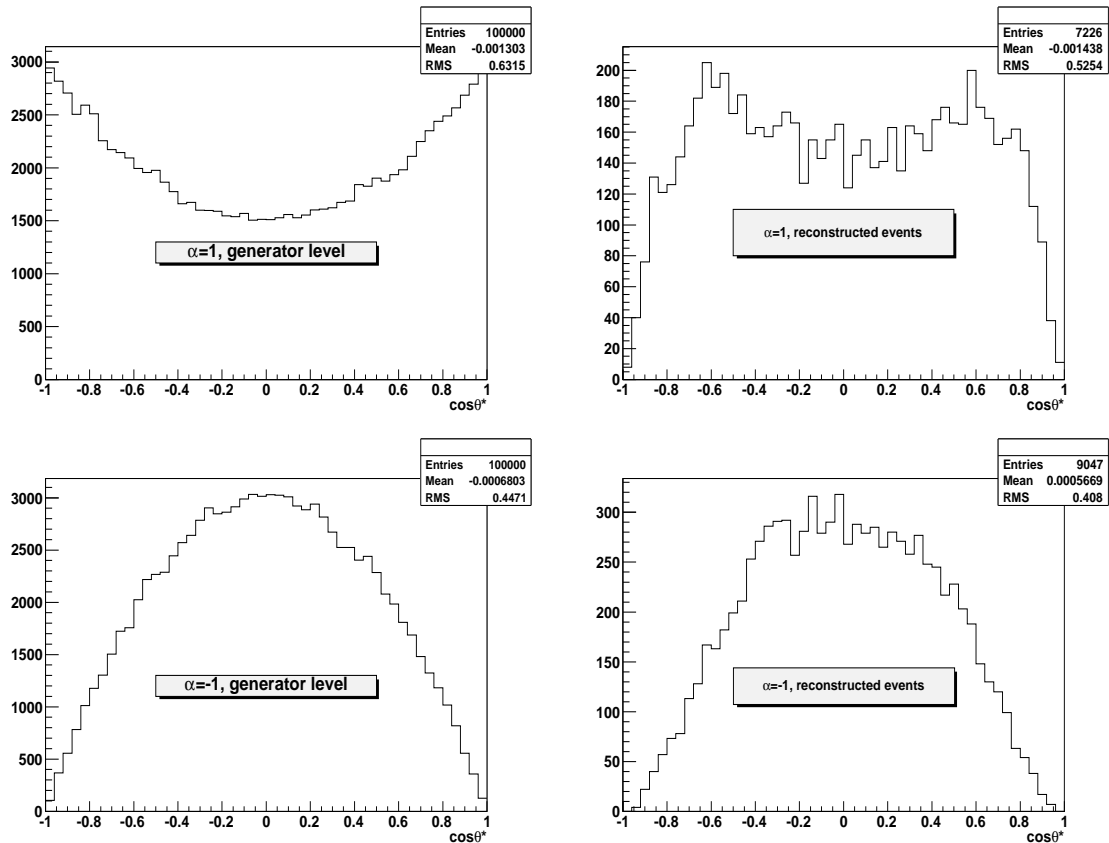


Figure 6.16:  $\cos\theta^*$  distribution for  $\psi$  mesons (top) totally transverse polarized,  $\alpha = 1$ , at the generator level (left) and after the reconstruction (right).  $\cos\theta^*$  distribution for  $\psi$  mesons (bottom) totally longitudinal polarized,  $\alpha = -1$ , at the generator level (left) and after the reconstruction (right).

When  $\alpha$  is assumed to be equal to 1, (fig. 6.16, top) less events, in the whole  $\cos \theta^*$  spectrum, are reconstructed and selected than the case  $\alpha = 0$ . The average efficiency reduces to

$$\langle \epsilon^{\alpha=1} \rangle_{\cos \theta^*} = (7.2 \pm 0.1)\%.$$

When  $\alpha$  is assumed to be equal to -1, (fig. 6.16, bottom) more events, in the whole  $\cos \theta^*$  spectrum, are reconstructed and selected than the case  $\alpha = 0$ . The average efficiency increases to

$$\langle \epsilon^{\alpha=-1} \rangle_{\cos \theta^*} = (9.0 \pm 0.1)\%.$$

Table 6.4: The efficiency (computed up to the L0) in the scenarios: ( $\alpha = 1$ ) totally transverse polarized mesons; ( $\alpha = -1$ ) totally longitudinal polarized mesons; ( $\alpha = 0$ ) unpolarized mesons. If we assume  $\alpha = 0$  (unpolarized mesons), the real efficiency, which depends on the real polarization, could vary in a range whose width is 23% of the assumed value.

Polarization	Efficiency	Systematic error assuming $\alpha = 0$
$\alpha = 1$	$(7.2 \pm 0.1)\%$	+0.6%
$\alpha = 0$	$(7.8 \pm 0.1)\%$	0.0%
$\alpha = -1$	$(9.0 \pm 0.1)\%$	-1.2%

Such systematic uncertainty, which holds both for  $J/\psi$  and  $\psi(2S)$ , propagates on the efficiency ratio, giving the following errors

$$\frac{\epsilon}{\epsilon'} = 0.98^{+0.22}_{-0.11}.$$

The error can be reduced, measuring directly the polarization at LHCb. The main problem is to understand the effect introduced from the apparatus. An idea is to compare the  $\cos \theta^*$  distribution obtained from  $\psi$  mesons with the  $\cos \theta^*$  distribution obtained from unpolarized samples. This would allow to disentangle the detector effects from the effects due to the polarization. An unpolarized “sample” could be represented by sideband events around the  $J/\psi$  mass: such combinatorial background dimuon pairs have no physical meaning and there’s not reason to be polarized. The polarization measurement is not one of the first measurements that can be done, as it requires sufficiently statistics to construct reliable distributions and requires a good knowledge of the systematic effects introduced from the apparatus. Sensitivity studies on polarization measurements and on the necessary integrated luminosity at LHCb are still in progress.

### 6.3 Correction factor to the $\psi'$ to $J/\psi$ ratio

We are now able to give an estimation of the correction factor to the  $\psi'$  to  $J/\psi$  ratio (see equation 6.5). Concerning the branching fraction ratio

$$\frac{B_{\mu\mu}}{B'_{\mu\mu}} = 7.80 \pm 0.83, \quad (6.9)$$

the error represents a systematic uncertainty on our measurement. The efficiency ratio is given from

$$\frac{\epsilon}{\epsilon'} = 0.98 \pm 0.06^{+0.22}_{-0.11} \quad (6.10)$$

where the first error refers to the statistical error due to the Monte Carlo sample size used to estimate the ratio, while the second (asymmetric) error refers to the systematic error coming from assuming unpolarized mesons. Given the different origin of the errors we will keep them separated. The statistical error ( $\pm 0.06$ ) can be reduced to negligible values increasing the Monte Carlo samples size.

The correction factor to the  $\psi'$  to  $J/\psi$  ratio is therefore

$$\frac{B_{\mu\mu}}{B'_{\mu\mu}} \frac{\epsilon}{\epsilon'} = 7.64 \pm 0.47 \pm 0.81^{+1.72}_{-0.86}. \quad (6.11)$$

While the statistical error ( $\pm 0.47$ ) can be easily reduced, the systematic due to the branching fractions ( $\pm 0.81$ ) gives a relative error of about 11% and the systematic due to the polarization gives up to 22% of relative error.

The result presented, reflects a situation rather pessimistic in which the polarizations of  $J/\psi$  and  $\psi(2S)$  can vary, independently each other, with a uniform probability in the range  $[-1,1]$ . We know, from CDF findings, that the polarization of  $J/\psi$  is similar to the polarization of  $\psi(2S)$  and that the values of  $\alpha$  vary in the range  $[-0.3,0]$  for  $J/\psi$  and  $[-0.6,0.55]$  for  $\psi(2S)$ . As a consequence if we assume such ranges at LHC also, the asymmetric systematic error on the efficiency ratio would be reduced to

$$\frac{\epsilon}{\epsilon'} = 0.98 \pm 0.06^{+0.09}_{-0.04}.$$

In this case the correction factor to the  $\psi'$  to  $J/\psi$  ratio would be

$$\frac{B_{\mu\mu}}{B'_{\mu\mu}} \frac{\epsilon}{\epsilon'} = 7.64 \pm 0.47 \pm 0.81^{+0.70}_{-0.31}, \quad (6.12)$$

thus the systematic error due to the branching fraction ratio and the systematic error due to the polarization would be of the same order of magnitude:  $\mathcal{O}(10\%)$ . Since, as we already said, the systematic error introduced from the branching fraction ratio is mainly due to the uncertainty on the  $\psi'$  dimuon branching fraction, a way to reduce this error would be to measure  $B'_{\mu\mu}$ , in order to improve the current precision on its value (see table 4.2).



# Chapter 7

## Future prospects

---

As we have seen, in the measurement of the  $\psi'$  to  $J/\psi$  production ratio, the main contribution to the uncertainty comes from the systematic error. Two sources of systematic error have been identified: the systematic coming from the dimuon branching fraction ratio and the systematic coming from assuming unpolarized mesons.

The systematic error arising from the branching fraction ratio,

$$\frac{B_{\mu\mu}}{B'_{\mu\mu}} = 7.80 \pm 0.83$$

is mainly due to the error on the  $\psi'$  dimuon branching fraction  $B'_{\mu\mu}$ , and only in minor part to the error on the  $J/\psi$  dimuon branching fraction  $B_{\mu\mu}$  (see tab 4.2). A way to reduce this error is to measure the  $\psi'$  dimuon branching fraction, currently known within 10%, in order to reduce its uncertainty to values of the same order of magnitude than the error on the  $J/\psi$  dimuon branching fraction, namely about 1%.

In this last part of the thesis we propose a way to measure  $B'_{\mu\mu}$  at LHCb through the decays of charmonium  $\psi' \rightarrow J/\psi\pi^+\pi^-$ ,  $\psi' \rightarrow \mu^+\mu^-$  and  $J/\psi \rightarrow \mu^+\mu^-$ .

Let us consider the decay  $\psi' \rightarrow J/\psi\pi^+\pi^-$  whose branching fraction,  $B'_{J/\psi\pi\pi}$ , is given in table 4.2. Reconstructing such decays, with  $J/\psi$  in the dimuon channel, and the decays  $\psi' \rightarrow \mu^+\mu^-$ , one can measure the ratio

$$\frac{\sigma_{\psi(2S)} B'_{J/\psi\pi\pi} B_{\mu\mu} \epsilon_{\mu\mu} \epsilon'_{\pi\pi}}{\sigma_{\psi(2S)} B'_{\mu\mu} \epsilon'_{\mu\mu}} = \frac{B'_{J/\psi\pi\pi} B_{\mu\mu}}{B'_{\mu\mu}} \left( \frac{\epsilon_{\mu\mu}}{\epsilon'_{\mu\mu}} \right) \epsilon'_{\pi\pi}. \quad (7.1)$$

Since  $B'_{J/\psi\pi\pi} \cdot B_{\mu\mu}$  is known with a good precision (within 2%) and  $\epsilon_{\mu\mu}/\epsilon'_{\mu\mu}$  is close to one (unless of polarization effects, as we have showed in the previous chapter), if we knew the dipion efficiency  $\epsilon'_{\pi\pi}$  with a good precision, would be possible to

extract  $B'_{\mu\mu}$  from a measure of the equation 7.1.

The main challenge in this measurement is to be able to take under control the dipion efficiency, whose absolute value enters directly in the measurement. The dipion efficiency can be determined from Monte Carlo simulation but a comparison with real data is anyhow necessary. The decay channel  $\psi' \rightarrow J/\psi \pi^+ \pi^-$  provides, also, an alternative way to measure the ratio  $R_\psi$ , as the following equation shows

$$\frac{\sigma_{\psi(2S)} B'_{J/\psi \pi \pi} B_{\mu\mu} \epsilon_{\mu\mu} \epsilon'_{\pi\pi}}{\sigma_{J/\psi} B_{\mu\mu} \epsilon_{\mu\mu}} = R_\psi B'_{J/\psi \pi \pi} \epsilon'_{\pi\pi}, \quad (7.2)$$

provided  $\epsilon'_{\pi\pi}$  was known. But the usefulness of equation 7.2 is twofold: the ratio  $R_\psi$  is measurable in the dimuon decay modes ( $J/\psi \rightarrow \mu^+ \mu^-$  and  $\psi(2S) \rightarrow \mu^+ \mu^-$ , as described in this thesis), so that if in the next future we will be able to reduce the systematic errors on  $R_\psi$ , the equation 7.2 can help us to evaluate the dipion efficiency,  $\epsilon'_{\pi\pi}$ .

In the following we will describe a selection that we have set up for the decay  $\psi' \rightarrow J/\psi \pi^+ \pi^-$  with  $J/\psi$  in the dimuon channel. The cuts have been optimized using the ‘‘MC09’’ Monte Carlo production of LHCb.

## 7.1 $\psi' \rightarrow J/\psi(\mu^+ \mu^-) \pi^+ \pi^-$ selection

The Monte Carlo events used to set up the selection are inclusive  $J/\psi \rightarrow \mu^+ \mu^-$  with both muons in the LHCb geometrical acceptance. Most of such  $J/\psi$  are directly produced in proton-proton collisions (prompt-direct component) while a fraction of them comes from  $\psi' \rightarrow J/\psi(\mu^+ \mu^-) \pi^+ \pi^-$  decays: in our Monte Carlo we find  $\sim 9$   $\psi' \rightarrow J/\psi(\mu^+ \mu^-) \pi^+ \pi^-$  out of 1000  $J/\psi \rightarrow \mu^+ \mu^-$ .

In order to understand on which variables to cut and the appropriate values of the cuts, we have, first of all, defined a quite loose selection. This loose selection comprises two main stages: 1)  $J/\psi(\mu^+ \mu^-)$  making, followed by 2) a combination of such dimuon pairs with dipion pairs.

1) To form  $J/\psi(\mu^+ \mu^-)$  we start from a set of tracks identified as muons and apply the following cuts:

- combined  $DLL_{\mu\pi} > -3$
- muon transverse momentum product  $p_T^{\mu^+} p_T^{\mu^-} > 10^6$  (MeV/c)<sup>2</sup>
- fitted common vertex  $\chi^2/\text{ndf} < 10$
- $|M_{\mu\mu} - M_{J/\psi}^{PDG}| < 200$  MeV/c<sup>2</sup>.

The cuts for  $J/\psi(\mu^+ \mu^-)$  selection have been widely discussed in the chapter 5.

2) The  $J/\psi(\mu^+ \mu^-)$  are, then, combined with pairs of tracks identified as pions. The following cuts are applied:

- combined  $DLL_{\pi K} > -5$  on both pion tracks
- $p_T^{\pi^\pm} > 20$  MeV/c
- common vertex  $\chi^2/\text{ndf}$  of the four tracks  $J/\psi(\mu^+\mu^-)$ ,  $\pi^+$ ,  $\pi^-$ , smaller than 10
- $|M_{(\mu^+\mu^-)\pi^+\pi^-} - M_{\psi'}^{PDG}| < 400$  MeV/c<sup>2</sup>.

At the end of this loose selection, the  $\psi'$  invariant mass is re-calculated constraining the 4-momentum of  $J/\psi$  to the true  $J/\psi$  mass. This reduces the spread of the signal  $\psi'$  invariant mass distribution (the RMS reduces of a factor  $\sim 2$ ) allowing to evaluate the signal over background ratio in a limited range:  $\sim 95\%$  of signal  $\psi'$  lies in the mass range 3670-3700 MeV/c<sup>2</sup>.

About 538 k inclusive  $J/\psi \rightarrow \mu^+\mu^-$  events have been reconstructed and selected. In order to improve the selection, more refined cuts have been studied.

### Pion transverse momentum cut

In the loose selection discussed above a very low threshold has been set on the pion transverse momentum:  $p_T^{\pi^\pm} > 20$  MeV/c. A harder cut can reject more pion background. The figure 7.1 shows the  $\pi^- p_T$  versus  $\pi^+ p_T$  distribution for the candidates selected with the loose selection described above. As we can see the signal (red markers) is contained in the region  $p_T^{\pi^-} + p_T^{\pi^+} > 300$  MeV/c: several values of the cut have been applied and the one that maximizes the signal significance is resulted to be  $p_T^{\pi^-} + p_T^{\pi^+} > 600$  MeV/c.

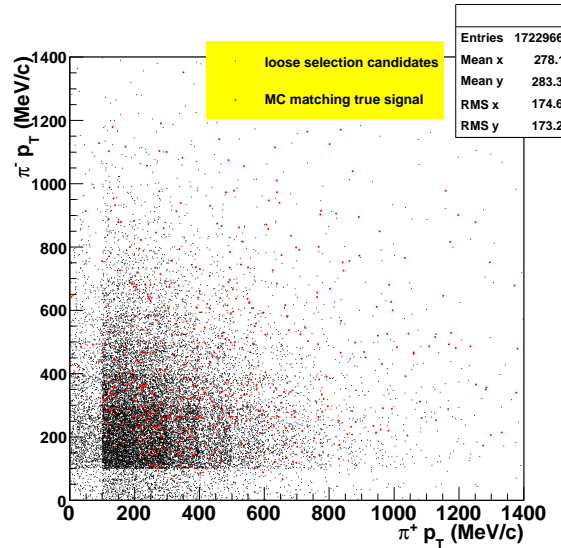


Figure 7.1:  $\pi^-$  versus  $\pi^+$  transverse momentum distribution for candidate  $\psi'$  selected with the loose selection (see text).

This cut has a signal efficiency of  $\sim 73\%$  and a background efficiency of  $\sim 21\%$ .

### $J/\psi$ and $\psi'$ transverse momentum cut

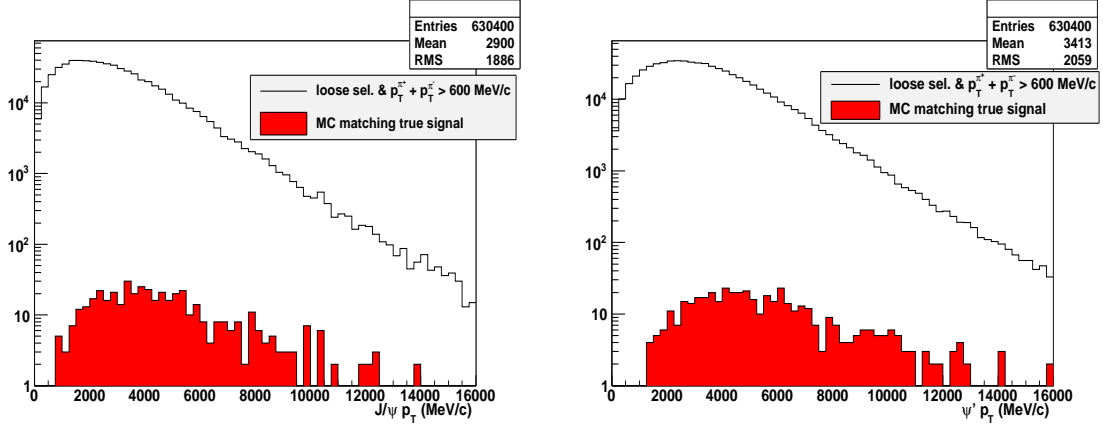


Figure 7.2:  $p_T$  of  $J/\psi$  (left) and  $\psi'$  (right) for candidates selected with the loose selection (see text) and with the further requirement  $p_T^{\pi^+} + p_T^{\pi^-} > 600$  MeV/c.

Once the  $J/\psi$  and  $\psi'$  have been reconstructed, one can introduce a cut on their transverse momentum to reject part of the background. The figure 7.2 shows the transverse momentum distributions of  $J/\psi$  (left) and  $\psi'$  (right) for events selected at which the cuts so far discussed have been applied. The red histograms are filled only if the selected  $\psi'$  matches with a Monte Carlo true  $\psi'$ . To reject a large fraction of background we cutted at  $p_T^{J/\psi, \psi'} > 3.5$  GeV/c. This cut has a signal efficiency of  $\sim 66\%$  and a background efficiency of  $\sim 43\%$ .

### $Q$ cut

A kinematic variable that allow to separate a large part of the background from signal, is the variable  $Q$

$$Q = M(J/\psi\pi^+\pi^-) - M(\pi^+\pi^-) - M(J/\psi). \quad (7.3)$$

The distribution of such variable is shown in figure 7.3. It is evident that the signal (red histogram) is limited to  $Q$  values from 0 to 250 MeV/c<sup>2</sup>. The cut on  $Q$  results to be very useful, as the signal efficiency is  $\sim 100\%$  and the background efficiency is  $\sim 90\%$ . Let us recall that the signal and the background are being evaluated in the mass region 3670-3700 MeV/c<sup>2</sup>. The cut  $Q < 250$  MeV/c<sup>2</sup> rejects background mainly in the right sideband mass region respect to the measured mass  $M(J/\psi\pi^+\pi^-)$ , therefore most of the background cutted off is not background under the mass peak. Such a cut, nevertheless, is useful as allows to reject  $\sim 10\%$  of the background under the mass peak.

### $\Delta r$ cut

Finally, the last cut we have imposed is a cut on the variable  $\Delta r$

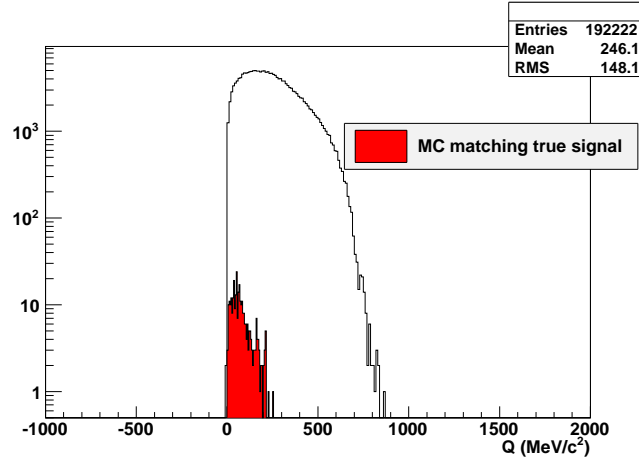


Figure 7.3: Distribution of the variable  $Q = M(J/\psi\pi^+\pi^-) - M(\pi^+\pi^-) - M(J/\psi)$ . The Monte Carlo signal (red histogram) is characterized by a maximum value  $Q=250$  MeV/ $c^2$ .

$$\Delta r = \sqrt{\Delta\varphi^2 + \Delta\eta^2} \quad (7.4)$$

where  $\Delta\varphi$  is the angle between  $\pi^+$  and  $\psi'$ , while  $\Delta\eta$  is the angle between  $\pi^-$  and  $\psi'$ .

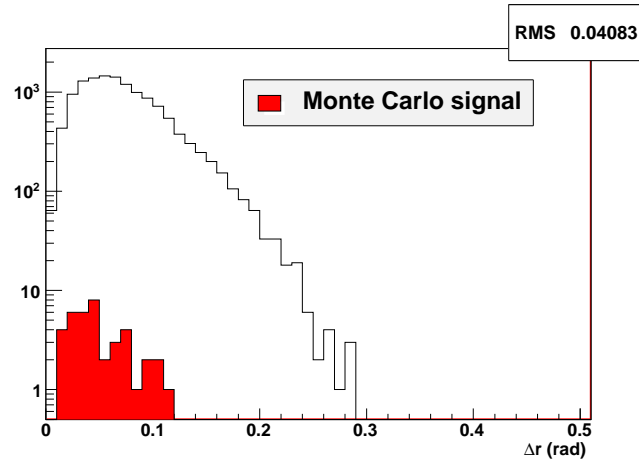


Figure 7.4: Distribution of the variable  $\Delta r$ . The Monte Carlo signal (red histogram) is characterized by a maximum value  $\sim 0.12$ .

From figure 7.4 it is clear that the signal distribution is limited to lower  $\Delta r$  values. A reasonable cut is  $\Delta r < 0.12$ . This cut has a signal efficiency of  $\sim 99\%$  and a background efficiency of  $\sim 97\%$ .

The figure 7.5 shows the invariant mass distribution obtained after that the previous selection cuts have been applied. The mass peak around the  $\psi'$  mass value (3686.09 MeV/c<sup>2</sup>) is not clearly distinguishable due to the dominant contribution of the background. The major problem of this selection is represented by the pion background which gives its most important contribution at high pseudo-rapidity, hence in LHCb.

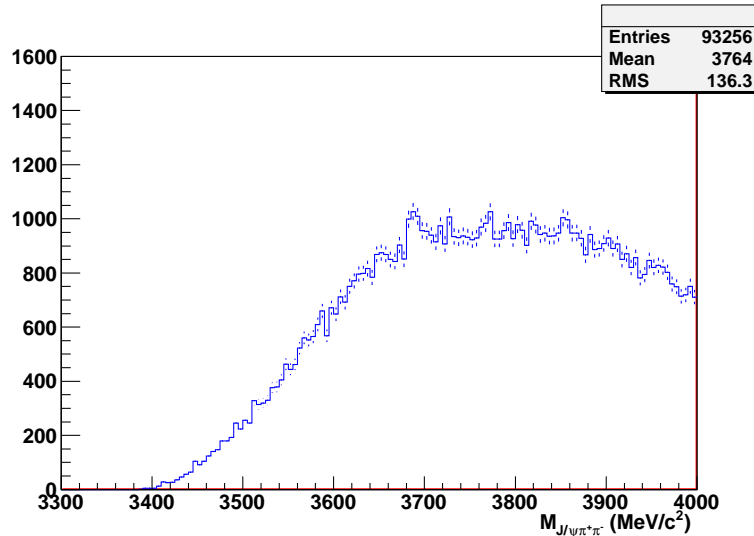


Figure 7.5:  $J/\psi\pi^+\pi^-$  invariant mass reconstructed with the selection cuts described (see text).

The selection here described is not a final selection for the signal  $\psi' \rightarrow J/\psi\pi^+\pi^-$ : more studies are still necessary to refine and set up better the cuts. Nevertheless, there is also an important aspect to highlight: as we said many times in this thesis, in the LHCb Monte Carlo the prompt  $\psi'$  cross-section results to be smaller of a factor  $\sim 3-4$  than the expected value. This is due to the fact that in the simulation of the hadroproduction of  $\psi'$ , the only color singlet process has been taken into account. While this allows to generate  $\psi'$  in the sample of  $J/\psi$ , the production ratio  $\psi'/(J/\psi)$  is not well reproduced and also some important kinematic variables ( $p$ ,  $p_T$ ) could be affected.

The value of the  $\psi'$  cross-section in the current LHCb Monte Carlo is 0.0085 mb. In order to simulate a prompt  $\psi'$  cross-section 3 times larger we may, in first approximation, reduce the background of the same factor. We have done this simple exercise filling the mass histogram with 33.33% of efficiency if the selected  $\psi'$  does not match a Monte Carlo true  $\psi'$ . The result is shown in figure 7.6.

Of course the feasibility of the measurement depends strongly on the real value of the cross-section. While we can rely on Monte Carlo for the acceptance, the reconstruction efficiencies, the trigger efficiencies and all the informations strictly related to the detector modeling, the cross-section simulated depends on the el-

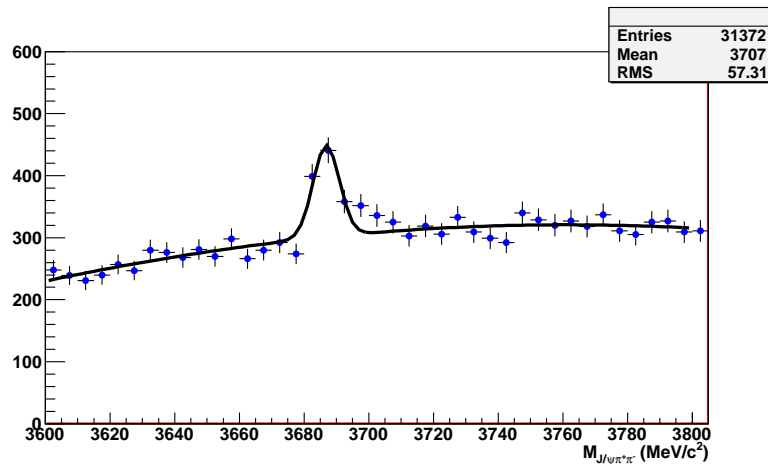


Figure 7.6:  $J/\psi\pi^+\pi^-$  invariant mass. The result reflects a situation in which the prompt  $\psi'$  cross-section was 3 times larger than the value currently simulated in the LHCb Monte Carlo (0.0085 mb).

elementary processes simulated that even if correctly taken into account, nobody knows their exact contribution to the total cross-section at the LHC energies. Only real data measurements at LHC can give us the right values of the cross-sections.

The study described in this chapter is still preliminary but demonstrates that the signal  $\psi' \rightarrow J/\psi\pi^+\pi^-$  is visible at LHCb. The importance of such decay is related to the possibility of measuring the  $\psi'$  dimuon branching fraction, as described above. But there is also another reason: in LHCb there is interest in measuring the  $J^{PC}$  quantum numbers of the  $X(3872)$  resonance through the decay  $X(3872) \rightarrow J/\psi\pi^+\pi^-$ . Therefore the  $\psi' \rightarrow J/\psi\pi^+\pi^-$  can provide calibration samples for future and more complex analyses.



# Chapter 8

## Conclusions

---

The LHCb experiment will play a fundamental role in the measurements of CP violating and rare  $b$ -hadron decays. The main purpose of the experiment is to look for any inconsistency within the Standard Model in the heavy flavour physics sector. In this framework wide space is devoted to the  $c$ -hadron physics and in particular to the  $c\bar{c}$  physics. LHC will offer unique experimental conditions to study the hadroproduction of charmonium and to verify the predictions of NRQCD theory. As we have seen such theory describes very well the  $J/\psi$  and  $\psi(2S)$  production cross-sections measured from CDF at the Tevatron, but fails dramatically in the prediction of the mesons polarization: this indicates that there is some important aspect of the charmonium hadroproduction that is not yet understood.

The decays  $J/\psi \rightarrow \mu^+\mu^-$  and  $\psi(2S) \rightarrow \mu^+\mu^-$  will allow to measure the prompt cross-sections but also will offer abundant samples of muons to do calibrations and alignments of the apparatus in the first periods of data taking. Moreover, such decays are present in the final state of many interesting  $B$  physics decays, such as  $B_d \rightarrow J/\psi(\mu^+\mu^-)K_s$  or  $B_s \rightarrow J/\psi(\mu^+\mu^-)\varphi$ , therefore the charmonium decays studies will open the road towards the future  $B$  physics studies.

In this work of thesis we have presented the theoretical and experimental status of art in the charmonium hadroproduction. In particular we have seen the predictions at LHC based on extrapolations from CDF data. The measurements of  $J/\psi \rightarrow \mu^+\mu^-$  and  $\psi(2S) \rightarrow \mu^+\mu^-$  production cross-sections will be performed at LHCb with the first data. Studies on Monte Carlo show that the statistical error will be reduced at 10% with only  $5 \text{ pb}^{-1}$  of data collected. Nevertheless, the measurement of the absolute cross-section requires the knowledge of the integrated luminosity as well as the knowledge of the global efficiency introduced from the experiment. The efficiency determination requires an accurate check of the Monte Carlo to understand possible biases introduced from the modeling.

On the other hand a measurement that does not require the knowledge of the integrated luminosity and in which most of the systematics on the efficiency cancel out, is the  $\psi'$  to  $J/\psi$  production ratio. Such a measurement can be performed even

before the absolute cross-section measurements and can give a valid result to do cross-check with the subsequent absolute measurements.

The steps to measure the  $\psi'$  to  $J/\psi$  production ratio, in the dimuon decay channel, have been described in this work with studies on Monte Carlo. A dimuon selection has been set up with optimized cuts. Then we described how to extract the prompt signal through a combined fit of the invariant mass and of a *pseudo* proper time variable. We have then described a procedure to extract from Monte Carlo, and in part from real data, the global factor  $(B_{\mu\mu}\epsilon)/(B'_{\mu\mu}\epsilon')$  needed to correct the raw  $\psi'$  to  $J/\psi$  ratio obtained from the fits to the data. In this factor two major systematic errors have been identified: the first is the error due to the branching fraction ratio, which gives a relative error of  $\sim 11\%$ ; the second one is the systematic error arising from assuming unpolarized mesons, which gives a relative error up to  $\sim 22\%$ . The possibility of measuring the polarization of charmonium at LHCb and the necessary integrated luminosity are being studied. Finally some future prospects have been discussed in the last chapter, in which the possibility of reconstruct  $\psi' \rightarrow J/\psi \pi^+ \pi^-$  decays is explored. Combining such measurement with the one based on the dimuon channel, the systematic error in the measurement of the  $\psi'$  to  $J/\psi$  ratio could be substantially reduced.

On November 23rd 2009, LHCb registered the first proton-proton collisions at 450+450 GeV energy and on December 14th 2009, we had collisions at 1.2+1.2 TeV. In the last weeks thousands of events have been triggered and reconstructed in the detector and are being analysed for first calibrations and alignments of the sub-detectors. So far we collected about 300 k minimum-bias events from proton-proton collisions, with the LHCb magnetic field on. The figure 8.1 shows a preliminary dimuon invariant mass distribution obtained from the first collisions data. Such dimuon masses have been determined with a muon stand-alone tracking pro-

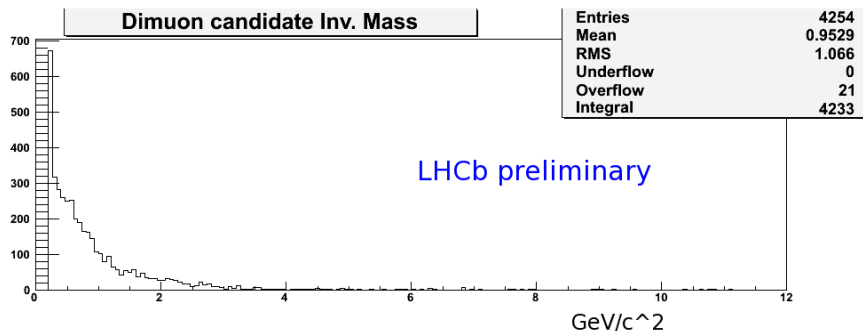


Figure 8.1: The plot shows a preliminary dimuon invariant mass obtained from the first collisions data.

cedure (without using the tracking system), hence with a worst mass resolution than the mass resolution expected when the tracking system will be included. Unfortunately the number of events  $J/\psi(\mu^+\mu^-)$  expected in the statistics collected is still too low.

The preliminary results are very promising and show a good agreement between data and Monte Carlo. The LHCb experiment is now fully commissioned and ready for Physics at the TeV scale.



# Bibliography

---

- [1] M. Blanke, A.J. Buras, D. Guadagnoli and C. Tarantino, arXiv:hep-ph/0604057 (2006).
- [2] ATLAS collaboration, *ATLAS: technical proposal for a general-purpose pp experiment at the Large Hadron Collider at CERN*, CERN-LHCC-94-43.
- [3] CMS collaboration, *CMS technical proposal*, CERN-LHCC-94-38.
- [4] TOTEM collaboration, *TOTEM, Total cross section, elastic scattering and diffractive dissociation at the LHC: Technical Proposal*, CERN-LHCC-99-007.
- [5] ALICE collaboration, *ALICE: Technical proposal for a Large Ion collider Experiment at the CERN LHC*, CERN-LHCC-95-71.
- [6] LHCf collaboration, *The LHCf detector at the CERN Large Hadron Collider*, 2008 JINST 3 S08006.
- [7] LHCb collaboration, *Technical Proposal*, CERN-LHCC-98-4.
- [8] LHCb collaboration, *Reoptimized Detector Design and Performance*, CERN-LHCC-2003-030.
- [9] LHCb collaboration, *LHCb VELO Technical Design Report*, CERN-LHCC-2001-011.
- [10] LHCb collaboration, *LHCb RICH Technical Design Report*, CERN-LHCC-2000-037.
- [11] LHCb collaboration, *LHCb Magnet Technical Design Report*, CERN-LHCC-2000-007.
- [12] LHCb collaboration, *The LHCb Detector at the LHCb*, 2008 JINST 3 S08005.
- [13] J. Gassner, M. Needham and O. Steinkamp, *Layout and expected performance of the LHCb TT station*, Note LHCb-2003-140.
- [14] LHCb collaboration, *Inner Tracker Technical Design Report*, CERN-LHCC-2002-029.

- [15] LHCb collaboration, *LHCb Outer Tracker*, CERN-LHCC-2001-024.
- [16] LHCb collaboration, *LHCb Calorimeters Technical Design Report*, CERN-LHCC-2000-036.
- [17] LHCb collaboration, *LHCb Muon System Technical Design Report*, CERN-LHCC-2001-010.
- [18] M. Calvi et al., *Flavour Tagging Algorithms and Performances in LHCb*, Public Note LHCb 2007-058.
- [19] *GEANT detector description and simulation tool*, CERN Program Library long writeup W5013 (1994).
- [20] S. de Capua et al., *Study of gas gain uniformity of the LHCb Muon System MWPCs using cosmic rays*, Public Note LHCb 2006-010.
- [21] G. Sabatino et al., *Cluster size measurements for the LHCb Muon System M5R4 MWPCs using cosmic rays*, Public Note LHCb 2006-011.
- [22] G. Martellotti et al., *Study of the performance of the LHCb MWPC with cosmic rays*, Public Note LHCb 2008-057.
- [23] W. Bonivento et al., *Production of the front-end boards of the LHCb muon system*, Note LHCb-2007-150, <http://cdsweb.cern.ch/record/1079951>.
- [24] G. Haefeli et al., *The LHCb DAQ interface board TELL1*, N.I.M. A 560 (2006) 494.
- [25] E. Polycarpo, M. Gandelman, *The performance of the LHCb Muon Identification procedure*, LHCb 2007-145.
- [26] G. Lanfranchi et al., *The Muon Identification Procedure of the LHCb Experiment for the First Data*, LHCb-PUB-2009-013.
- [27] M. Krasowski et al., *Primary vertex reconstruction*, Note LHCb-2007-011.
- [28] The LHCb collaboration, *LHCb Online System, Data Acquisition and Experiment Control*, CERN-LHCC-2001-40.
- [29] The LHCb collaboration, *GAUSS-The LHCb Simulation Program*, <http://lhcb-release-area.web.cern.ch/LHCb-release-area/DOC/gauss/>.
- [30] T. Sjöstrand et al., *High-energy physics event generation with PYTHIA 6.1*, *Comput. Phys. Commun.* **135** (2001) 238.
- [31] The LHCb collaboration, *BOOLE-The LHCb Digitization Program*, <http://lhcb-release-area.web.cern.ch/LHCb-release-area/DOC/boole/>.
- [32] <http://lhcb-release-area.web.cern.ch/LHCb-release-area/DOC/moore/>.

- [33] The LHCb collaboration, *BRUNEL-The LHCb Reconstruction Program*, <http://lhcb-release-area.web.cern.ch/LHCb-release-area/DOC/brunel/>.
- [34] The LHCb collaboration, *DAVINCI-The LHCb Analysis Program*, <http://lhcb-release-area.web.cern.ch/LHCb-release-area/DOC/davinci/>.
- [35] <http://lhcb-release-area.web.cern.ch/LHCb-release-area/DOC/panoramix/>.
- [36] N. Brambilla et al., *Heavy Quarkonium Physics*, HEP/PH 04-12-158 v2, CERN-2005-005, Yellow Report.
- [37] E.L. Berger, D.L. Jones, *Inelastic photoproduction of  $J/\psi$  and  $\Upsilon$  by gluons*, Phys. Rev. D 23, 1521-1530 (1981).
- [38] R. Baier, R. Ruckl, Phys. Lett. B 102 (1981) 364.
- [39] C.H. Chang, *Hadronic production of  $J/\psi$  associated with a gluon*, Nucl. Phys. B, 172, 425 (1980).
- [40] E. Braaten and T.C. Yuan, *Gluon fragmentation into heavy quarkonium*, Phys. Rev. Lett. 71, 1673 - 1676 (1993).
- [41] M. Kramer, *Quarkonium production at high-energy colliders*, Prog. Part. Nucl. Phys., 47, 141-201 (2001).
- [42] G.T. Bodwin, E. Braaten, G.P. Lepage, *Rigorous QCD analysis of inclusive annihilation and production of heavy quarkonium*, Phys. Rev. D 51, 1125 - 1171 (1995).  
G.T. Bodwin, E. Braaten, G.P. Lepage, *Erratum: Rigorous QCD analysis of inclusive annihilation and production of heavy quarkonium [Phys. Rev. D 51, 1125 (1995)]*, Phys. Rev. D 55, 5853 - 5854 (1997).
- [43] G.P. Lepage et al., *Improved nonrelativistic QCD for heavy-quark physics*, Phys. Rev. D 46, (1992) 4052.
- [44] J. Baines et al., *Bottom Production*, arXiv:hep-ph/0003142v2, 29 Aug 2001.
- [45] D. Acosta et al., *Measurement of the  $J/\psi$  Meson and  $b$ -Hadron Production Cross Sections in  $p\bar{p}$  Collisions at  $\sqrt{s}=1960$  GeV*, Phys. Rev. D71:032001, 2005.
- [46] T. Aaltonen et al., *Production of  $\psi(2S)$  Mesons in  $p\bar{p}$  Collisions at 1.96 TeV*, Phys. Rev. D80:031103, 2009.
- [47] P. Faccioli et al.,  *$J/\psi$  polarization from Fixed-Target to Collider Energies*, PRL 102 151802 (2009).
- [48] R.J. Cropp, FERMILAB-THESIS-2000-03.

- [49] The CDF collaboration, *Polarizations of  $J/\psi$  and  $\psi(2S)$  Mesons Produced in  $p\bar{p}$  Collisions at  $\sqrt{s}=1.96$  TeV*, Phys. Rev. Lett. 99, 132001 (2007).
- [50] S.P. Baranov, *Highlights from the  $k_T$ -factorization approach on the quarkonium production puzzles*, Phys. Rev. D 66, 114003 (2002).
- [51] The HERA-B collaboration, *Angular distributions of leptons from  $J/\psi$ 's produced in 920 GeV fixed-target proton-nucleus collisions*, Eur.Phys.J.C, Vol.60, Number 4 (2009), 517-524.
- [52] M. Bargiotti, V. Vagnoni, *Heavy Quarkonia sector in PYTHIA 6.324: tuning, validation and perspectives at LHC(b)*, Public Note LHCb-2007-042.
- [53] C. Amsler et al. (Particle Data Group), PL B667, 1 (2008) and 2009 partial update for the 2010 edition (URL: <http://pdg.lbl.gov>).
- [54] The HERA-B collaboration, *A Measurement of the  $\psi'$  to  $J/\psi$  production ratio in 920 GeV proton-nucleus interactions*, Eur. Phys. J. C49, 545-558 (2007).
- [55] The EvtGen package homepage, <http://www.slac.stanford.edu/lange/EvtGen/>